Numerical simulation of CO_2 storage in saline aquifers

Francesca Elizabeth Watson

A THESIS SUBMITTED IN PARTIAL FULFILMENT OF THE REQUIREMENTS FOR THE DEGREE OF DOCTOR OF PHILOSOPHY AT DURHAM UNIVERSITY

Department of Earth Sciences
Durham University
April 2015

Abstract

CO_2 capture and storage (CCS) has been proposed as a climate change mitigation strategy. The basic principle is to prevent CO_2 which would normally be emitted from large point sources, such as power stations, from entering the atmosphere. This is achieved by capturing the CO_2 at source and storing it in a location where it will be trapped and unable to enter the atmosphere. This work looks specifically at geological storage of CO_2 in deep saline formations.

Dynamic simulations can be used to investigate the fundamental physical and chemical processes which occur when CO_2 is injected into geological formations. They can also be used to determine the suitability of a particular site for CO_2 storage. The scale of the processes being simulated is important when building a dynamic model. Here dynamic simulations have been used to explore three different aspects of geological CO_2 storage in deep saline formations. The first model investigates large scale CO_2 migration and pressure build up at a potential CCS site. The second model concentrates on the small scale processes of CO_2 dissolution and convection. The third model attempts to accurately model both the large scale processes of CO_2 injection and migration and the small scale processes of CO_2 dissolution and convection.

Dynamic simulations have been used to model storage capacity, CO_2 migration and pressure buildup at a potential CO_2 storage site in the UK North Sea. There are large uncertainties in the input data so various models have been run using a range of parameters. The primary control on pressure buildup at the site is the permeability of the unit directly beneath it. The plume diameter is primarily controlled by the porosity and permeability of the reservoir unit. Despite uncertainties in the input data, the use of a full three-dimensional (3D) numerical simulation has been extremely useful for identifying and prioritizing factors that need further investigation.

Dissolution of CO_2 into existing formation waters (brine) leads to an increase in brine density proportional to the amount of dissolved CO_2. This can lead to gravitational instabilities and the formation of convection currents. Convection currents, in turn, will increase CO_2 dissolution rates by removing CO_2 saturated brine from the CO_2-brine interface. The dissolution and subsequent convection of CO_2 which has leaked through a fracture is investigated using dynamic simulations. The instigation of convection currents due to flow through a fracture increases dissolution rates. Comparison of our results with fracture flow rates shows that for typical fracture apertures dissolution from a fracture is small relative to the amount of CO_2 flowing through the fracture.

Two phase flow effects and the currents caused by an advancing plume of injected CO_2 can affect patterns of CO_2 dissolution and convection within a reservoir. Most existing models of CO_2 dissolution and convection use a static boundary layer or do not involve two phase flow effects. A radial, two phase, two component model has been built to model the injection process along with convection enhanced dissolution. The model performs well compared to analytical solutions in terms of the large scale processes of CO_2 migration and pressure buildup but modelled convection is highly dependent on grid resolution. Numerical instabilities are also present. Further work is needed to increase the accuracy of the model in order to allow higher resolution modelling to be carried out and modelling of the smaller scale processes to be improved.

Contents

List of Figures

List of Tables

Declaration

I declare that this thesis, presented for the degree of Doctor of Philosophy at Durham University, is a result of my own original research and has not been previously submitted to Durham University or any other institution. I have clearly indicated, when appropriate, the contributions of colleagues and have made every effort to acknowledge all collaborative work.

Francesca Watson

Durham University

April 2015

Acknowledgements

This work would not have been possible without generous sponsorship from my employer, Geospatial Research Limited (GRL), both financially and in terms of the time I have been allowed in which to work towards this thesis. For this I would like to thank Richard Jones for employing me in the first place and then allowing me to pursue a PhD after only being at GRL a couple of months! I sincerely hope that the work I've done and the skills I've learnt have been of some benefit to GRL and that it's been worth it.

I would like to thank Jeroen van Hunen for getting me started with this PhD and providing scientific insight, encouragement and advice throughout.

I would like to thank Susie Daniels for helping me to see the bigger, geological picture and preventing me from getting carried away with the maths!

I would like to thank Simon Mathias for enabling me to do something that I've always wanted to do, i.e. surround myself with pages of equations and pretend to be clever.

To all my supervisors, I have thoroughly enjoyed myself during my PhD and this can only be down to your invaluable support and vast knowledge which you have been willing to share. I have learnt so much from you all about the subject and generally about how to be a good scientist. I honestly don't think anyone else could have taught me better.

To everyone I've had the pleasure of working with at GRL, thanks for your plentiful encouragement and advice throughout my PhD.

I would like to thank Ben Hedley and Richard Davies for all their help with the work carried out in Chapter 4 and insights on CCS in general.

I would like to thank all of Simon's PhD students and post docs that I've known whilst I've been at Durham for help with my work and general chat about related and unrelated topics: Cath, Kate, Gerardo, Tore, Salim, Helena, Jack and Ayo. I would particularly like to thank Lena for checking all my equations in Chapter 6!

To all the footy girls, past and present, thanks for keeping me sane(!) and making my PhD experience / life in general much more brightly coloured. It's not an exaggeration to say that I don't know what I would have done without you.

In addition to everyone mentioned already I would like to thank the following people for laughter and good times plus general PhD backup support over the last few years: Jo, Katie, Dean, Yang, Bansri, Kester, Effie, Magnus, Sarah, Rich, Wanda, Ben P, Cat, Sam, Alison, Louise and Siân. What would life be without Sunday Night Film Club and Monday Bunday Funday?

Finally I would like to thank Dad, Marcus, Julie and Martin for everything you've done for me during my PhD and beyond. I know I'm lucky to have you all. And of course, thank you Zak.

Dedication

This thesis is dedicated to my wonderful Mum and to everyone else who still misses her like crazy.

Nomenclature

This is a partial list of symbols used in this thesis. Some symbols have been used to denote different things in different contexts. Numbers in italics indicate equation numbers, numbers in bold indicate page numbers where the definition occurs.

Notation	Definition	
γ'	Activity coefficient of aqueous CO_2 in brine	*3.54*, *3.66*, **31**
γ_{mi}	Activity coefficient of component i in the aqueous phase on a molality scale	*3.35*, **28**
γ_{xi}	Activity coefficient of component i in the aqueous phase on a mole fraction scale	*3.32*, **28**
λ	Duan and Sun parameter	*3.66*, *3.67*, **34**
λ_c	Critical wavelength of convective fingers	*7.1*, **121**
μ_i	Chemical potential of component i	*3.16*, *3.18*, **24**
ϕ	Porosity	*2.2*, **9**
ϕ_i	Fugacity coefficient of component i in the gaseous phase	*3.31*, **27**
ρ_j	Density of phase j	*2.2*, **9**
ρ_{ij}	Partial density of component i in phase j	*6.4*, **88**
ξ	Duan and Sun parameter	*3.66*, *3.68*, **34**
a	Redlich-Kwong parameter	*3.2*, *3.3*, **16**
a_{mi}	Activity of component i in the aqueous phase on a molality scale	*3.37*, **29**
a_{xi}	Activity of component i in the aqueous phase on a mole fraction scale	*3.36*, *3.37*, **29**

Notation	Definition	
b	Redlich-Kwong parameter	*3.2*, **16**
b	Fracture aperture	*5.20*, **80**
C	Concentration	*5.3*, **73**
c_f	Fluid compressibility	*5.3*, **73**
c_{ij}	Compressibility of component i in phase j	*6.50*, **98**
c_j	Compressibility of phase j	*6.49*, *6.50*, **97**
c_r	Rock compressibility	*5.3*, *6.48*, **73**, **97**
$\boldsymbol{D_A}$	Apparent diffusivity	*5.3*, **73**
$\boldsymbol{D_E}$	Effective diffusivity	*2.5*, **10**
F	Total mass of all components	*6.0*, *6.1*, **88**
$\boldsymbol{F_{a_i}}$	Advective mass flux of component i	*2.2*, *2.4*, **9**
$\boldsymbol{F_{d_i}}$	Diffusive mass flux of component i	*2.2*, *2.5*, **9**
f_i	Fugacity of component i in the gaseous phase	*3.29*, **27**
G_i	Mass of component i	*2.1*, *2.2*, **9**
G	Gibbs energy	*3.16*, *3.17*, **24**
$\boldsymbol{g}$	Gravity	*2.6*, **10**
$\boldsymbol{H_i}$	Mass flux of component i	*2.2*, *2.3*, **9**
H	Model height	**74**
$\boldsymbol{k}$	Permeability	*2.6*, **10**
k_0	Redlich-Kwong parameter	*3.3*, **16**
k_1	Redlich-Kwong parameter	*3.3*, **16**
k_h	Horizontal permeability	**108**
K_i	Equilibrium coefficient of component i	*3.42*, *3.43*, **29**
k_{ra0}	End point aqueous phase permeability	*2.8*, **10**
k_{rg0}	End point gaseous phase permeability	*2.8*, **10**
k_{rj}	Volumetric flux of phase j	*2.6*, **10**
k_v	Vertical permeability	**108**
L	Model length	**74**
m	Relative permeability parameter	*2.8*, **10**
M_0	Injection rate	**107**, **108**
M_{CO_2}	Molar mass of CO_2	*3.4*, **17**

Notation	Definition	
m_i	Molality of component i	*3.35*, **28**
m_v	Capillary pressure parameter	*2.9*, **11**
n	Relative permeability parameter	*2.8*, **10**
N_c	Number of components	*2.2*, **9**
n_i	Number of moles of component i	*3.17*, **25**
N_p	Number of phases	*2.2*, **9**
n_r	Number of grid points in the r direction	**111**
n	Number of moles	*3.1*, **16**
n_z	Number of grid points in the z direction	**111**
P	Total pressure	*6.6*, *6.7*, **89**
P_c	Capillary pressure	*2.8*, *2.9*, **10**
P_{c0}	Capillary pressure parameter	*2.9*, **11**
P_i	Partial pressure of component i	*3.26*, *3.27*, **26**
P_j	Pressure of phase j	*2.6*, **10**
$\boldsymbol{q_j}$	Volumetric flux of phase j	*2.5*, *2.6*, **10**
q_x	Volumetric flux in the x direction	*5.2*, *5.3*, **73**
q_z	Volumetric flux in the z direction	*5.2*, *5.3*, **73**
R	Gas Constant	*3.1*, **16**
Ra	Rayleigh number	*5.9*, **70**
r_E	Model radial extent	**107**
r_W	Model well radius	**107**
S	Entropy	*3.17*, **25**
S_{ar}	Residual aqueous saturation	*2.8*, **10**
S_{gc}	Critical gas saturation	*2.8*, **10**
Sh	Sherwood number	*5.14*, *5.15*, **78**
S_j	Saturation of phase j	*2.2*, **9**
$\bar{V}_i$	Partial molar volume of component i	*3.22*, *3.23*, **26**
x_i	Mole fraction of component i in the aqueous phase	*3.31*, **27**
X_{ij}	Mass fraction of component i in phase j	*2.2*, **9**

Notation	Definition	
x_{ij}	Equilibrium mass fraction of component i in phase j	*6.8*, **90**
X_s	Salt mass fraction	*3.6*, **18**
y_i	Mole fraction of component i in the gaseous phase	*3.27*, **27**
z_i	Mass fraction of component i	*6.2*, *6.3*, **88**

Chapter 1

Introduction

Carbon capture and storage (CCS) has received plenty of attention over recent years as a possible method of mitigation against increasing atmospheric CO_2 emissions. Deep geological formations are the main type of storage location proposed for the CO_2. Numerical modelling of CO_2 injection into these reservoir formations is based on the same fundamental principles used to model fluid flow in hydrocarbon reservoirs although there are differences, for instance in terms of the fluids being modelled, the configuration of wells within models and the amount of input data available. In this thesis various different numerical models have been used to investigate the process of injecting CO_2 into deep saline aquifers.

1.1 Why are we interested in CO_2 storage?

Global mean surface temperatures (GMST) have undergone a statistically significant rise (0.85 °C) over the period 1880 to 2012 (Fig. 1.1). Studies suggest that increasing temperatures will have negative impacts on people, economies and the environment (e.g. Patz *et al.*, 2005; Mendelsohn *et al.*, 2006; Hoegh-Guldberg & Bruno, 2010). Monte Carlo simulations of various contributing factors to global temperature change (radiative forcing) show that the primary reason for an increase in GMST is likely to be an increase in greenhouse gases in the atmosphere (Myhre *et al.*, 2013). A major source of greenhouse gases, and in particular CO_2, is the energy industry. However, global energy demand is predicted to rise steeply accompanied by a corresponding increase in CO_2 emissions (U.S. Energy Information Administration, 2014). CCS has been proposed as one of several methods for keeping atmospheric greenhouse gas emissions at an acceptable level whilst meeting global energy requirements (Pacala & Socolow, 2004).

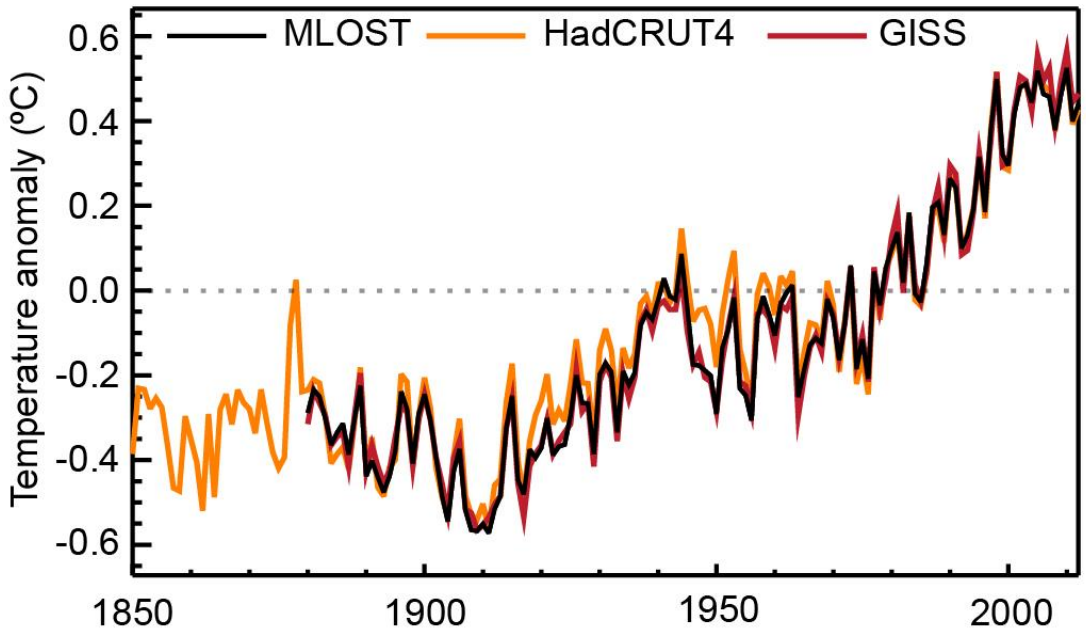

Figure 1.1: Annual global mean surface temperature (GMST) anomalies 1850-2012, relative to average temperatures over the period 1961-1990, from the latest version of the three combined land-surface air temperature (LSAT) and sea surface temperature (SST) data sets (HadCRUT4, GISS and NCDC MLOST) (Hartmann *et al.*, 2013)

1.2 Overview of geological storage of CO_2

Geological CCS involves capturing CO_2 from an emissions source (e.g. a power station), transporting it to a suitable storage location and injecting it into an underground geological formation where it should stay for an extended period of time.

The two primary types of geological formation being considered for CCS are depleted oil or gas reservoirs (DOGRs) and deep, saline formations. The main difference between DOGRs and deep, saline formations being that DOGRs have been exploited for hydrocarbons whereas saline formations do not contain hydrocarbons and have not been depleted. In terms of numerical modelling this has implications for factors such as reservoir pressure and fluid chemistry. This thesis is concerned with CO_2 storage in deep, saline formations.

For reasons of efficiency CO_2 will generally be stored in supercritical phase. The density of supercritical CO_2 is similar to that of a liquid but supercritical CO_2 viscosity is closer to that of a gas. The CO_2 will be compressed until it reaches supercritical phase and then injected

underground at depths greater than 800 m, where the pressure and temperature are high enough for it to remain in supercritical phase (7.38 MPa and 31 °C).

When CO_2 is injected into a saline formation certain mechanisms, known as trapping mechanisms, work to keep the CO_2 from migrating back to the surface. Possible trapping mechanisms are: structural and stratigraphic trapping, residual trapping, dissolution trapping and mineral trapping.

In a saline aquifer supercritical CO_2 is less dense than in situ reservoir fluids so it will rise due to buoyancy. Structural and stratigraphic trapping refer to CO_2 rising and becoming stuck beneath a barrier to flow such as a low permeability layer or a sealed fault. This is the main form of trapping in the initial stages after CO_2 injection. Structural and stratigraphic trapping can be modelled by having low permeability layers in the model or by implementing boundaries which don't allow flow across them.

Residual trapping is a phenomenon related to multiphase flow where small droplets of CO_2 within pores become surrounded by the aqueous phase and are disconnected from the rest of the CO_2, rendering them immobile. This is modelled by having a residual CO_2 saturation below which the relative permeability of the supercritical phase is set to zero (see Section 2.2.1 for more details).

Dissolution trapping is when the supercritical CO_2 dissolves into the in situ fluids. Dissolution will occur at the interface between the CO_2 plume and surrounding brine. Dissolution of CO_2 into brine is useful because brine density increases with dissolved CO_2 content so dissolved CO_2 will sink under gravity. This reduces the chance of CO_2 escaping upwards, towards the atmosphere and is therefore favourable for CO_2 storage.

Mineral trapping pertains to the precipitation of new carbonate minerals from dissolved CO_2 and other substances present. Mineral trapping has not been investigated in this thesis due to the complexity that this would add to the model and the relatively long timescales over which significant mineral trapping is likely to occur (1000s of years).

1.3 The utility of dynamic modelling for CCS

The overall purpose of CCS as defined by the European Union Directive on the geological storage of carbon dioxide is (European Union, 2009):

> "... the permanent containment of CO_2 in such a way as to prevent and, where

this is not possible, eliminate as far as possible negative effects and any risk to the environment and human health."

therefore successful storage of CO_2 would reduce the long term risks to the planet by removing CO_2 from the atmosphere permanently at the same time as minimising short term risks to the population such as ground movement or migration into drinking water sources, by being carried out in a responsible way.

Minimising the short term risks requires us to have an understanding of the likely migration patterns of the CO_2 once injected. Likewise an understanding of the possible pressure change due to injection can provide an insight into the likelihood of processes such as fracturing or fault reactivation. Dynamic flow models can model injection of CO_2 before it takes place in order to predict CO_2 movement and pressure buildup within the reservoir. Results from such modelling can inform decisions about site selection and about operational parameters for instance injection well location.

The longer term success of a storage site is related to how much CO_2 can be stored at a site and the length of time it will remain there. Permanence of CO_2 storage is controlled by the efficiency of trapping mechanisms. Dynamic models can provide storage capacity estimates and predictions of the trapping mechanisms at work over various timescales.

The underground system is complex and any models produced are necessarily simplified compared to the real situation being represented. Nevertheless modelling can provide a useful insight into many aspects of interest to scientists and engineers. It is also important to note that models cannot be directly tested as there is no way to get a complete understanding of what is happening in the subsurface.

1.4 Thesis overview

This thesis describes numerical modelling undertaken to better understand the processes involved when injecting CO_2 into deep saline formations. Modelling CO_2 storage in deep saline formations is a complex problem which requires knowledge of porous media flow mechanisms, multiphase flow dynamics and chemical thermodynamics along with an understanding of the analytical / numerical methods required to carry out the modelling and an understanding of the geological properties of the site being modelled. Another important aspect of numerical modelling is the scale of the processes the model is trying to represent. Within this thesis

dynamic modelling has been carried out for three different problems relating to CCS and on three different scales. These three sections are described below:

1. In Chapter 4 we use a commercially available simulation package, TOUGH2 with ECO2N, for predictive modelling of CO_2 storage at a potential storage site in the UK North Sea. The aims of this part of the thesis are to assess the suitability of the site for CO_2 storage, to identify important limiting factors and major uncertainties and to look at the relative benefits of carrying out 3D dynamic simulations compared with using analytical solutions or static simulations. It is shown that 3D dynamic models are useful in a situation such as this for looking at a range of situations, planning further work and refining capacity estimates. This section deals with numerical modelling of CCS on a large scale. It would not be easy to use the same model to investigate the smaller scale processes occurring within a storage site, for instance CO_2 dissolution. Furthermore, the number of processes being modelled in TOUGH2/ECO2N is large making it difficult to isolate a single process and investigate it on its own.

2. Modelling on a smaller scale allows us to isolate specific processes which are likely to occur when CO_2 is injected underground. Chapter 5 deals with the process of CO_2 dissolution in brine and in particular CO_2 dissolution associated with flow of CO_2 through fractures. Investigating this requires a single (liquid) phase model with two components (CO_2 and brine). To this end a simple 2D MATLAB model has been built allowing us to strip out the complexities of modelling multiphase flow and focus purely on the dissolution process. Simulations have been undertaken in a general fashion using non-dimensional parameters thus enabling the results to be applied to different situations (i.e. various reservoirs with different properties).

3. In Chapter 7 an attempt has been made to build a model which combines both the small scale process of convective dissolution and field scale injection and migration. The model built in Chapter 5 has been extended in Chapters 6 and 7 to include multiphase flow and miscibility between phases. This is in order to look at the effect of CO_2 injection and subsequent migration on patterns of CO_2 dissolution and convection. The model is able to simulate the large scale injection process well. However, resolution testing indicates that the smaller scale processes are highly dependent on grid resolution and therefore the model is unable to convincingly simulate the dissolution process, within the boundaries of computing power available. Further work needs to be carried out to improve the numerical method used or to parallelise the code.

An overview of the governing equations used and the finite difference method is presented in Chapter 2. Chapter 3 describes correlations used to calculate thermodynamic fluid properties used in subsequent chapters. A discussion of the utility of dynamic simulations for CCS and suggestions for further work are presented in Chapter 8.

Chapter 2

Dynamic modelling for CO_2 storage

Summary

This chapter gives a brief overview of the dynamic modelling process for CCS. Equations which govern the processes of flow and transport in the models used in later chapters (Chapters 4, 5 and 7) are described below. The equations are applicable to multiphase and multicomponent flow but do not include variations in temperature. The finite difference method used to approximate the solution to the equations is also described.

2.1 Introduction

Dynamic modelling is used to assess the evolution through time of conditions within the site, in response to CO_2 injection. As a minimum requirement a dynamic model will model flow of fluids within the reservoir, including the injected CO_2 and the original reservoir fluids. A more complex model will also simulate the chemical reactions between the fluids such as the dissolution of CO_2 into reservoir brine. Models are either at a constant temperature or include the changes in temperature affecting the reservoir. A dynamic model can be extended by modelling the interaction of the fluids with the reservoir rocks in terms of chemical reactions ('reactive transport modelling') and in terms of stresses induced on the rocks with fluid pressure increases ('geomechanical modelling').

The various aspects to be modelled must be described by some governing equations, for instance fluid flow within a porous medium is often described by the equation for Darcy's law. Once the relevant governing equations are chosen they must be solved over the region of the model using either analytical or numerical methods.

Another important part of the dynamic modelling process is populating the model with data. In this respect, dynamic modelling of deep saline aquifers provides an extra challenge compared to depleted oil and gas reservoirs due to the limited availability of site specific data. Often data from literature and analogues must be synthesised and used in place of direct site data (e.g. see Chapter 4).

The purpose of the dynamic models developed in this thesis is to model the movement of fluids when CO_2 is injected into a porous medium initially saturated with brine, and to model the associated pressure changes. No temperature change, geochemical reactions (other than CO_2 dissolution in brine) or geomechanical stresses have been modelled.

For the multiphase models presented in Chapters 4 and 7 the phases being modelled are a supercritical phase (hereafter referred to as the gaseous phase) and an aqueous phase.

The components that make up the phases are CO_2, H_2O and NaCl. The gaseous phase is predominantly CO_2 with some dissolved H_2O and the aqueous phase is predominantly brine, H_2O and NaCl, with some dissolved CO_2.

The single phase model in Chapter 5 contains an aqueous phase and the components H_2O, NaCl and CO_2 although the model effectively only has two components as the H_2O and NaCl are modelled together as brine.

The reservoir in which the injection takes place is represented by a series of grid points or cells. Each grid point is assigned certain values for porosity and permeability. The change in the component masses over time and the change in pressure over time at each grid point are controlled by the governing equations. The initial phase saturation, component masses and fluid pressure are set for each grid point and the governing equations are then solved at each grid point showing the evolution of components and pressure within the model, through time.

Analytical solution of the governing equations is generally not possible hence some numerical method, in this case the finite difference method, is used to approximate the solution to the governing equations at the required timesteps and grid points.

2.2 Governing equations

The governing equations for multiphase and multicomponent flow in porous media are described below.

The mass balance equation states that the change in mass of a component is equal to the divergence of the mass flux of that component in all phases:

$$\frac{\partial G_i}{\partial t} = -\nabla \cdot \boldsymbol{H_i} \qquad\qquad i = 1, ..., N_c \tag{2.1}$$

where the mass of component i, G_i, is given by:

$$G_i = \phi \sum_{j=1}^{N_p} \rho_j X_{ij} S_j \tag{2.2}$$

and N_c is the number of components in the system, N_p is the number of phases in the system, ϕ is the porosity of the medium, ρ_j is the density of phase j, X_{ij} is the mass fraction of component i in phase j and S_j is the saturation (volume fraction) of phase j. (See Appendix A for details of the divergence operator, $\nabla \cdot ()$, in different coordinate systems.)

The mass flux of component i, $\boldsymbol{H_i}$, is the sum of advective and diffusive fluxes of component i, $\boldsymbol{F_{a_i}}$ and $\boldsymbol{F_{d_i}}$, respectively, in each phase:

$$\boldsymbol{H_i} = \boldsymbol{F_{a_i}} + \boldsymbol{F_{d_i}} \tag{2.3}$$

$$\boldsymbol{F_{a_i}} = \sum_{j=1}^{Np} \rho_j X_{ij} \boldsymbol{q_j} \tag{2.4}$$

$$\boldsymbol{F_{d_i}} = -\sum_{j=1}^{Np} (\rho_j S_j \boldsymbol{D_E} \nabla X_{ij}) \tag{2.5}$$

where $\boldsymbol{q_j}$ is the volumetric flux of phase j and $\boldsymbol{D_E}$ is the effective diffusivity.

The multiphase version of Darcy's law is used to describe the volumetric flux:

$$\boldsymbol{q_j} = -\frac{\boldsymbol{k} k_{rj}}{\mu j} \left(\nabla P_j + \rho_j \boldsymbol{g}\right) \tag{2.6}$$

where $\boldsymbol{k}$ is the permeability of the medium, k_{rj} is the relative permeability of phase j, which is a function of S_j, P_j is the fluid pressure of phase j and $\boldsymbol{g}$ is gravity. (See Appendix A for details of the gradient operator, $\nabla()$, in different coordinate systems.)

2.2.1 Relative permeability

For a multiphase system the permeability for one phase is reduced due to the presence of other phases within the pore space. Relative permeability is the ratio of the permeability of a particular phase within a porous medium to the absolute permeability of the porous medium and is proportional to the phase saturation. For single phase flow relative permeability is equal to one.

We have modelled the relative permeability of the aqueous (wetting) phase, k_{ra} and gaseous (non-wetting) phase, k_{rg} using power law relationships:

$$k_{ra} = k_{ra0} \left(\frac{1 - S_g - S_{ar}}{1 - S_{gc} - S_{ar}}\right)^m \tag{2.7}$$

$$k_{rg} = k_{rg0} \left(\frac{S_g - S_{gc}}{1 - S_{gc} - S_{ar}}\right)^n \tag{2.8}$$

where S_g is saturation of the gaseous phase, S_{ar} is the residual saturation of the aqueous phase which is the minimum saturation that the aqueous phase can be reduced to, S_{gc} is the critical gas saturation which is the minimum gas saturation required before the gas phase can flow, k_{ra0} and k_{rg0} are endpoint permeabilities and m and n are power law exponents. S_{ar}, S_{gc}, k_{ra0}, k_{rg0}, m and n are found by fitting Eqs. (2.7) and (2.8) to empirical data.

2.2.2 Capillary pressure

Capillary pressure, P_c, is the difference in phase pressure between the two phases in contact with each other. It is related to the interfacial tension between the phases and is a function of

phase saturation. We have used the van Genuchten model of capillary pressure (Van Genuchten, 1980):

$$P_c = P_{c0}\left(S_g^{-\frac{1}{m_v}}\right)^{\frac{1}{n}}, \qquad n = \frac{1}{1-m_v} \tag{2.9}$$

where P_{c0} and m_v are empirical parameters.

2.3 Finite difference method

Once we have defined the governing equations we need to decide which variables we are trying to solve for, the primary variables, and formulate partial differential equations (PDEs) describing the change in primary variables with time and space.

In general the PDEs cannot be solved analytically so instead we use numerical methods to approximate the solutions at the required points in time and space.

Suppose we have a function $u(x)$ which is known at discrete x values. We want to find an approximation to $u'(x)$ at the same discrete x values such that:

$$u'(x) = D_x + E_x \tag{2.10}$$

where D_x is the approximation of the first derivative of x and E_x is the error in the approximation, i.e. the difference between D_x and the true value $u'(x)$.

For a central difference approximation we use the points $u(\bar{x}+h)$, $u(\bar{x})$ and $u(\bar{x}-h)$, where $\bar{x}$ is the point at which the solution applies and h is the difference in x for different points in the solution. We are looking for a polynomial of the form:

$$D^0 = au(\bar{x}+h) + bu(\bar{x}) + cu(\bar{x}-h) \tag{2.11}$$

where the superscript 0 denotes the central difference formulation. First we find the Taylor expansions of $u(\bar{x}+h)$, and $u(\bar{x}-h)$ (LeVeque, 2007):

$$u(\bar{x}+h) = u(\bar{x}) + hu'(\bar{x}) + \frac{h^2}{2!}u''(\bar{x}) + \frac{h^3}{3!}u'''(\bar{x}) + \frac{h^4}{4!}u^{(4)}(\bar{x}) + O(h^5)$$
$$u(\bar{x}-h) = u(\bar{x}) - hu'(\bar{x}) + \frac{h^2}{2!}u''(\bar{x}) - \frac{h^3}{3!}u'''(\bar{x}) + \frac{h^4}{4!}u^{(4)}(\bar{x}) + O(h^5) \tag{2.12}$$

Substituting Eq. (2.12) into Eq. (2.11) gives:

$$D^0 = (a+b+c)u(\bar{x}) + (a-c)hu'(\bar{x}) + (a+c)\frac{h^2}{2!}u''(\bar{x}) + (a-c)\frac{h^3}{3!}u'''(\bar{x}) + (a+c)\frac{h^4}{4!}u^{(4)}(\bar{x}) + O(h^5) \tag{2.13}$$

For Eq. (2.13) to equal $u'(x)$ up to the second order term (giving a second order accurate approximation) we need to equate the coefficients in Eq. (2.13) to:

$$\begin{aligned}(a+b+c) &= 0\\ (a-c) &= \frac{1}{h}\\ (a+c) &= 0\end{aligned} \tag{2.14}$$

Rearranging Eq. (2.14) leads to:

$$\begin{aligned}a &= \frac{1}{2h}\\ b &= 0\\ c &= -\frac{1}{2h}\end{aligned} \tag{2.15}$$

which upon substitution into Eq. (2.11) gives:

$$D_x^0 = \frac{1}{2h}\left[u(\bar{x}+h) - u(\bar{x}-h)\right] \tag{2.16}$$

The error, E_x^0, is given by:

$$E_x^0 = D_x^0 - u'(\bar{x}) = (a-c)\frac{h^3}{3!}u'''(\bar{x}) + (a+c)\frac{h^4}{4!}u^{(4)}(\bar{x}) + O(h^5)$$
$$= \frac{1}{6}h^2 u'''(\bar{x}) + O(h^4) \tag{2.17}$$

Using the same method as above the central difference approximation to the second derivative, $u''(x)$, is:

$$D_{xx}^0 = \frac{1}{h^2}[u(\bar{x}+h) - 2u(\bar{x}) + u(\bar{x}-h)] \tag{2.18}$$

$$\tag{2.19}$$

with the error:

$$E_{xx}^0 = D_{xx}^0 - u''(\bar{x}) = (a-c)\frac{h^3}{3!}u'''(\bar{x}) + (a+c)\frac{h^4}{4!}u^{(4)}(\bar{x}) + O(h^4)$$
$$= \frac{1}{12}h^2 u^{(4)}(\bar{x}) + O(h^4) \tag{2.20}$$

For different order accurate approximations and different types of finite difference, forward or backward, we can use more or less terms from the Taylor expansions and different points from the function $u(x)$. For instance, a first order forward difference approximation would use the points $u(\bar{x})$ and $u(\bar{x}+h)$ and only the first two terms of the combined Taylor expansions would approximate $u'(x)$, with the other terms being incorporated into the error.

2.3.1 Model implementation of finite difference method

In Chapter 4 simulations have been run using the TOUGH2 modelling code (Pruess *et al.*, 1999). TOUGH2 uses a first order integrated finite difference method (IFDM) (Narasimhan & Witherspoon, 1976) to discretise in space and an implicit first order finite difference method to discretise in time.

In the IFDM the model domain is split into 3D elements. A volume averaged mass balance equation is used. The left hand side of the mass balance equation (Eq. (2.1)) is divided by the volume of the element in question and the the total flux of a particular phase into the element

is the sum of average fluxes of that phase over each surface of the element, divided by the element volume. The volume averaged mass balance equation is then discretised using a first order finite difference scheme (see Pruess *et al.* (1999) for more details).

In the MATLAB models developed in Chapters 5 and 7 the method of lines has been used. Here the governing PDEs are discretised in space using finite differences and the value of the resulting ordinary differential equation (ODE) is passed to the MATLAB ODE solver, `ode15s`, which integrates the result with respect to time.

A second order central difference method has been used to discretise in space. First order forward differences are used to find the new solution values at midpoints between nodes and then first order forward differences of the midpoint solutions are used to find the new solution at the original node. This allows us to have a second order finite difference approximation with fewer grid points in our final solution. See Appendix B for more details.

Chapter 3

Properties of mixtures of CO_2, H_2O and NaCl

Summary

Solution of the governing equations requires us to calculate certain fluid properties, namely density, viscosity, compressibility and equilibrium compositions, at the pressures and temperatures being modelled. Functions to calculate these properties have been taken from the literature and are described below.

For immiscible fluids we would need functions which apply to fluids only containing a single component (e.g. either CO_2 or H_2O). However, the system we are looking at includes miscibility of CO_2 and H_2O so the two fluids present are supercritical CO_2 containing dissolved water vapour, and brine containing dissolved CO_2. For fluid mixtures we also need to know the equilibrium composition of the mixtures at specified pressures and temperatures. In our model the equations for CO_2 span the range of conditions over which it changes from a gas to a supercritical fluid. In the rest of this chapter the supercritical phase is referred to as the gaseous phase.

This chapter describes the fluid property equations used in the MATLAB model in Chapter 7. The ECO2N fluid property model used in the TOUGH2 model presented in Chapter 4 uses slightly different equations to calculate fluid properties. Fluid properties from both models have been plotted together for comparison.

3.1 Density

3.1.1 Density of CO_2

To calculate the density of a pure (single component) gas we can calculate the volume of a mole of that gas and then convert it to a density using the molar mass of that substance.

For an ideal gas the equation of state relating pressure, P, volume, V and temperature, T is:

$$PV = nRT \tag{3.1}$$

where n is the number of moles present and R is the gas constant. An ideal gas is one in which the molecules are far enough apart such that they do not interact with each other and they take up only a very small proportion of the total volume of the gas. Although ideal gases do not exist they are a useful starting point from which to develop an equation of state for non-ideal gases

Redlich & Kwong (1949) produced the following equation of state, which is a modification of Eq. (3.1) to make it more applicable to real gases:

$$P = \left(\frac{RT}{V-b}\right) - \left(\frac{a}{T^{0.5}V(V+b)}\right) \tag{3.2}$$

Parameter a is related to the attraction between molecules in the gas and parameter b is related to the volume of the gas that is taken up by the molecules themselves. The parameters are found by fitting Eq. (3.2) to empirical data.

Eq. (3.2) has been used in the MATLAB model with parameters given by Spycher *et al.* (2003). Spycher *et al.* (2003) use a slightly modified form of Eq. (3.2) where the value for a is calculated using the equation:

$$a = k_0 + k_1 T \tag{3.3}$$

where temperature is in Kelvin. Spycher *et al.* (2003) found values for the parameters k_0, k_1 and b, by fitting Eq. (3.2) to empirical data for CO_2 and H_2O. These are shown in Table 3.1.

Molar volume, V, can be converted to CO_2 density, ρ_{CO_2}, using the following equation:

Parameter	Value	Units
a_{CO2}	7.54×10^7 - $4.13 \times 10^4 \times T$	bar cm^6 $K^{0.5}$ mol^{-2}
b_{CO2}	27.80	cm^3 mol^{-1}
b_{H2O}	18.18	cm^3 mol^{-1}
$a_{H2O-CO2}$	7.89×10^7	bar cm^6 $K^{0.5}$ mol^{-2}
R	83.1447	bar cm^3 K^{-1} mol^{-1}

Table 3.1: Parameters for Eq. (3.2), P is in bar, T is in Kelvin and V is in cm^3

$$\rho_{CO_2} = \frac{M_{CO_2}}{V} \tag{3.4}$$

where M_{CO_2} is the molar mass of CO_2 which is 44.0 g mol^{-1} and ρ_{CO_2} is given in g cm^{-3}.

Solving Eq. (3.2) for V is fairly difficult as it involves the solution of a cubic equation (see Spycher *et al.* (2003) eq. B8). An alternative approach is to specify a range of densities along with a value for temperature, and then to use Eq. (3.2) to calculate corresponding values of pressures for those densities at that temperature. Subsequently a lookup table can be used to find density at pressure P. (See Section 3.5). The variation of CO_2 density with pressure, when $T = 40°C$, is shown in Fig. 3.1.

ECO2N uses CO_2 density values based on correlations from Altunin (1975). Fig. 3.1 shows a small variation between the CO_2 density calculated using the different methods. The correlation of Spycher *et al.* (2003) is implemented in the MATLAB model as it is relatively simple to implement.

3.1.2 Density of brine

Brine density has been calculated using the following equations derived by Batzle & Wang (1992) by fitting empirical data :

$$\begin{aligned}\rho_{H_2O} =& 1 + 10^{-6}\left(-80T - 3.3T^2 + 0.00175T^3 + 489P\right. \\ & \left. -2TP + 0.016T^2P - 1.3 \times 10^{-5}T^3P - 0.333P^2 - 0.002TP^2\right)\end{aligned} \tag{3.5}$$

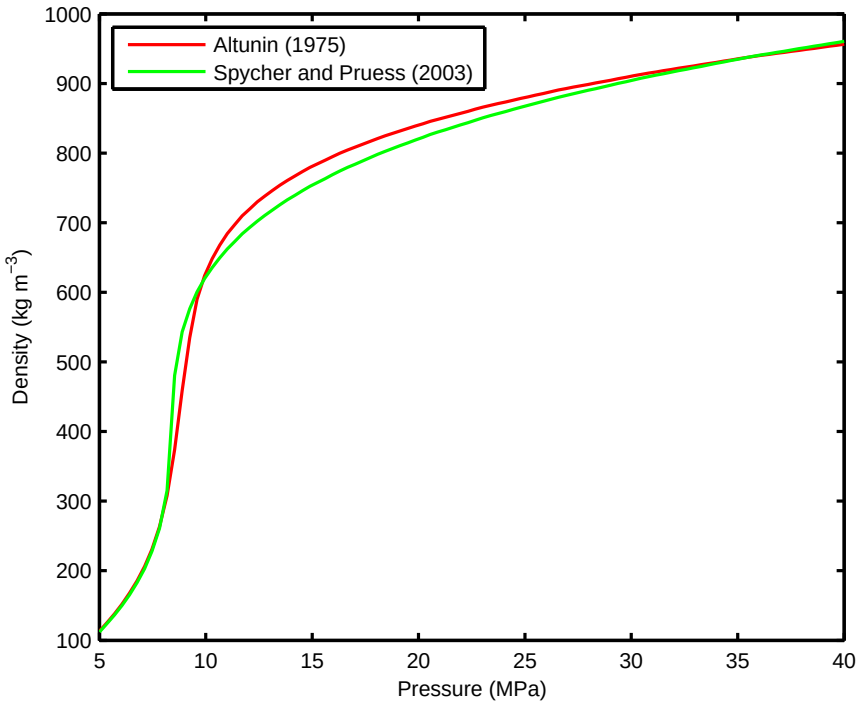

Figure 3.1: CO_2 density vs pressure for $T = 40°C$

$$\rho_{brine} = \rho_{H_2O} + X_s\,(0.668 + 0.44S \\ +10^{-6}\,(300P - 2400PS + T\,(80 + 3T - 3300X_s - 13P + 47PX_s))) \tag{3.6}$$

where T is temperature in °C, P is pressure in MPa, X_s is salt mass fraction and densities ρ_{H_2O} and ρ_{brine} are given in g cm^{-3}. Variation of brine density with pressure is shown in Fig. 3.2 for T = 40°C.

Brine density is modelled in ECO2N using the correlations of Haas Jr (1976). However the equation presented by Batzle & Wang (1992) has been used in the MATLAB model as it has been shown to be particularly accurate in intercomparison studies (Adams & Bachu, 2002). Brine density as calculated by Haas Jr (1976) is also shown in Fig. 3.2 for comparison purposes.

3.1.3 Density of liquid phase CO_2-H_2O mixtures

The density of the aqueous phase, H_2O with dissolved CO_2, is described by the following mixing law :

$$\rho_a = \left(\frac{x_{ca}}{\rho_{ca}} + \frac{x_{wa}}{\rho_{wa}} \right)^{-1} \tag{3.7}$$

where x_{ca} is the equilibrium mass fraction of CO_2 in the aqueous phase, x_{wa} is the equilibrium mass fraction of H_2O in the aqueous phase, ρ_{ca} is the partial density of CO_2 in the aqueous phase and ρ_{wa} is the partial density of H_2O in the aqueous phase.

The partial density of CO_2 in the aqueous phase is found using the equation for partial molar volume of CO_2 in water given by Garcia (2001):

$$V = 37.51 - 9.585 \times 10^{-2} T + 8.740 \times 10^{-4} T^2 - 5.044 \times 10^{-7} T^3 \tag{3.8}$$

in conjunction with Eq. (3.4).

This formulation does not take into account the dependence of partial density of CO_2 on dissolved salt concentration. Also, the dependence of partial density on pressure is neglected. The same relations are used in ECO2N.

Fig. 3.2 also shows density of the aqueous phase with dissolved CO_2 at equilibrium concentration for $T = 40°C$ and $X_s = 0.105$. Note that aqueous phase density increases with dissolved CO_2 content.

3.1.4 Density of gaseous phase CO_2-H_2O mixtures

In both the MATLAB model and in ECO2N it is assumed that the effect of dissolved H_2O on the density of the gaseous phase is negligible. Therefore ρ_g is taken as the density of pure CO_2 which is calculated as described above (Section 3.1.1).

3.2 Viscosity

3.2.1 Viscosity of CO_2

CO_2 viscosity has been modelled using a simplified version of the empirical relations provided by Fenghour *et al.* (1998) (Mathias *et al.*, 2009b):

$$\mu_{CO_2} = 16.485 + (0.0094870\rho_{CO_2})^2 + (0.0025939\rho_{CO_2})^4 + (0.0019815\rho_{CO_2})^6 \tag{3.9}$$

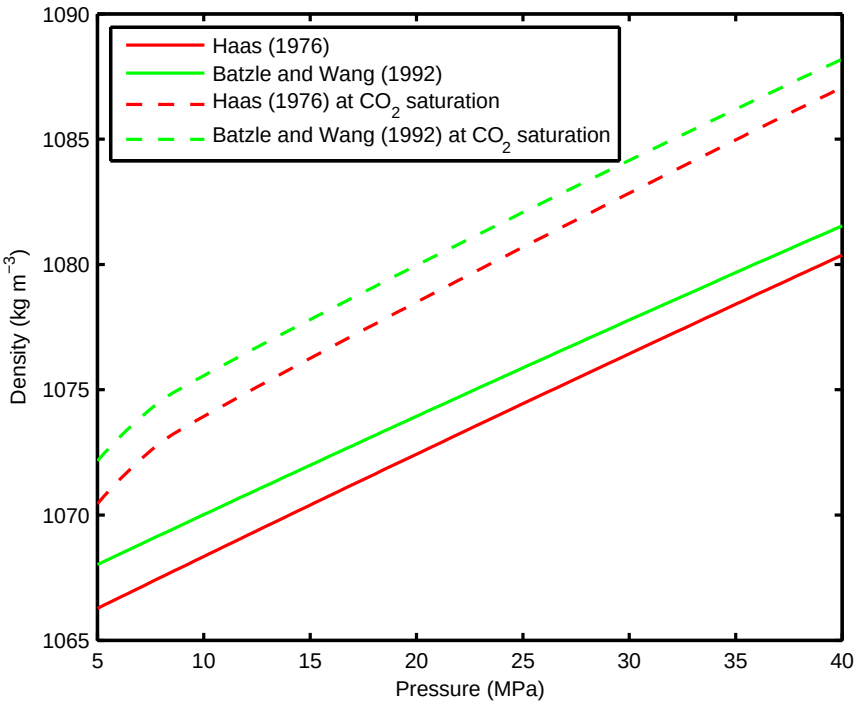

Figure 3.2: Aqueous phase density variation with P for $T = 40°$C and salt mass fraction, $X_s = 0.105$

The units of μ_{CO_2} are μPa s and the units of ρ_{CO_2} are kg m $^{-3}$. ECO2N uses CO_2 viscosity values provided by Altunin (1975). Eq. (3.9) and Altunin (1975) provide a good approximation to the viscosity calculated from Fenghour *et al.* (1998) in the temperature range 238 K $\leq$ T $\leq$ 380 K (Fig. 3.3). Fig. 3.4 shows the variation of CO_2 viscosity with pressure. The difference in viscosity between the correlations of Mathias *et al.* (2009b) and Altunin (1975) is small.

3.2.2 Viscosity of brine

Adams & Bachu (2002) recommend the use of relations provided by Kestin *et al.* (1981) for calculating brine viscosity, μ_b. The MATLAB model uses brine viscosity given by Batzle & Wang (1992) which is a simplified approximation to the relation of Kestin *et al.* (1981) for temperatures below 250 °C:

$$\mu_b = 0.1 + 0.333X_s + (1.65 + 91.9X_s^3)\exp\{-(0.42(X_s^{0.8} - 0.17)^2 + 0.045)T^{0.8}\} \qquad (3.10)$$

where X_s is salt mass fraction T is given in °C and μ_b is given in mPa s.

In Eq. (3.10), the viscosity is only a function of temperature and salinity. This is considered

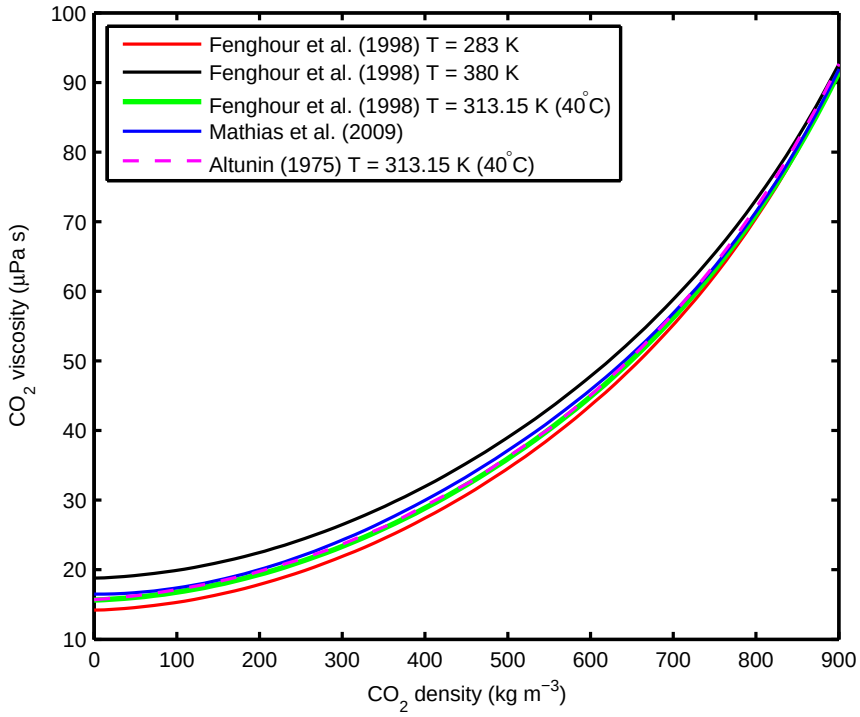

Figure 3.3: Comparison of CO_2 viscosity calculated using Fenghour *et al.* (1998), Altunin (1975) and CO_2 viscosity calculated using Eq. (3.9).

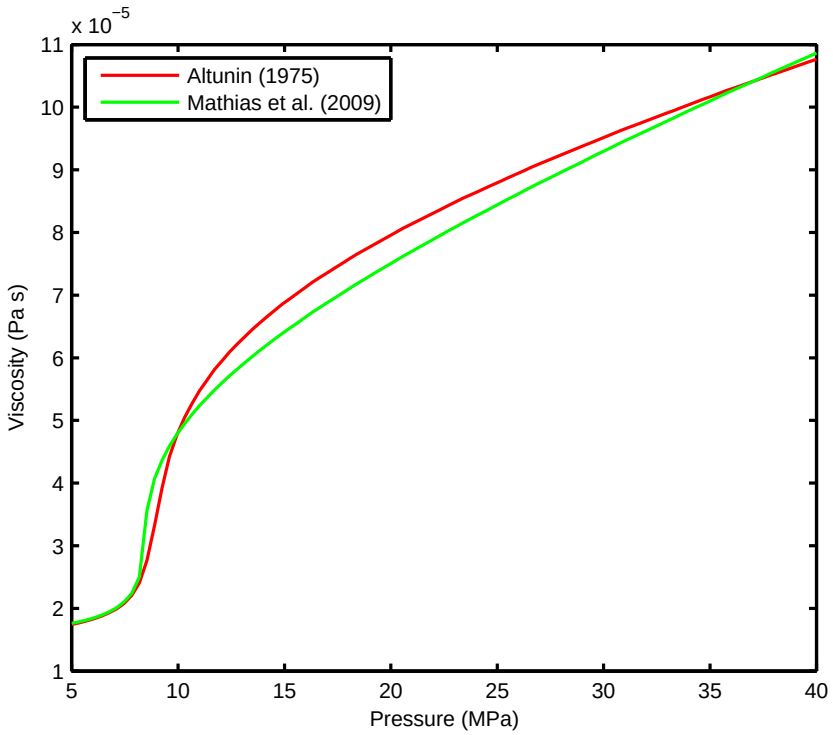

Figure 3.4: CO_2 viscosity variation with pressure at $T = 40$ °C, $X_s = 0.105$.

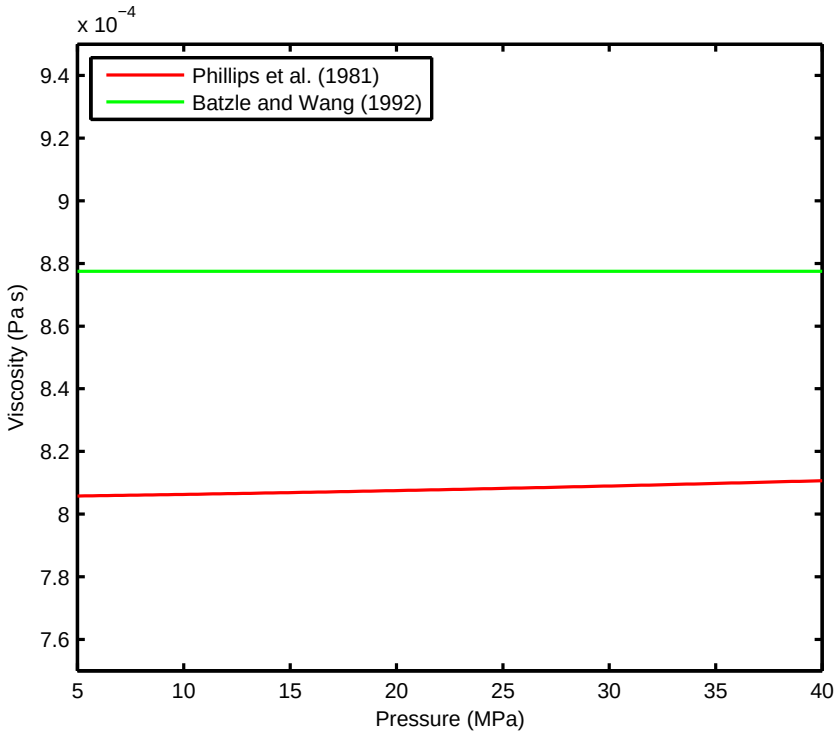

Figure 3.5: Brine viscosity variation with pressure at $T = 40$ °C.

a reasonable assumption as brine viscosity only has a very small dependence on pressure relative to its dependence on temperature and salinity. ECO2N uses correlations presented in Phillips (1981). Fig. 3.5 shows that in absolute terms there is only a small difference between the two correlations.

3.2.3 Viscosity of liquid phase CO_2-H_2O mixtures

CO_2 solubility in the aqueous phase is small (Spycher *et al.*, 2003) so the viscosity of the aqueous phase, in both the MATLAB model and ECO2N, is taken to be that of brine with no dissolved CO_2 (see Section 3.2.2).

3.2.4 Viscosity of gaseous phase CO_2-H_2O mixtures

Viscosity of the gaseous phase in both the MATLAB model and ECO2N is taken to be that of pure CO_2 (see Section 3.2.1), as the solubility of H_2O in the gaseous phase is small (Spycher *et al.*, 2003).

3.3 Compressibility

3.3.1 CO_2 compressibility

CO_2 compressibility, used in Eq. (6.50), is calculated using the following equation (Bear, 1989):

$$c_{CO_2} = \frac{1}{\rho_{CO_2}} \frac{\partial \rho_{CO_2}}{\partial P_{CO_2}} = -\frac{1}{V_{CO_2}} \frac{\partial V_{CO_2}}{\partial P_{CO_2}} \tag{3.11}$$

At constant temperature:

$$\frac{\partial V_{CO_2}}{\partial P_{CO_2}} = \left(\frac{\partial P_{CO_2}}{\partial V_{CO_2}} \right)^{-1} \tag{3.12}$$

and differentiation of Eq. (3.2) gives:

$$\frac{\partial P_{CO_2}}{\partial V_{CO_2}} = -\left(\frac{RT}{(V-b)^2} \right) + \left(\frac{a(2V+b)}{T^{0.5} V^2 (V+b)^2} \right) \tag{3.13}$$

3.3.2 Brine compressibility

Brine compressibility, used in Eq. (6.50), is given by:

$$c_b = \frac{1}{\rho_b} \frac{\partial \rho_b}{\partial P_b} \tag{3.14}$$

Differentiation of Eqs. (3.5) and (3.6) leads to:

$$\frac{\partial \rho_{H_2O}}{\partial P_{H_2O}} = 10^{-6} \left(489P - 2T + 0.016T^2 - 1.3 \times 10^{-5} T^3 - 0.666P - 0.004TP \right) \tag{3.15}$$

$$\frac{\partial \rho_b}{\partial P_b} = \frac{\partial \rho_{H_2O}}{\partial P_{H_2O}} + X_s \{ 10^{-6} \left[300 - 2400 X_s + T \left(-13 + 47 X_s \right) \right] \} \tag{3.16}$$

3.3.3 Phase compressibilities

Phase compressibilities for multicomponent mixtures are calculated using Eq. (6.50) described in Chapter 6.

3.4 Composition of CO_2-H_2O-NaCl mixtures

This section describes the mutual solubility correlations proposed in Spycher *et al.* (2003); Spycher & Pruess (2005) which have been used in the MATLAB model. Derivations of the thermodynamics equations are based on the work of Denbigh (1957) and Smith (2002) where they are described in more detail.

The thermodynamic system in question contains two phases (gaseous and aqueous) and three components (CO_2, H_2O and NaCl). The components CO_2 and H_2O are able to move between phases. The NaCl component is only able to exist in the aqueous phase.

When the two phases are present some CO_2 molecules will dissolve into the aqueous phase and some H_2O molecules will evaporate into the gaseous phase.

For a specified pressure, temperature and brine salinity there is an equilibrium concentration of each component in each phase which defines the maximum concentration of each component in each phase. For instance, if only the aqueous phase was initially present but the concentration of CO_2 within it was raised above the equilibrium concentration, a separate gaseous phase would form and two phase conditions would exist. Equilibrium concentrations are required at the pressure, temperature and salinity conditions being modelled in order to track the appearance and disappearance of single phase and two phase conditions (see Section 6.3).

3.4.1 Gibbs energy and chemical potential

If a thermodynamic system is in chemical equilibrium then for each component the chemical potential of that component is equal in each phase. Chemical potential, μ_i, is defined in terms of the Gibbs energy, G. Gibbs energy is the amount of energy available in the system for doing non-expansion work e.g. the amount of energy available for things like chemical reactions.

Thermodynamics deals with changes in energy in a system as opposed to absolute values of energy. The change in Gibbs energy of a system is given by (Smith, 2002, Pg. 49):

$$dG = VdP - SdT + \sum_i \mu_i dn_i \tag{3.17}$$

where V is volume, P is pressure, S is entropy, T is temperature, n_i is the number of moles of component i and:

$$\mu_i = \left(\frac{\partial G}{\partial n_i}\right)_{T,P,n_j} \tag{3.18}$$

Eq. (3.18) states that the chemical potential of component i is the change in Gibbs energy of a system when an infinitesimal amount of component i is added to the system *without* having a noticeable effect on the overall composition of the the system.

Gibbs energy cannot be measured directly so an expression for chemical potential in terms of measurable quantities is needed.

At constant temperature and composition Eq. (3.17) becomes:

$$dG = VdP \tag{3.19}$$

and the change in Gibbs energy with pressure is:

$$\left(\frac{\partial G}{\partial P}\right)_{T,n_i} = V \tag{3.20}$$

Taking the derivative of Eq. (3.20) with respect to n_i leads to:

$$\frac{\partial}{\partial n_i}\left(\frac{\partial G}{\partial P}\right)_{T,n_j} = \left(\frac{\partial V}{\partial n_i}\right)_{T,P,n_j} \tag{3.21}$$

$$\left(\frac{\partial \mu_i}{\partial P}\right)_{T,n_i,n_j} = \bar{V}_i \tag{3.22}$$

where $\bar{V}_i$ is the partial molar volume of component i defined as (Smith, 2002, Pg. 51):

$$\bar{V}_i = \left(\frac{\partial V}{\partial n_i}\right)_{T,P,n_j} \tag{3.23}$$

Substituting the equation of state for an ideal gas, Eq. (3.1), into Eq. (3.22) leads to:

$$d\mu_i = \bar{V}_i = RT\frac{dP}{P} \tag{3.24}$$

because:

$$V = \sum_i n_i \bar{V}_i \qquad \text{and} \qquad \sum_i n_i = n \tag{3.25}$$

μ_i is then found by the taking the definite integral of Eq. (3.24) with respect to P, between an arbitrary reference pressure P^0 and P:

$$\begin{aligned}
\int_{P^0}^{P} d\mu_i dP &= RT \int_{P^0}^{P} \left(\frac{dP}{P}\right) dP \\
[\mu_i]_{P^0}^{P} &= [RT\ln(P)]_{P^0}^{P} \\
\mu_i - \mu_i^0 &= RT\ln(P) - RT\ln(P^0) \\
\mu_i &= \mu_i^0 + RT\ln\left(\frac{P}{P^0}\right)
\end{aligned} \tag{3.26}$$

where μ_i^0 is the chemical potential of the pure gas i at conditions (P^0, T) and is independent of composition. We now have an equation for the chemical potential of the gas i in terms of measureable quantities (Eq. (3.26))

3.4.2 Chemical potential of gas mixtures

For mixtures of gases, partial pressure, P_i, is defined as:

$$P_i = y_i P \tag{3.27}$$

where y_i is the mole fraction of component i in the gas mixture.

By definition the chemical potential of an ideal gas mixture is given by (Denbigh, 1957, Eq. 3.18):

$$\mu_i = \mu_i^0 + RT \ln\left(\frac{P}{P^0}\right) + RT \ln y_i \tag{3.28}$$

As P^0 is arbitrary it can be chosen such that it is equal to 1 in the relevant units. Assuming $P^0 = 1$, Eq. (3.28) can be written as:

$$\mu_i = \mu_i^0 + RT \ln\left(P_i\right) \tag{3.29}$$

For a non-ideal gas mixture Eq. (3.1) only holds in the limit of zero pressure. To account for this in Eq. (3.29) we define a new term, fugacity f_i, which replaces the partial pressure:

$$\mu_i = \mu_i^0 + RT \ln\left(f_i\right) \tag{3.30}$$

$$\phi_i = \frac{f_i}{P_i} \to 1 \qquad \text{as} \qquad P \to 0 \tag{3.31}$$

where ϕ_i is defined as the fugacity coefficient of component i. The limit means that for an ideal gas mixture ϕ is equal to 1 and f_i is equal to P_i.

3.4.3 Chemical potential of solutions

As well as gas mixtures, we are also concerned with the chemical potential of components in solution. An ideal solution is defined as one where the chemical potential of each component is related to its mole fraction in the solution, x_i, by:

$$\mu_i = \mu_i^\star + RT \ln x_i \tag{3.32}$$

where $\mu_i^\star$ is the chemical potential of pure component i at conditions (P, T) (and is therefore independent of composition).

To account for the deviation from ideality we can define the activity coefficient, γ_{xi}, analogous to the fugacity coefficient, such that (Denbigh, 1957, Eq. 9.1):

$$\mu_i = \mu_i^\star + RT \ln \gamma_{xi} x_i \tag{3.33}$$

The behaviour of component i in a real solution approaches ideal either when $x_i \to 1$, pure component i, or when $x_i \to 0$, infinite dilution of component i.

Often the activity coefficient of a solute is quoted on a molality scale (moles of solvent per 1000 grams of solute), by convention then the complete definition of the chemical potential of components in a real solution is (Denbigh, 1957, Eq. 9.16):

$$\text{for a solvent:} \quad \mu_i = \mu_i^\star + RT \ln \gamma_{xi} x_i \quad \text{and} \quad \gamma_0 \to 1 \quad \text{as} \quad x_i \to 1 \tag{3.34}$$

$$\text{for a solute:} \quad \mu_i = \mu_i^\diamond + RT \ln \gamma_{mi} m_i \quad \text{and} \quad \gamma_i \to 1 \quad \text{as} \quad m_i \to 0 \tag{3.35}$$

where the solvent is defined as a component whose mole fraction can take any value between 0 and 1 without a change of phase. $\mu_i^\diamond$ is the chemical potential of a hypothetical ideal solution with unit molality at conditions (P, T). m_i is the molality of component i. γ_{xi} and γ_{mi} refer to the activity coefficient of component i on a mole fraction scale and a molality scale respectively.

We can also define the activity of component i:

$$\text{for a solvent:} \quad a_{xi} = \gamma_{xi} x_i \tag{3.36}$$

$$\text{for a solute:} \quad a_{mi} = \gamma_{mi} m_i \tag{3.37}$$

where a_{xi} is activity on a mole fraction scale and a_{mi} is activity on a molality scale. This leads to the expression for the chemical potential of i in a real solution:

$$\text{for a solvent:} \qquad \mu_i = \mu_i^\star + RT \ln a_{xi} \tag{3.38}$$

$$\text{for a solute:} \qquad \mu_i = \mu_i^\diamond + RT \ln a_{mi} \tag{3.39}$$

3.4.4 Equilibrium constants

We now have expressions for the chemical potential of component i in the gaseous phase (Eq. (3.30)) and component i in the aqueous phase (Eqs. (3.38) and (3.39)). At equilibrium the chemical potential of component i in each phase is equal therefore:

$$\text{for a solvent:} \qquad \mu_i^0 + RT \ln f_i = \mu_i^\star + RT \ln a_{xi} \tag{3.40}$$

$$\text{for a solute:} \qquad \mu_i^0 + RT \ln f_i = \mu_i^\diamond + RT \ln a_{mi} \tag{3.41}$$

Rearrangement of Eqs. (3.40) and (3.41) leads to:

$$\text{for a solvent:} \qquad K_i = \frac{f_i}{a_{xi}} = \exp\left[(\mu_i^0 - \mu_i^\star)\frac{1}{RT}\right] \tag{3.42}$$

$$\text{for a solute:} \qquad K_i = \frac{f_i}{a_{mi}} = \exp\left[(\mu_i^0 - \mu_i^\diamond)\frac{1}{RT}\right] \tag{3.43}$$

where K_i is known as the equilibrium constant. As μ_i^0, $\mu_i^\star$ and $\mu_i^\diamond$ are functions of (P,T) only it follows that K_i is also a function of only (P,T).

In the system being modelled equilibrium constants for H_2O and CO_2 are as follows (Spycher *et al.*, 2003):

$$K_{H_2O} = \frac{f_{H_2O(g)}}{a_{H_2O(l)}}, \qquad K_{CO_2(g)} = \frac{f_{CO_2(g)}}{a_{CO_2(aq)}} \tag{3.44}$$

Substitution of Eqs. (3.27), (3.31), (3.36) and (3.37) into Eq. (3.44) gives:

$$K_{H_2O} = \frac{\phi_{H_2O} y_{H_2O} P}{\gamma_{H_2O} x_{H_2O}}, \qquad K_{CO_2(g)} = \frac{\phi_{CO_2} y_{CO_2} P}{\gamma_{CO_2} m_{CO_2}} \tag{3.45}$$

We can also find $K_{CO_2(g)}$ in terms of mole fraction of CO_2, x_{CO_2}, by finding $a_{CO_2(aq)}$ on a mole fraction scale instead of a molality scale as described below (also see Denbigh, 1957, Sec. 9.4).

Regardless of the scale it is defined on, the chemical potential of component i in a particular phase at (P, T) is the same. Therefore:

$$\mu_i = \mu_i^\star + RT \ln \gamma_{xi} x_i = \mu_i^\diamond + RT \ln \gamma_{mi} m_i \tag{3.46}$$

where γ_{xi} is the activity coefficient of component i on a mole fraction scale and γ_{mi} is the activity coefficient of component i on a molality scale. Rearranging Eq. (3.46) leads to:

$$RT \ln \frac{\gamma_{mi} m_i}{\gamma_{xi} x_i} = \mu_i^\star - \mu_i^\diamond \tag{3.47}$$

Molality of component i is given by:

$$m_i = \frac{n_i}{n_0} \times \text{moles in 1 kg of solvent} = \frac{n_i 1000}{n_0 M_0} \tag{3.48}$$

where n_i is the number of moles of solute present, n_0 is the number of moles of solvent present and M_0 is the weight of a mole of solvent in grams.

Mole fraction of component i is given by:

$$x_i = \frac{n_i}{n_0 + \sum n_i} \tag{3.49}$$

where $\sum n_i$ is the sum of moles of all components in solution. For high dilution $\sum n_i \to 0$ and:

$$\frac{m_i}{x_i} \approxeq \frac{1000}{M_0} \tag{3.50}$$

Under limiting conditions of high dilution $\gamma_{xi} = \gamma_{mi} = 1$ and Eq. (3.47) reduces to:

$$RT \ln \frac{m_i}{x_i} = \mu_i^\star - \mu_i^\diamond \tag{3.51}$$

Using Eqs. (3.47), (3.50) and (3.51) we have:

$$RT \ln \frac{1000}{M_0} = RT \ln \frac{\gamma_{mi} m_i}{\gamma_{xi} x_i} \tag{3.52}$$

Then the relationship between γ_{xi} and γ_{mi} is given by:

$$\frac{\gamma_{mi}}{\gamma_{xi}} = \frac{1000 x_i}{M_0 m_i} \tag{3.53}$$

The activity on a molality scale assuming unit activity coefficient on a mole fraction scale is:

$$a_{CO_2} = \gamma_{mi} m_{CO_2} = \frac{1000 x_{CO_2}}{M_0} = 55.508 x_{CO_2} \tag{3.54}$$

where $M_0 = 18.01528$.

Eq. (3.54) is the activity of CO_2 in pure water at infinite dilution. In our model the solvent also contains dissolved NaCl. To account for this we introduce the activity coefficient for aqueous CO_2 in brine, γ', into Eq. (3.54):

$$a_{CO_2} = 55.508 \gamma' x_{CO_2} \tag{3.55}$$

with the convention that $\gamma' \to 1$ as $x_{NaCl} \to 0$. γ' is calculated from empirical data (see Eq. (3.66)).

3.4.5 Calculation of mole fractions from equilibrium constants

Expressions for equilibrium constants, fugacity coefficients and activity coefficients in terms of P and T can be found, allowing us to calculate the unknown mole fractions in Eq. (3.45).

At constant temperature, rearrangement of Eq. (3.42) and substitution into Eq. (3.22) leads to the following equation linking the equilibrium constant with pressure and temperature (Denbigh, 1957, Sec. 8.6):

$$\left(\frac{\partial \ln K_i}{\partial P}\right)_T = \frac{\bar{V}_i}{RT} \tag{3.56}$$

Integration of Eq. (3.56) with respect to pressure between P^0 and P gives:

$$\begin{aligned}
\int_{P^0}^{P} \left(\frac{\partial \ln K}{\partial P}\right)_T &= \int_{P^0}^{P} \frac{\bar{V}_i}{RT} \\
\ln\left(\frac{K}{K^0}\right) &= \frac{\bar{V}_i}{RT}(P - P^0) \\
K &= K^0 \exp\left(\frac{\bar{V}_i}{RT}(P - P^0)\right)
\end{aligned} \tag{3.57}$$

Substitution of K_{H_2O} from Eq. (3.45) and rearrangement leads to the following expression for the mole fraction of H_2O in the gaseous phase:

$$\begin{aligned}
y_{H_2O} &= \frac{K^0_{H_2O}\gamma_{H_2O}}{\phi_{H_2O}P}\left[\exp\left(\frac{\bar{V}_{H_2O}}{RT}(P - P^0)\right)\right](1 - x_{CO_2} - x_{NaCl}) \\
&= A(1 - x_{CO_2} - x_{NaCl})
\end{aligned} \tag{3.58}$$

Similarly:

$$\begin{aligned}
x_{CO_2} &= \frac{\phi_{CO_2}P}{K^0_{CO_2}55.508\gamma'}\left[\exp\left(-\frac{\bar{V}_{CO_2}}{RT}(P - P^0)\right)\right](1 - y_{H_2O}) \\
&= B(1 - y_{H_2O})
\end{aligned} \tag{3.59}$$

where A and B are:

$$A = \frac{K^0_{H_2O}\gamma_{H_2O}}{\phi_{H_2O}P}\left[\exp\left(\frac{\bar{V}_{H_2O}}{RT}(P-P^0)\right)\right] \tag{3.60}$$

$$B = \frac{\phi_{CO_2}P}{K^0_{CO_2}55.508\gamma'}\left[\exp\left(-\frac{\bar{V}_{CO_2}}{RT}(P-P^0)\right)\right] \tag{3.61}$$

We now have two equations and two unknowns which can be solved by substituting Eq. (3.59) into Eq. (3.58) and rearranging to get:

$$y_{H_2O} = \frac{(1-B-x_{NaCl})}{1/A-B} \tag{3.62}$$

The equation for salt mole fraction, x_{NaCl}, is:

$$x_{NaCl} = \frac{vm_{NaCl}}{55.508 + vm_{NaCl} + m_{CO_2}} \tag{3.63}$$

where v is the stoichiometric number of ions in the dissolved salt (for NaCl, $v = 2$), m_{NaCl} is the molality of NaCl in the aqueous solution and m_{CO_2} is the molality of CO_2 in the aqueous solution

CO_2 molality in the aqueous solution given by Eq. (3.48) where the number of moles of solute present is the number of moles of H_2O plus the number of moles of Na and the number of moles of Cl:

$$m_{CO_2} = \frac{x_{CO_2}}{(1-x_{CO_2})}(vm_{NaCl} + 55.508) \tag{3.64}$$

Substitution of Eqs. (3.59), (3.63) and (3.64) into Eq. (3.62) gives:

$$y_{H_2O} = \frac{(1-B)55.508}{(1/A-B)(vm_{NaCl}+55.508)+vm_{NaCl}B} \tag{3.65}$$

Values for $K^0_{H_2O}$, $K^0_{CO_2}$, ϕ_{H_2O}, ϕ_{CO_2}, $\bar{V}_{H_2O}$ and $\bar{V}_{CO_2}$ have been taken from Spycher *et al.* (2003). P^0 is taken as 1 bar, the water activity coefficient γ_{H_2O} is assumed to be 1. The CO_2

activity coefficient is taken from the equation for activity coefficient proposed by Duan & Sun (2003) and given in Spycher & Pruess (2005):

$$\ln(\gamma') = 2\lambda(m_{Na}) + \xi m_{Cl}(m_{Na}) \tag{3.66}$$

where m_{Na} and m_{Cl} are the molalities of Na and Cl and are equal to m_{NaCl}. λ and ξ are given by:

$$\begin{aligned}\lambda = &-0.411370585 + 6.07632013 \times 10^{-4}T + 97.5347708/T \\ &- 0.0237622469P/T + 0.0170656236P/(630 - T) + 1.41335834 \times 10^{-5}T\ln(P)\end{aligned} \tag{3.67}$$

$$\begin{aligned}\xi = &\ 3.36389723 \times 10^{-4}T - 1.98298980 \times 10^{-5}T \\ &+ 2.12220830 \times 10^{-3}P/T + 5.24873303 \times 10^{-3}P/(630 - T)\end{aligned} \tag{3.68}$$

where P is in bars and T is in Kelvin.

3.5 EOS Implementation

In the MATLAB model a lookup table of fluid properties has been generated for a range of pressures and for a specific temperature. During simulations fluid properties are found using linear interpolation of the data in the table based on the model pressure. This reduces the computational effort required at each time step as the fluid properties only need to be calculated once when generating the table.

Chapter 4

Dynamic modelling of a UK North Sea saline formation for CO_2 sequestration

Summary

This chapter describes preliminary dynamic modelling, using TOUGH2/ECO2N, carried out to assess the suitability of a site in the UK North Sea for sequestering CO_2. The site in question is a previously unused saline formation; therefore, data regarding the site are limited. The main objectives of the work were:

1. To find out if the site could sustain a particular CO_2 injection rate (2.5 Mt a^{-1} for 20 years) without CO_2 migrating out of the trap or the fluid pressure exceeding the caprock fracture pressure.

2. To determine the factors which have the largest impact on the CO_2 migration and pressure buildup.

3. To assess the utility of dynamic simulations where not much data about the proposed site is available and there are many uncertainties in the input data.

Large scale, fully 3D models incorporating the reservoir geometry were used. However, the models were simplified in some respects (i.e. no dissolution modelling, no detailed modelling

of the injection process) to allow us to concentrate on meeting the objectives described above and producing realistic results based on the available data.

A version of this chapter is published in the following article:

> Watson, F. E., Mathias, S. A., Daniels, S. E., Jones, R. R., Davies, R. J., Hedley, B. J., & van Hunen, J. (2014). Dynamic modelling of a UK North Sea saline formation for CO_2 sequestration. *Petroleum Geoscience*, 20(2), 169-185.

All TOUGH2 models were built, run and analysed by myself. Write up of the work was carried out by myself. Model input parameters were researched and collated by Ben Hedley. Seismic interpretation to determine the geometry of the reservoir was undertaken by Ben Hedley. Additional support relating to constructive criticism of the manuscript and overall project management was provided by the other authors.

4.1 Introduction

Deep saline formations are one possible storage option for CO_2 as they contain large volumes of pore space and are regionally extensive (Metz *et al.*, 2005). One of the advantages of using previously unused saline formations for CO_2 storage is the fact that they may have a reduced well density compared with oil or gas fields. Therefore, the number of man made leakage pathways is reduced. This is also a disadvantage as it means that there is limited data available about the formation for site-scale characterisation.

The EU directive (European Union, 2009) requires the screening of a range of sites in order to identify those which are promising for CO_2 storage. Potential storage sites, chosen from preliminary screening, then need to be fully characterised using static and dynamic computer simulations which should demonstrate storage capacity, pressure buildup and CO_2 migration pathways. A site can only be used for CO_2 storage if the site characterisation indicates that the risk of CO_2 leakage is insignificant and that there are no significant risks to human health or the environment. This paper describes a preliminary site characterisation, undertaken for a deep saline formation in the North Sea, using a very limited dataset. This comes after the regional screening stage but is prior to the full site characterisation stage of the CO_2 storage workflow described above. The aim of the work is to build a dynamic model with which to assess the potential for CO_2 storage at the proposed site and to identify further data which will be needed before a thorough site assessment can be carried out.

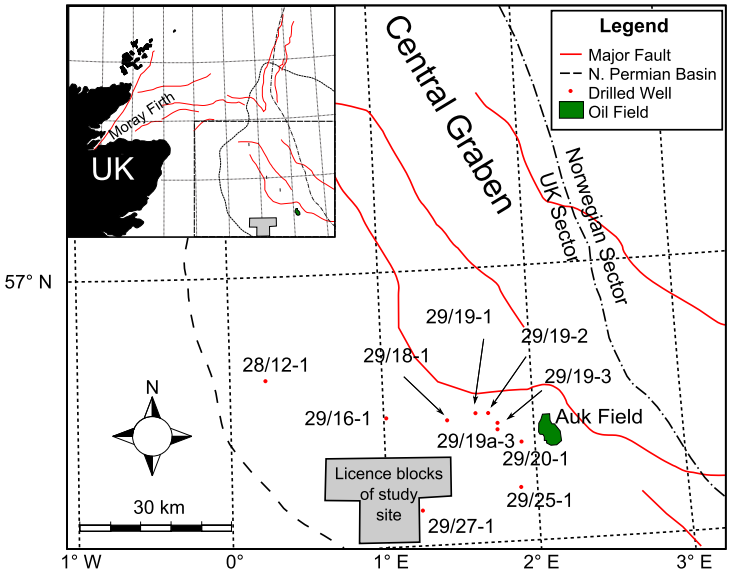

Figure 4.1: Location map of the study site showing well logs used in this study.

The site being considered for CO_2 storage is located in the Central North Sea (Fig. 4.1). It is 50 km west of the Central Graben and 70km north of the Mid North Sea High, on the south western edge of the Northern Permian Basin. This is approximately 200 km North East of the UK Teesside industrial processing region which could provide the source of CO_2. The potential storage formation is the Permian Rotliegend Sandstone with the Permian Zechstein salt providing the cap rock (Glennie, 1983).

The intended preliminary trap within the Rotliegend is referred to hereafter as the CCC Prospect. A 2D seismic survey carried out over the proposed storage site shows that the CCC Prospect consists of a series of interconnected four-way dip closures. It is known that the Rotliegend pinches out to the south west of the site about 30 km away from the CCC Prospect (Fig. 4.2). As the pinchout is updip from the CCC Prospect it could form a secondary trap in the event of CO_2 escaping from the CCC site.

4.2 CO_2 storage in saline formations in the UK North Sea

In order to meet emissions reductions targets the UK may need to store between 2 and 5 billion tonnes of CO_2 before 2050. The Department for Energy and Climate Change estimated that the UK has the potential to store 60 billion tonnes of CO_2 within saline formations in the UK North Sea and the East Irish Sea (DECC, 2012). However, this storage capacity is not well understood and requires further investigation before storage operations can begin.

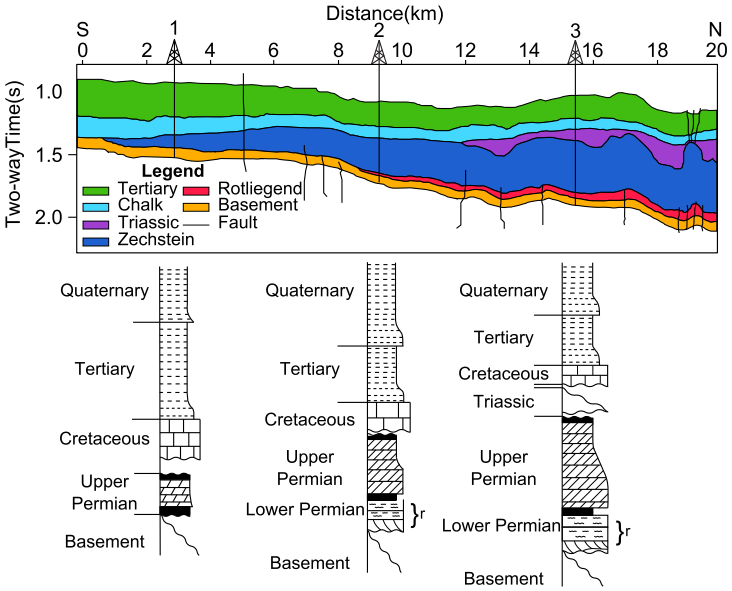

Figure 4.2: Regional structure and stratigraphy based on regional seismic line. Schematic wells show lateral variations in unit thickness. The reservoir interval is denoted (r). After Hedley *et al.* (2013).

Formations within the North Sea have proven ability to store CO_2 both in natural accumulations (Yielding *et al.*, 2011) and as part of a large scale carbon sequestration project (Chadwick *et al.*, 2009a; Boait *et al.*, 2012). Currently there is no injection of CO_2 for storage purposes within the UK North Sea.

Most previously published work regarding CO_2 storage in specific saline formations in the UK North Sea has been associated with the Triassic Bunter Sandstone Formation, within the Southern North Sea. Bentham (2006) estimated the total storage capacity for several structures within the Bunter Sandstone based on their pore volume, CO_2 density at reservoir conditions and a factor representing the proportion of porespace likely to be filled with with CO_2. This factor was derived from a numerical model of a planned CO_2 injection into the Esmond field in the Bunter Sandstone. These estimates were mostly constrained by plume geometry and did not include the potentially limiting effect of pressure buildup on CO_2 injection.

Heinemann *et al.* (2012) estimated the dynamic storage capacity of the Bunter Sandstone by approximating it as a series of identical unit cells each containing an injection well at its centre. The minimum allowable well spacing was determined by finding the minimum cell size where the pressure increase due to injection stayed below some maximum pressure threshold. Estimates calculated in this way, which include the impact of pressure buildup on injection, were 2 - 4 times smaller than the static estimates given by Bentham (2006). Noy *et al.* (2012) modelled a 113 km $\times$ 160 km portion of the Bunter Sandstone and estimate that 15 - 20 Mt

a^{-1} could be stored in it over a 50 year period.

As part of the CASSEM (CO_2 Aquifer Storage Site Evaluation and Monitoring) project two onshore analogues for potential offshore CO_2 storage sites were modelled (Jin *et al.*, 2012). The analogues chosen were the Kinniswood and Knox Pulpit Formations, in the east of Scotland and the Triassic Sherwood Sandstone in the east of England, the second of which is very similar to the Bunter Sandstone. The aim of the CASSEM project was to consider and refine the methods used for site characterisation as opposed to investigating the storage potential of any particular sites. However, they calculated storage efficiencies (the maximum volume of CO_2 stored divided by the total pore volume of the storage site) for the two sites at between 0.46 % and 2.75 %. These efficiencies led to storage capacity estimates of 800 Mt and 2300 Mt which indicate the potential for CO_2 storage at similar sites in the UK North Sea.

Our work investigates the potential pressure buildup and plume migration at a specific, field scale site within a larger, regional scale aquifer, in the UK North Sea. The main objective of the study is to determine if the site is generally capable of storing the desired amount of CO_2 without causing an unsustainable increase in pressure or leading to migration of CO_2 over large distances. This preliminary site investigation will provide information on the feasibility of storing CO_2 at this site and the further data which will be needed to carry out a thorough site investigation. We also describe the methodology used to build a dynamic model for a site with little existing, direct data. The modelling choices made and the reasons behind them are given, providing a useful reference for building similar models in the future.

4.3 Geological Background

After the Carboniferous Variscan Orogeny, north - south extension and thermal subsidence in the North Sea during the Permian formed the Northern and Southern Permian Basins. They are separated by the Mid North Sea High. Rotliegend Sandstone was deposited into the Permian Basins and into the much smaller Moray Firth Basin. In the Late Permian, rifting in the Northern North Sea and rising sea levels led to the opening up of a seaway which allowed the Zechstein Marine Transgression to occur, forming the Permian Zechstein salt (Taylor, 1998). Subsequent east - west extension led to the formation of the Central and Viking Grabens which cross cut the Permian Basins.

4.3.1 Proposed storage site

The CCC prospect is located on the edge of the Northern Permian Basin within the Rotliegend and consists of three interconnected four-way dip closures which can be seen in the depth converted seismic data. It covers an area of 26.5 km^2 and is approximately 2600 m below sea level. The thickness of the storage formation at this point is uncertain as it is not possible to identify the base of the formation on the seismic data. Also, no wells penetrate the base of the Rotliegend in this area. It is estimated that beneath the CCC prospect the Rotliegend is 100 - 300 m thick.

The Rotliegend in our study area consists of Auk Formation deposits. The Auk Formation covers a large part of the Northern Permian Basin and is composed solely of sedimentary rocks. It was deposited at a time when the climate of the region was arid desert. Aeolian sandstones dominate the sequence with some fluvial and lacustrine facies also present. The prominent wind direction at the time was most likely from the north west (Glennie, 1983; Glennie *et al.*, 2003).

The Rotliegend forms a hydrocarbon reservoir in the nearby Auk field (Fig. 4.1). Several studies have characterised the Rotliegend at the Auk field using core data (Heward, 1992; Trewin *et al.*, 2003). Heward (1992) divided the reservoir into several layers with different porosities and permeabilities according to the facies present within them. It is possible that this facies variation is also present in the CCC prospect.

Core data from wells near the storage site indicate that the lithology of the Rotliegend at the site is most likely similar to the fluvial and dune facies seen in the Auk field.

4.3.2 Caprock

The Zechstein Marine Transgression occurred during the late Permian and covered both the Northern and Southern Permian basins. Changes in sea level due to periodic glaciation and retreat led to several cycles of transgression and subsequent evaporation of the Zechstein Sea. This sequence of transgression and evaporation led to the deposition of a thick evaporite layer in the centre of the basin, predominantly composed of halite. A higher proportion of carbonates and anhydrite exists at the shallower edges of the basin. Some dolomitisation has occurred within the basin as a whole. Salt tectonics are common in the thicker, halite sections of the basin (Taylor, 1998). This is when salt layers deform ductilely, mainly in response to differential loading. Causes of differential loading include gravitational forces, displacement of salt bodies relative to each other and changes in thermal gradient (Hudec & Jackson, 2007). The movement

of salt can disrupt the overlying strata potentially creating pathways for fluid leakage.

It is not possible to discriminate between the different Zechstein facies by interpretation of the seismic data. Dolomite rafts can have high porosity but it is thought, from seismic and well data, that there is greater than 800 m thickness of halite above the site which will provide a competent caprock with sufficient sealing capacity. Salt tectonics can clearly be seen in the seismic data to the north east of the proposed storage site.

4.3.3 Base Unit

The Rotliegend in our study area is thought to lie unconformably upon Devonian Old Red Sandstone. This is not known for certain as no wells have penetrated the base of the Rotliegend in this area, however the Rotliegend is directly above Devonian strata in the Auk field (Trewin *et al.*, 2003) and in the Argyll and Innes fields to the east of the storage site (Heward *et al.*, 2003). Alternatively the Rotliegend of the storage site could lie on top of Carboniferous strata. However, it is possible that both the Devonian Old Red Sandstone and Carboniferous rocks in the area have similar porosity and permeability characteristics to the Rotliegend Sandstone.

4.4 Modelling

The model has been built to satisfy in part the requirements of the EU Directive (European Union, 2009), for characterisation of the dynamic behaviour of injected CO_2 in a potential storage site. At present the available input data is not sufficient to provide a complete site characterisation which assesses all aspects required by the EU Directive. The main parameters investigated using this model are the storage capacity of the intended trap, pressure buildup within the storage site and the migration of the CO_2 plume.

A choice of modelling methods for site characterisation is available. The simplest of these are analytical methods which provide analytical solutions for one or two model variables such as storage capacity (Zhou *et al.*, 2008), pressure buildup with CO_2 injection (Mathias *et al.*, 2009a; Zhou *et al.*, 2008; Mathias *et al.*, 2011), or the radius of the CO_2 plume (Nordbotten *et al.*, 2005). These methods are useful as they provide a quick assessment of certain characteristics of a site. However, they require some simplifying assumptions to be made. A common limitation of analytical models is that they are unable to account for heterogeneity in either formation properties or model geometry. As we have access to stratigraphic relief data, in the form of an interpreted seismic layer, we can better model storage capacity, CO_2 migration and pressure

buildup specific to our site using a 3D numerical model which incorporates the geometry data.

3D numerical modelling can be undertaken using several different methods. One potential option is to use streamline based models (Obi & Blunt, 2006; Qi *et al.*, 2009). Here the model domain is split into small grid blocks and a finite difference approximation is used to calculate pressure in each grid block. The pressure field is then used to trace streamlines which show the fluid flow paths within the model. Flow equations are solved in one dimension, along the streamline, for several timesteps to show the migration of different phase saturations within the storage site. After a certain global timestep size the average saturation of each grid block is calculated from the saturation of the streamlines running through it, the pressure field is updated and the locations of the streamlines are retraced. The whole process is then repeated. This method is computationally efficient as the flow equations are only solved in one dimension, along the streamlines. Also, fewer time consuming pressure calculations have to be carried out. However, streamline simulation is only suitable for modelling systems where the pressure, and therefore the location of the streamlines, does not change much during the relatively large pressure timesteps. As our model involves CO_2 injection with no accompanying production, the pressure change in the system is quite large. Consequently, streamline simulations may not be suitable in this context.

Another possible option is to use a vertical equilibrium model (Gasda *et al.*, 2009, 2011; Møll Nilsen *et al.*, 2011). In this method the model domain is discretised in the horizontal direction but only contains one layer in the vertical direction. The fluids in each cell are assumed to be in a gravitationally stable configuration (vertical equilibrium), therefore no flow in the vertical direction is modelled. Horizontal flow in the model is solved-for using Darcys law. The height of the interface between fluid phases (CO_2, CO_2 saturated brine, brine) in each cell can then be found, using an analytical solution based on the phase saturations. This method is more computationally efficient than a full three dimensional model as the flow equations are only solved in two dimensions. It allows the horizontal plume spread and the segregation between the different fluid phases to be modelled. However, the assumption that the storage site is in vertical equilibrium means that it is not possible to account for heterogeneity and anisotropy in the vertical direction. Consequently, a vertical equilibrium model is unsuitable for assessing effects associated with layering within formations, such as those potentially present within the Rotliegend.

In this study, we consider a more conventional 3D, regular, grid based model which uses an integrated finite difference method to solve the flow and transport equations (Narasimhan &

Witherspoon, 1976). This is more computationally expensive than other methods as it requires the model to be discretised into a three dimensional grid and therefore the equations have to be solved for more gridblocks at each timestep. However, the chosen method will enable us to better model the pressure increase during the injection period and to include vertical anisotropy in the form of anisotropic permeability and layering within the model.

Specifically, modelling has been performed using TOUGH2-MP (Zhang *et al.*, 2008), the parallel version of the TOUGH2 numerical code for modelling multiphase flow in porous media (Pruess *et al.*, 1999). It has been used in conjunction with the ECO2N equation of state module (Pruess, 2005), which models mixtures of H2O-CO_2-NaCl and has been designed specifically to represent conditions applicable to CO_2 storage in saline aquifers. Code comparison studies (Pruess *et al.*, 2004) have shown TOUGH2 to be a robust code, capable of modelling complex systems relating to geological storage of CO_2. It is widely used for CO_2 storage simulations (e.g. Chadwick *et al.*, 2009b; Doughty, 2010; Chasset *et al.*, 2011).

The model covers an area of about 15.75 km by 14.25 km. This encompasses the CCC Prospect but does not extend to the stratigraphic pinchout of the Rotliegend which could form a secondary trap in the event of CO_2 escaping laterally from the CCC Prospect. In the interest of reducing the computational cost of modelling it was decided at this early stage to only model the CCC Prospect and the area immediately surrounding it.

The model is rectangular in area. The base of the Rotliegend layer cannot be distingushed in the seismic data. A formation thickness of 320 m has been chosen for the base case model. The relief of the top surface of the model has been interpolated from the depth converted seismic surface of the top of the Rotliegend (Fig. 4.3). As the base of the Rotliegend cannot be seen in the seismic data, the base of the model has been given the same relief as the top of the model.

The available seismic data is old and was interpreted using only sparse coverage of well data picks. This is often the case for CCS modelling studies of previously unused sites (e.g. Noy *et al.*, 2012; Schäfer *et al.*, 2012). Seismic data must be integrated with well data to provide a reasonable estimate of reservoir depth and the thickness of layers within the reservoir. Large uncertainties can be introduced into the data when well data is sparse and well locations are far from the storage site. To address this issue we have varied reservoir thickness in one of the model runs. Other dynamic modelling studies of storage sites within saline formations have used models with flat top and bottom surfaces (Hovorka *et al.*, 2004; Chasset *et al.*, 2011). This is due either to a lack of significant undulation in the surfaces of the modelled units or a lack of seismic data over the modelled site. To assess the impact of using a model with flat surfaces

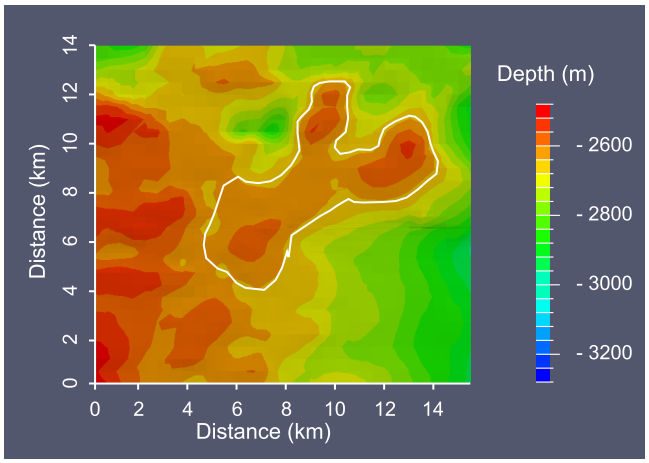

Figure 4.3: Depth map of top of the model, showing model dips to the NE. The white line indicates the approximate outline of CCC Prospect.

we have run some simulations with flat top and bottom surfaces.

The horizontal resolution of the model is 5 m around the injection well increasing to 500m at the edges of the model. To accurately model injection well pressure a very fine horizontal grid resolution ($\approx$ 5 mm) is needed around the injection well (Mathias *et al.*, 2011). As the purpose of our model is to look at the overall capacity of the storage site to store injected CO_2 it was not deemed necessary at this stage to carry out detailed modelling of injection pressures. Therefore, a larger grid resolution near the well bore has been chosen in order to increase the computational efficiency of simulations. This approach of having a relatively large injection cell is taken by several studies investigating field scale effects of CO_2 injection, particularly for models using fully 3D rectangular grids (Doughty, 2010; Noy *et al.*, 2012). Yamamoto *et al.* (2009) used a Voronoi mesh which allowed them to have very fine grid resolution around their modelled injection wells. However, in their study it was important to model the effects of several closely spaced injection wells and the corresponding brine migration caused by the pressure increase around the wells. This is not the case in our work.

Vertical resolution is 1 m for the first 10 m below the caprock. Beneath the top 10 m of the model the vertical resolution is 10 m. Yamamoto & Doughty (2011) showed that a coarse vertical grid resolution reduced the maximum radial plume extent at the top of their model, particularly when the injection rate was low (0.1 Mt a^{-1}). The injection rate in our models is much higher than this. However, the grid resolution has been increased at the top of the model in order to better capture the plume spread at the top of the storage site.

The total number of gridblocks in the base case model is 350714 (94 x 91 x 41).

4.4.1 Initial and boundary conditions

The initial conditions used in the models have been informed by well data and literature data. Where possible, direct data from the Rotliegend formation close to the CCC Prospect have been used. Literature observations regarding nearby analogues and rocks with similar lithologies have been used in preference to more general observations. Empirical observations from the literature have been given priority over theoretical relationships.

Pressure information is available from a pressure study undertaken at the site using nearby well data and published information. The site is thought to be slightly overpressured compared to the hydrostatic pressure gradient. Pressure at the top of the site is $\approx$ 33 MPa. The fracture pressure of the Zechstein caprock is estimated to be 47 MPa. In our models pressure has been set at 33 MPa at a depth of 2600 m and a hydrostatic gradient has been allowed to equilibrate.

A temperature of approximately 90°C, taken from nearby well logs, has been chosen as the formation temperature at 2600 m depth. A geothermal gradient of 30 °C km^{-1} has then been applied to the model. This is a reasonable value for the geothermal gradient in the area of the storage site (Cornford, 1998).

No direct data is available about existing fluids within the formation. We have assumed that the storage site is initially filled with brine. A salinity of 10.5 % has been used similar to the salinity of formation fluids in the Auk field (Trewin *et al.*, 2003). The effect of salt precipitation due to formation dry-out near the injection well (Kim et al. 2012) has not been looked at. This effect has implications for injection pressures but has not been included as we are not carrying out detailed modelling of formation injectivity.

Appropriate boundary conditions are required to model pressure buildup and fluid migration accurately. The thickness of the salt (up to 1 km) and its low permeability mean it is unlikely that CO_2 will leak into the caprock, unless the fracture pressure is exceeded. Therefore a no flow boundary condition has been implemented at the top of the model. The assumption of a no flow boundary at the top seal of the model is frequently used to represent the boundary between a relatively high permeability formation and an extensive, low permeability caprock (Doughty, 2007; Hatzignatiou *et al.*, 2011). Noy *et al.* (2012) show that reducing the permeability of the caprock leads to an increase in the pressure footprint of the plume. Using a no flow boundary condition instead of modelling the caprock essentially reduces the permeability of the caprock to zero, thus allowing a conservative pressure estimate to be made. The advantage of not modelling the caprock explicitly is a reduction in model complexity and associated computation time.

The pressure study of the site suggests that the storage formation is not compartmentalised. To reflect this, an open boundary condition (constant pressure) has been imposed at the lateral edges of the model. The nature of the unit beneath the storage site is unknown although it is suspected to be Devonian Sandstone, similar in nature to the Rotliegend Sandstone. If this is the case, the bottom boundary will probably allow flow across it and should therefore be modelled as an open boundary. Sensitivities have been run with closed base boundaries to look at the extreme case of a very low permeability unit underlying the storage site.

4.4.2 Input parameters

Values for input parameters used for modelling are shown in Table 4.1.

Porosity and permeability data can either be measured directly from cores or be calculated from borehole data. There are various ways of calculating porosity and permeability depending on the data available. Several authors have used depth / porosity correlations and then porosity / permeability correlations of surrounding units to calculate porosity and permeability of the modelled units, based on their depth (Eigestad *et al.*, 2009; Hatzignatiou *et al.*, 2011). This has allowed them to calculate porosity and permeability for areas where no direct porosity and permeability measurements are available.

In our case, porosity values for the Rotliegend are representative values taken from sonic logs of nearby wells and the literature, and are in the range 10 - 27 % with the most likely value being ≈ 19 % (Selley, 1978). Porosity values from the sonic logs were calculated using the equation given by Wyllie *et al.* (1958). No correction was made for clay content as the part of the Rotliegend penetrated by the logs consists of relatively clean quartz arenite.

Horizontal permeability values (k_h) have been taken from core flood data of Rotliegend samples from nearby wells. Permeabilities range from 21 mD (2.07E-14 m^2) for the finely laminated facies, to 33 mD (3.26E-14 m^2) for the massive sand facies, with 28 mD (2.76E-14 m^2) for the diffuse laminated facies, taken as the most likely case. The ratio of vertical to horizontal permeability (k_v/k_h) has been chosen as 0.1. A k_v/k_h of 0.1 is similar to values chosen in several studies to represent the fact that permeabilities in siliciclastic rocks are generally greater parallel to the bedding planes (e.g. Ghomian *et al.*, 2008; Doughty, 2010). The presence of clays within the reservoir would reduce this permeability ratio (Ringrose *et al.*, 2005); however, core data indicates that clay content within the Rotliegend near the CCC Prospect is negligible. Pore compressibility has been estimated using a correlation by (Jalalh, 2006) which was calculated

	Base Case	Ranges Modelled
Pressure	33 MPa	-
Temperature	90 °C	-
Porosity	0.19	0.10 - 0.27
Permeability	28 mD (2.76E-14 m^2)	21 - 33 mD (2.07E-14 - 3.26E-14 m^2)
k_v/k_h	0.1	-
Pore compressibility	1.05E-09 Pa^{-1}*	8.73E-10 Pa^{-1} - 1.05E-09 Pa^{-1}
Relative permeability	Function to fit Viking 2 data†	-
Capillary pressure	Function to fit Viking 2 data†	-
Isothermal	Yes	-
Diffusion	No	-
Reservoir thickness	320 m	120 m - 320 m
Injection interval	40 m	40 m - 70 m
Injection rate	2.5 Mt a^{-1}	-
Simulation time	20 yrs	Post injection - 100 yrs

Table 4.1: Model input parameters. *From Jalalh (2006). †From Bennion *et al.* (2006))

in the laboratory and relates porosity and pore compressibility in sandstones.

Relative permeability and capillary pressure data have come from the laboratory studies on the Viking 2 sandstone by (Bennion *et al.*, 2006). Viking 2 sandstone was chosen as it has similar porosity and permeability values to the estimated values for Rotliegend at our site. The effect of hysteresis, where the multiphase flow properties of the pore space are history dependent, has not been included in our model. Including hysteresis would lead to an increase in residually trapped CO_2 and a reduction in the amount of mobile CO_2 which is able to move through the formation (Doughty, 2007). Consequently CO_2 mobility in our models is at its upper limit, providing a maximum estimate of plume spread.

Temperature change through time and dissolution of CO_2 into the brine have not been modelled. Modelling temperature changes can be important when considering the effect of Joule-Thomson cooling (Oldenburg, 2007; Mathias *et al.*, 2010). This is where CO_2 cools as it undergoes rapid expansion due to a large drop in pressure. This could be the case for injection into a depleted oil or gas reservoir which is at a low pressure but is unlikely to be as important for injection into an aquifer at a pressure similar to that of the injected supercritical CO_2. Dissolution of CO_2 into the resident brine is an important trapping mechanism. However, in the interest of computational efficiency we have chosen not to model dissolution as the effect of dissolution is relatively small during the early stages of CO_2 injection. Prior to the onset of convection, CO_2 can only dissolve in residually trapped brine which is in contact with free-phase CO_2. The amount of CO_2 which can dissolve is controlled by the solubility limit of CO_2 in the brine. CO_2 solubility limit in brine, which is dependent on pressure and temperature

conditions, can be calculated using the equation of state provided by (Spycher and Pruess 2005). Assuming a residual brine saturation of 0.423 (i.e., the Viking 2 core) at 33 MPa and 90°C, the amount of CO_2 expected to dissolve in residually trapped brine would represent around 3.7 % of the total mass of injected CO_2.

The model injection point is located just off crest of the largest dome in the CCC structure, below the depth of the spill point. For operational purposes it would be best to inject CO_2 down dip from the structure to be filled. Buoyancy would then transport the CO_2 to the desired location, allowing more of the reservoir to be swept by the CO_2 and therefore increasing residual trapping. In our preliminary model the injection point is located closer to the crest of the structure than might usually be considered, in order to demonstrate containment within the CCC Prospect. This ensures that all the modelled, injected CO_2 migrates upwards and into the CCC Prospect, at least at the beginning of the simulation.

Injection has been carried out from a vertical well at a rate of approximately 2.5 Mt a^{-1} for 20 years. The completion interval varies from 40 m to 70 m. This interval is purposefully small to allow a more conservative estimate to be made of pressure and CO_2 saturation around the injection point. Post injection modelling for most models has been carried out for up to 100 years. Convergence issues, particularly with the layered models meant this was not possible for all models.

Input parameters for most of the models are uniform throughout the model domain. Some heterogeneous models were run, where differing permeability and porosity values were assigned to layers within the model. However, no allowance was made in any of the models for lateral heterogeneity in the storage site. This is due to a lack of data describing lateral heterogeneity within the site.

4.5 Results

4.5.1 Base Case

Table 4.2 shows the configuration of all models run and a summary of the results.

Fig. 4.4 shows the extent of the CO_2 plume, beneath the top of the storage site, through time for the base case scenario (See Table 4.2, (s01a) - 320 m thick, open lateral and base boundaries, most likely porosity and permeability values). The white line indicates the outline of the CCC Prospect at spill point taken from the depth converted seismic. All the CO_2 is

Model	s01a	s01a5	s01b	s01b4	s01c	s01c2	s01d	s01e	s01f	s02a	s02a2	s02a3	s02a4	s03a	s04f	s07a
Permeability Minimum - Min Most likely - ML Maximum - Max	ML	ML	Min	Min	Max	Max	ML	ML	ML	ML	ML	Min	Max	ML	ML	ML
Porosity Minimum - Min Most likely - ML Maximum - Max	ML	Max	Min	ML	Max	ML	ML	ML	ML	ML	ML	ML	ML	ML	ML	ML
Thickness 320 m 120 m	320 m	320 m	320 m	320 m	320 m	320 m	320 m	320 m	320 m	320 m	320 m	320 m	320 m	320 m	120 m	320 m
Layers No Yes	No	No	No	No	No	No	No	No	No	Yes	Yes	Yes	Yes	No	No	Yes
Base Boundary Open Closed	Open	Open	Open	Open	Open	Open	Closed	Open	Closed	Closed	Open	Open	Open	Open	Closed	Open
Lateral boundaries Open Closed	Open	Open	Open	Open	Open	Open	Open	Closed	Closed	Closed	Open	Open	Open	Open	Closed	Open
Topography Yes No	Yes	Yes	Yes	Yes	Yes	Yes	Yes	Yes	Yes	Yes	Yes	Yes	Yes	No	Yes	No
Max. Pressure Increase* 20 yrs. (MPa)	1.50	1.52	1.62	1.68	1.36	1.36	2.92	1.50	5.34	3.76	0.68	1.97	0.58	1.49	13.53	0.64
Max. Pressure Increase* 120 yrs. (MPa)	0.25	-	0.29	0.26	0.23	-	0.26	0.25	3.17	-	-	-	-	0.19	7.76	-
Plume diameter†20 yrs. (km)	1740	1195	2345	1351	1345	1842	1934	1740	1745	1351	2145	0	2872	1740	2682	1448
Plume diameter†120 yrs. (km)	3266	-	4559	2872	2782	-	3392	3266	3198	-	-	-	-	3393	3571	-

Table 4.2: Summary of model configurations and results. *Pressure measured at top of reservoir along cross section line. †Plume diameter measured at top of reservoir along cross section line

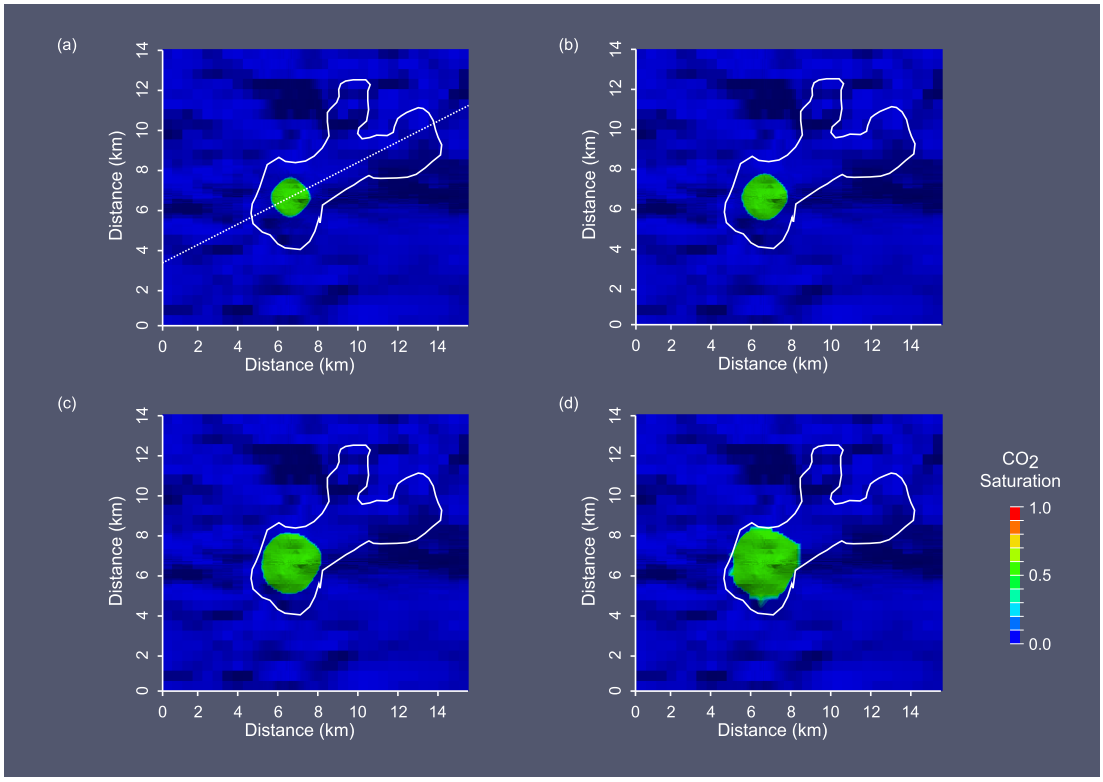

Figure 4.4: s01a - CO_2 saturation at the top of the storage site, (a) 20 years, (b) 30 years, (c) 70 years, (d) 120 years. Shading indicates surface topography. White line indicates outline of CCC Prospect. White dashed line indicates location of cross-section in later figures.

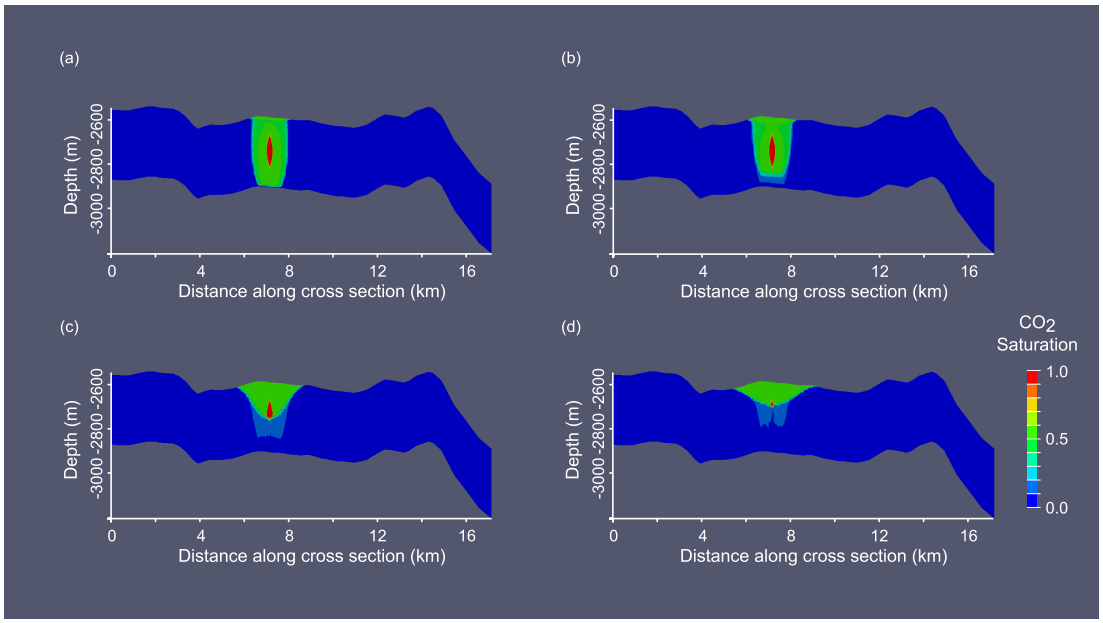

Figure 4.5: s01a - CO_2 saturation for a cross section through the storage site, (a) 20 years, (b) 30 years, (c) 70 years, (d) 120 years. 10 x vertical exaggeration. Cross section location shown in Fig. 4.4.

contained within the structure up to 100 years after the end of injection. However, the CO_2 plume is close to the edge of the structure at the end of the simulation and in time may migrate out of it.

A cross section through the plume (Fig. 4.5) shows that CO_2 concentration is highest around the injection point. At the end of 20 years of injection CO_2 fills the whole thickness of the storage site. After injection finishes the plume migrates upwards under buoyancy and spreads laterally beneath the caprock. The CO_2 does not appear to have stabilised by this time, which would be indicated by the base of the CO_2 saturated part of the reservoir being level. It is most likely that the CO_2 will migrate into the dip closure to the right of the injection point (at $\approx$ 14 km along the cross section) following the path with the highest stratigraphic relief.

Fig. 4.6 shows the pressure through time next to the injection point and at the top of the storage site, directly above the injection point. Injection rate is also shown. At both locations the pressure increases as the cumulative amount of injected CO_2 increases. Near the injection point pressure peaks at 40.1 MPa after 4 years and then decreases. At the top of the storage site pressure increases more slowly and reaches a peak of 35.5 MPa at around 10 years. Pressure in all locations never exceeds the caprock fracture pressure of 47 MPa.

The initial pressure peak during the injection period is probably related to modelling effects associated with a rapid increase in pressure when the injection begins (see Mathias *et al.*

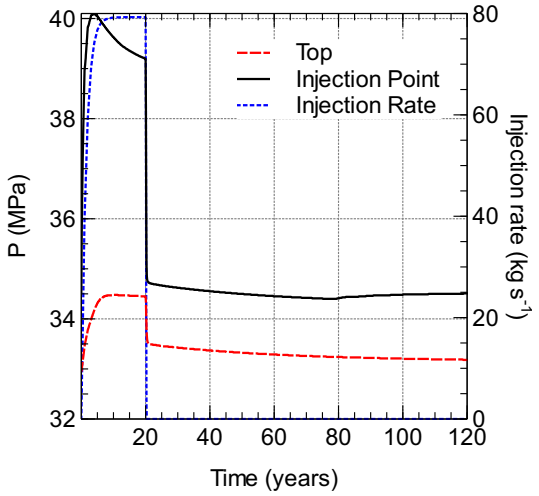

Figure 4.6: s01a (see Table 4.2) - Pressure (ΔP) through time for location immediately to the east of the injection point and at the top of the storage site above the injection point. Injection rate is also shown.

(2011)). It can be reduced by further shaping of the injection rate or a reduction in grid resolution around the injection point. Detailed modelling of injection has not been attempted in this study therefore maximum pressures for subsequent models have been taken at the end of the injection period where this effect is reduced.

The pressure increase at the top of the storage site, along the line of the cross section, can be seen in Fig. 4.7 (a). At the end of injection (20 years) the highest pressure increase is 1.50 MPa above virgin pressure, located above the injection point. Fig. 4.7 (b) shows the extent of the CO_2 plume at the top of the storage site. It can be seen that the pressure increase extends approximately 3 km on either side of the CO_2 plume. In the rest of the model pressure has returned to its starting value. After 120 years the pressure increase is 0.28 MPa. The highest pressure increase corresponds to the location of a structural stratigraphic high in the model where the CO_2 column beneath the caprock is thickest. The pressure increase does not extend further than the edge of the CO_2 plume at the end of the simulation.

4.5.2 Sensitivities

Boundary conditions

As the boundary conditions of the sides and the base of the model are not well constrained, several models have been run to test the sensitivity of results to a change in boundary conditions.

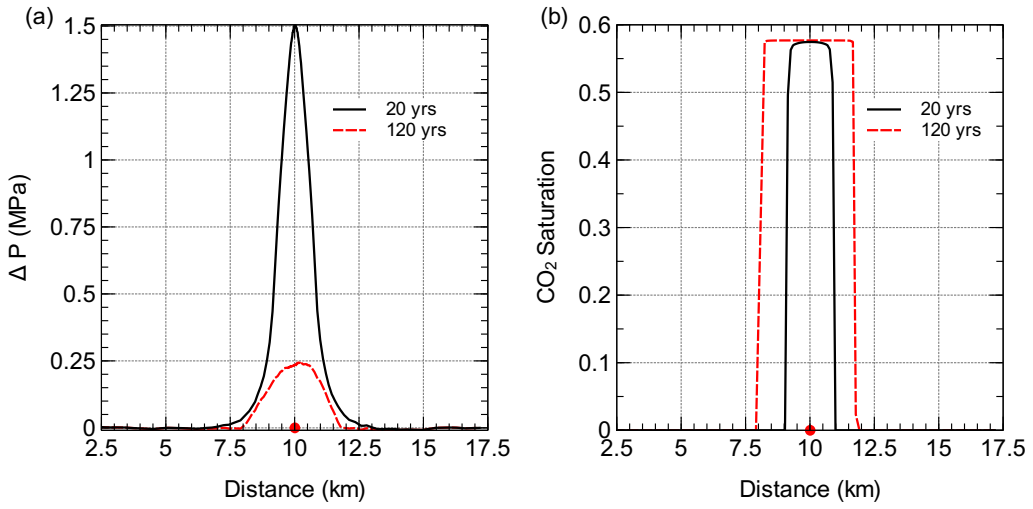

Figure 4.7: s01a (see Table 4.2) - (a) Pressure buildup (ΔP) and (b) CO_2 saturation, along cross section at the top of the storage site. Injection point indicated by the red circle. Cross section location shown in Fig. 4.4.

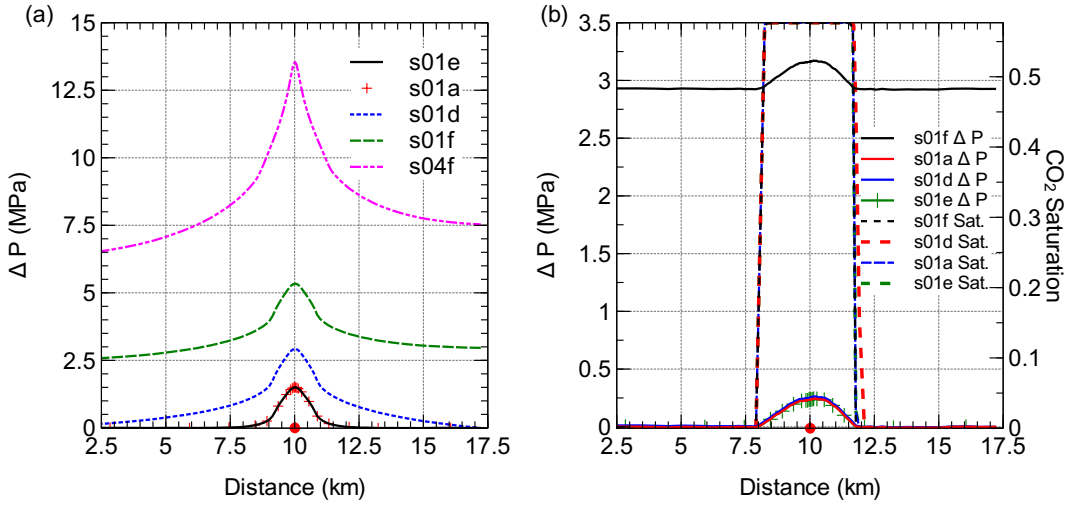

Figure 4.8: (a) Pressure buildup (ΔP) along cross section at the top of the storage site for models with different boundary conditions at 20 years. Injection point indicated by the red circle. (b) Pressure buildup and CO_2 saturation (Sat.) along cross section at the top of the storage site, for models with different boundary conditions, at 120 years. s01a - open base, open sides, s01d - closed base, open sides, s01e - open base, closed sides, s01f - closed base, closed sides, s04f - closed base, closed sides, thin storage site (see Table 4.2). Injection point indicated by the red circle. Cross section location shown in Fig. 4.4.

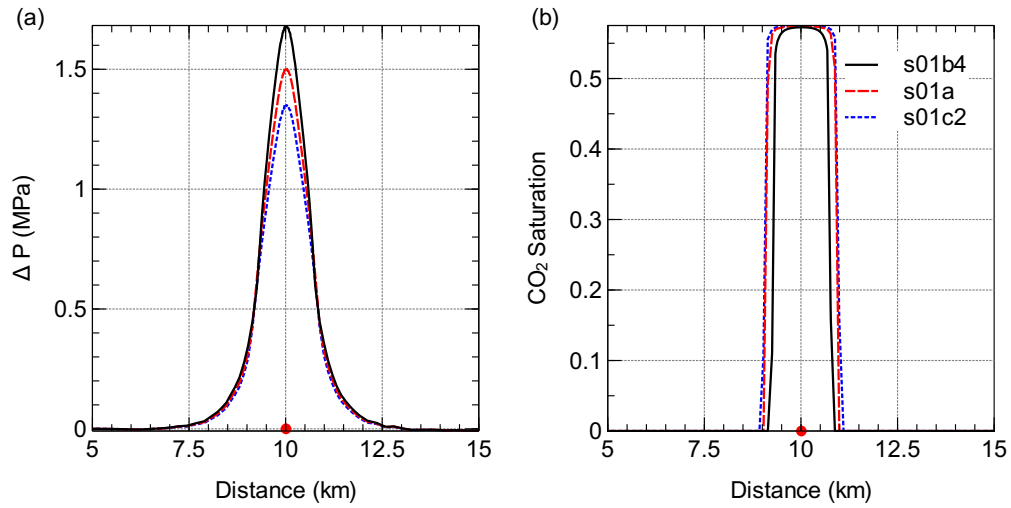

Figure 4.9: (a) Pressure buildup (ΔP) and (b) CO_2 saturation, along cross section at the top of the storage site, for models with different permeability, at 20 years. s01a - Most likely permeability, s01b4 Min. permeability, s01c2 - Max. permeability (see Table 4.2). Injection point indicated by the red circle. Cross section location shown in Fig. 4.4.

The pressure buildup at the end of injection is smallest for models with open (constant pressure) base boundaries (Fig. 4.8 (a)). For the two models run with open base boundaries the pressure increase is almost identical at 20 years, regardless of the nature of the lateral boundaries. Having closed boundaries on all sides of the model leads to a higher pressure buildup with a maximum pressure increase of 5.34 MPa above the injection point.

The thickness of the storage site is unknown. Therefore a worst case scenario model was developed with a relatively thin storage site (120 m) and closed boundaries on all sides. Pressure buildup in this model is much higher than in other models (Fig. 4.8 (a)). The pressure reaches a value of 46.5 MPa at the end of injection, which is very close to the estimated caprock fracture pressure of 47 MPa. The peak in pressure is located above the injection point.

After 120 years the pressure has returned to starting pressure everywhere except beneath the CO_2 plume, for models with at least one open boundary (Fig. 4.8 (b)). The pressure profile is the same for all models but pressures in the model with closed side and base boundaries are approximately 2.9 MPa higher than pressures in the other models. The plume diameter at 120 years is very similar in all models.

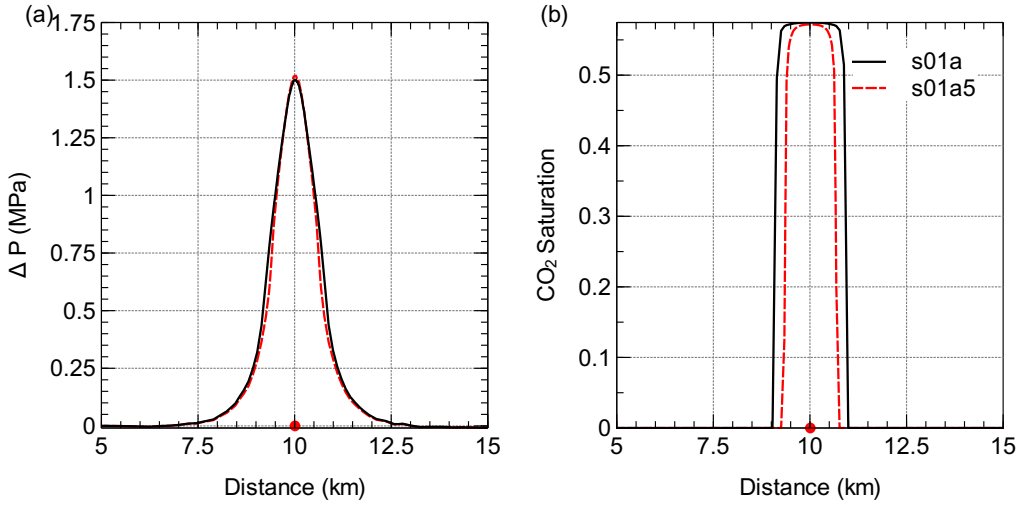

Figure 4.10: (a) Pressure buildup (ΔP) and (b) CO_2 saturation, along cross section at the top of the storage site, for models with different porosity, at 20 years. s01a - Most likely porosity, s01a5 - Max. porosity. Location of injection point indicated by the red circle. Cross section location shown in Fig. 4.4.

Facies	Thickness of layer (%)	Porosity (%)			Permeability (mD)		
		Min	Max	Mean	Min	Max	Mean
1. Fluvial	35	9	19	14	1	100	50.5
2. Aeolian	35	12	25	22	80	1000	540
3. Interdune	25	5	19	15	0.8	10	5.4
4. D facies	5	2	10	6	0.1	1	0.55

Table 4.3: Layer thicknesses and properties

Permeability / porosity

Models were run with minimum and maximum permeability and porosity values in addition to the most likely values used in the base case. Lowering the permeability results in an increase in pressure buildup and a decrease in plume diameters after 20 years (Fig. 4.9). Increasing porosity values leads to a small increase in maximum pressure buildup. Having a higher porosity reduces the plume diameter at the top of the model after 20 years (Fig. 4.10).

The pressure buildup and plume diameters which occur when both the porosity and permeability are changed at the same time show an increase in pressure buildup and plume diameter when the permeability and porosity are lower (Fig. 4.11).

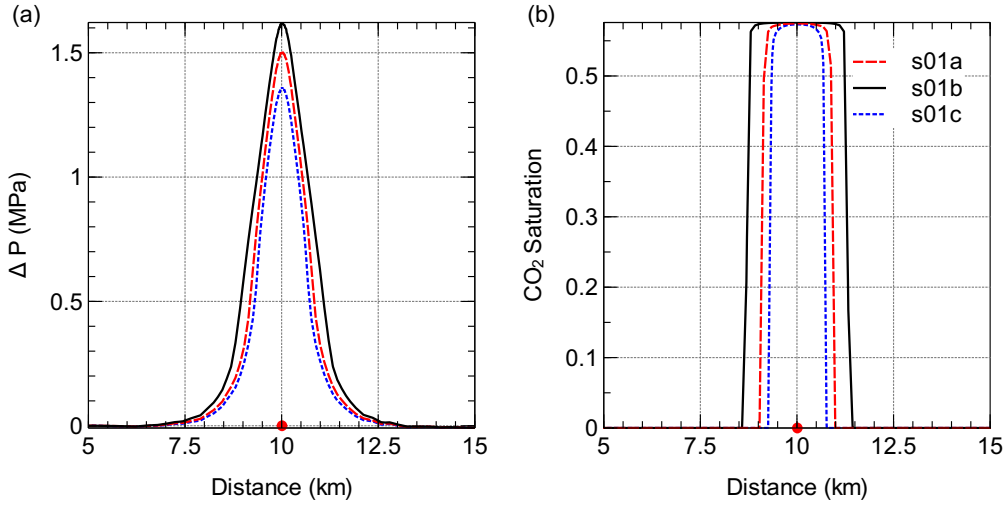

Figure 4.11: (a) Pressure buildup (ΔP) and (b) CO_2 saturation, along cross section at the top of the storage site, for models with varying porosity and permeability, at 20 years. s01a - Most likely porosity / permeability, s01b4 Min. porosity / permeability, s01c2 - Max. porosity / permeability (see Table 4.2). Location of injection point indicated by the red circle. Cross section location shown in Fig. 4.4.

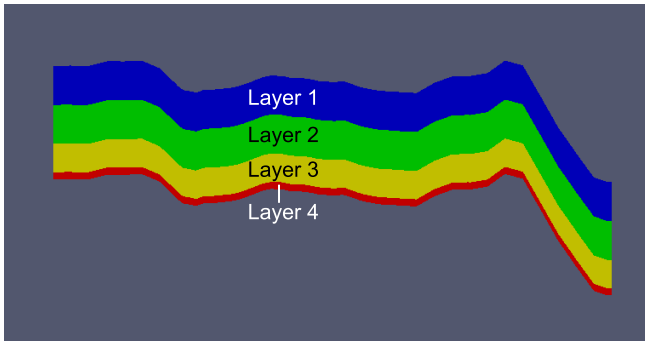

Figure 4.12: Slice through model showing layering. Numbers correspond to layers in Table 4.3. 10 x vertical exaggeration. Cross section location shown in Fig. 4.4.

Layering

Internal facies variation has been observed in Rotliegend reservoirs in the Auk and Argyll fields (Heward, 1992; Heward *et al.*, 2003). These variations have distinct permeability and porosity values which will affect fluid flow in the reservoir. A general layering scheme consisting of four layers has been derived from these papers, to represent possible layering in the Rotliegend at the location under investigation (Table 4.3). The thicknesses of layers have been defined as percentages to account for uncertainties in the total Rotliegend thickness.

Fig. 4.12 shows a cross section of the layered model. The presence of layers in the model modifies the shape of the CO_2 plume as it rises towards the top of the storage site. The CO_2

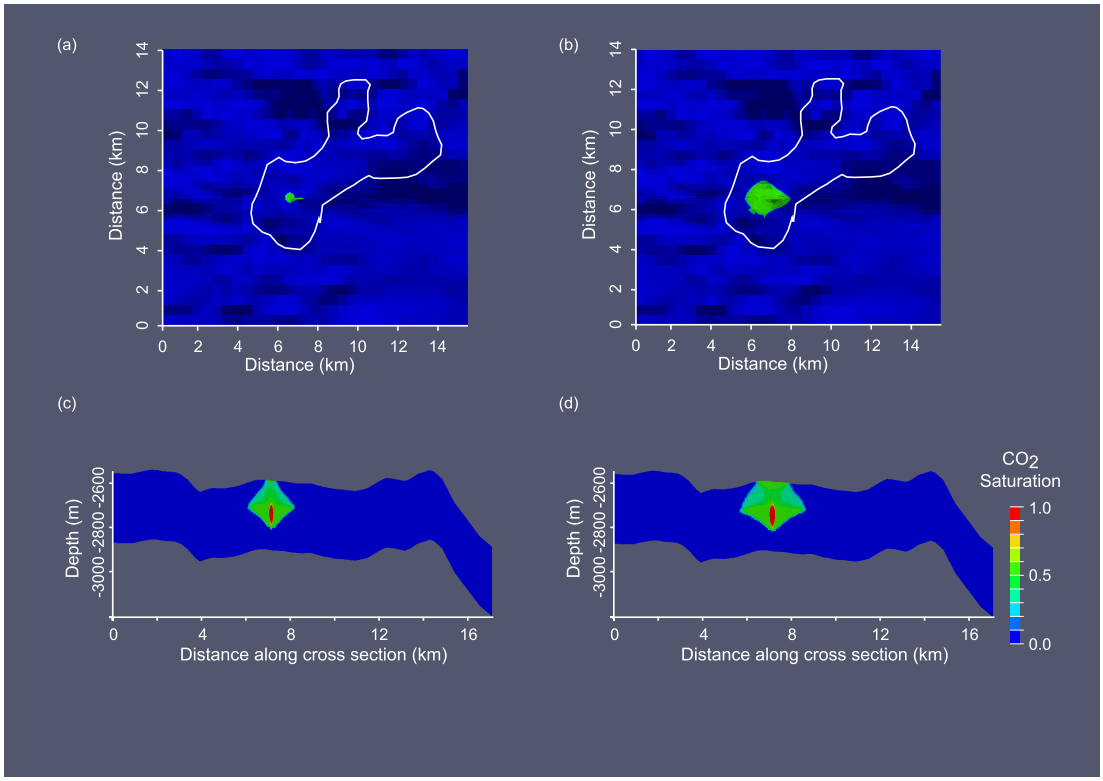

Figure 4.13: s02a - CO_2 saturation at the top of the storage site, for the layered storage site model, (a) 10 years, (b) 20 yrs. White line indicates outline of CCC prospect. CO_2 saturation for a cross section through the layered storage site model (c) 10 years, (d) 20 yrs. 10 x vertical exaggeration. Cross section location shown in Fig. 4.4.

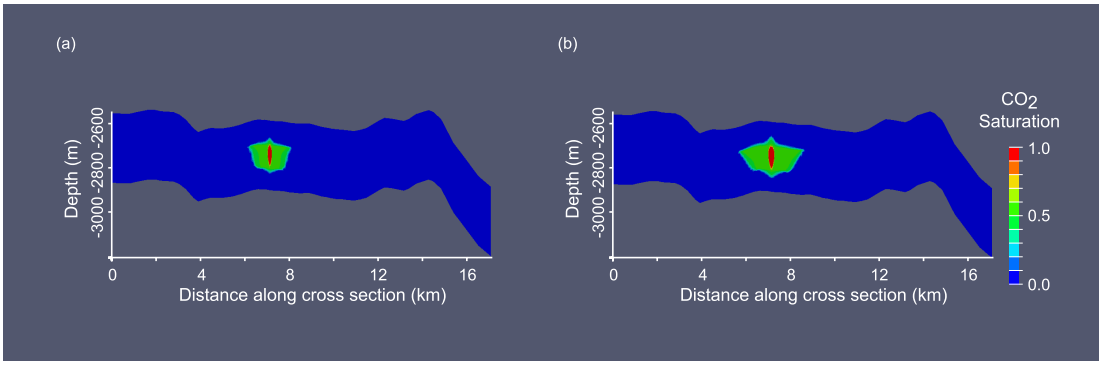

Figure 4.14: s02a3 - CO_2 saturation for a cross section through the layered storage site model, with low permeability, (a) 10 years and (b) 20 yrs. 10 x vertical exaggeration. Cross section location shown in Fig. 4.4.

spreads laterally beneath the boundary between layers 1 and 2 (Fig. 4.13 (c) & (d)). This reduces the amount of CO_2 reaching the top of the storage site compared to the homogeneous model and therefore reduces the plume diameter at the top of the model (Fig. 4.13 (a) & (b)). It can also be seen in Fig. 4.13 that the CO_2 plume footprint is more irregular in shape than in other models. The plume spreads further to the east of the injection point, following an area of high relief.

Permeability in the layered model has a large effect on the plume footprint and the pressure buildup. When the permeability is higher the plume footprint is much larger than in the model with average permeability. In the low permeability model the CO_2 does not reach the top of the model after 20 years of injection. Nearly all the CO_2 is still contained within layer 2 (Fig. 4.14). The layers reduce pressure buildup because they compartmentalise free CO_2; the exception being in the case of the low permeability layered model, where the maximum pressure increase after 20 years injection is nearly 2 MPa.

Stratigraphic Relief

To assess the impact of irregular stratigraphic relief on results, two additional models were built with flat, uniform surfaces, one with layers and one without.

Comparison of the non-layered models, both with and without irregular surfaces, shows that the effect of irregular stratigraphy on pressure buildup and plume spread is small (Fig. 4.15).

By contrast, in the layered models irregular stratigraphy has a noticeable effect on the pressure buildup and plume spread. In the flat, layered model the plume footprint and corresponding pressure buildup is symmetrical around the injection point. In the layered model with irregular stratigraphy the higher pressure buildup is observed in the region to the east of

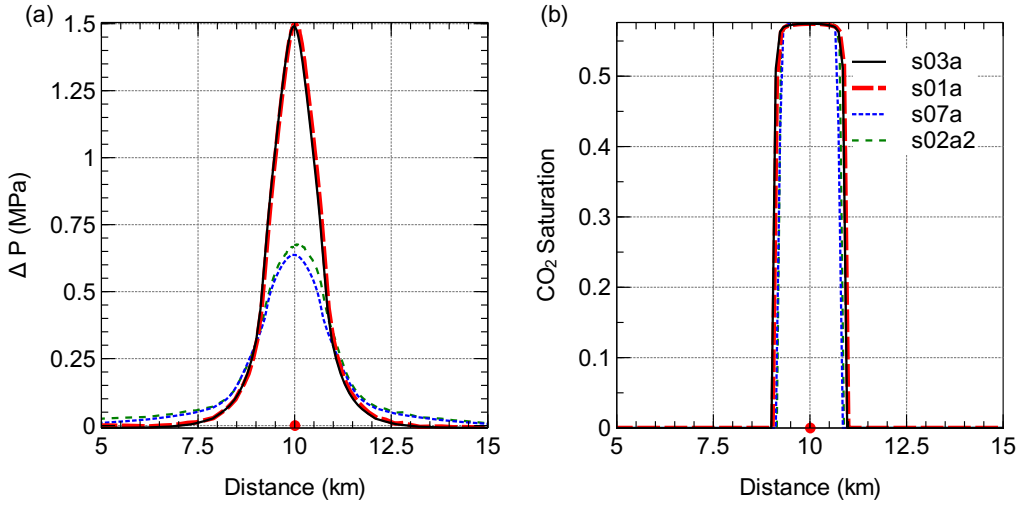

Figure 4.15: (a) Pressure buildup (ΔP) and (b) CO_2 saturation, along cross section at the top of the storage site, for flat and layered models, at 20 years. s03a - Flat, no layers, s01a - Irregular topography, no layers, s07a - Flat, layers, s02a2 - Irregular topography, layers (see Table 4.2). Location of injection point indicated by the red circle. Cross section location shown in Fig. 4.4.

the injection point related to the irregular plume footprint shown in Fig. 4.13.

4.6 Discussion

4.6.1 Pressure Buildup and Plume Diameter

The largest pressure increases are observed in the models with closed boundaries on all sides. This is because the pressure buildup in the storage site is unable to dissipate (see Mathias *et al.* (2011)). However, only in the thin, closed boundary model (s04f) is the pressure close to fracture pressure. Similar results have been found in other studies such as Hovorka *et al.* (2004) where the models with closed boundaries experienced the greatest pressure buildup. This situation, of a storage site with closed boundaries on all sides, is likely to be unrealistic for storage in a saline aquifer. Further data collection from the site should investigate how thick the storage site is, as well as ascertaining the nature of the base boundary of the storage site as these two factors appear to have the greatest influence on pressure buildup at this site.

The thickness of the Rotliegend at the CCC prospect could be better estimated if a well were drilled which completely penetrated the Rotliegend in the vicinity of the CCC prospect and reached the unit beneath. The collection of 3D seismic data which could be tied to this well

would allow a much better estimate of the reservoir geometry. Hence, confidence in estimates of pressure buildup and plume migration modelled using this data would be increased.

Increasing the permeability of the storage formation independently of porosity of the storage formation reduces the pressure buildup seen at the top of the model (s01a, s01b4, s01c2). This finding is similar to the results of Chadwick *et al.* (2009b) who showed that near-field pressure (within a 2.5 m radius of the injection well) is inversely proportional to permeability. Increasing storage formation porosity independently of permeability leads to slightly higher pressure at the top of the model (s01a, s01a5). When both porosity and permeability are varied together, the models with higher porosity and permeability exhibit lower pressure buildup (s01a, s01b, s01c).

Reducing the porosity of the storage site substantially increases the plume diameter at the top of the storage site, with the largest plume diameter observed for the model with the lowest porosity. This is because the same amount of CO_2 has to spread out further in a low porosity formation in order to find enough pore space to be accommodated. Increasing the permeability of the storage site without changing the porosity results in the plume diameter increasing. This result is supported by the findings of Han *et al.* (2010) who showed that a larger area of the storage site is swept by CO_2 when the formation permeability is increased. Similarly Jahangiri & Zhang (2011) found that the overall plume spread in all directions is increased when formation permeability is higher. Han *et al.* (2010) also showed an increase in movement of CO_2 through the reservoir for lower permeability ratio (k_v/k_h) which is likely to be the case for this reservoir although the permeability ratio has been kept constant in our simulations.

Decreasing porosity and permeability together results in a larger plume diameter in our models at the end of the simulation. For sandstones there is generally a strong positive correlation between porosity and permeability and therefore porosity and permeability should be varied together. The minimum permeability used in our models is higher than the permeability you would expect for a reservoir with the corresponding minimum porosity (Glennie, 1998). If the permeability was lower it is likely that the plume diameter would be decreased and the pressure buildup increased. It will be necessary then to have a better constraint on the relationship between porosity and permeability in the reservoir in order to better predict the plume diameter.

The porosity and permeability values used in the most likely case are much closer to the values of porosity and corresponding permeability that you would expect for Rotliegend Sandstone. The plume diameter for the most likely case is within the CCC Prospect at the end of

120 years. However, it is close to the edge of the CCC prospect and would probably migrate past the spill point after 120 years. The two main ways to stop this happening would be to fill the CCC prospect more effectively and to increase dissolution and residual trapping within the reservoir. The CCC prospect could be more effectively filled if the CO_2 were injected using multiple wells or a horizontal well which could spread the CO_2 out over the whole area of the trap.

Ideally the porosity and permeability relationship in the reservoir could be investigated by collecting and analysing well logs and core data at the site. Correlation of similar facies across multiple locations throughout the site would allow a much more thorough understanding of the spatial distribution of differing porosities and permeabilities. Subsequent modelling using the data would provide a more detailed estimate of potential CO_2 migration. However, the nature of dynamic modelling is such that if very detailed data were known it would still have to be upscaled somehow and used to populate grid cells of approximately 10 m x 10 m. In consequence of this, whilst as much porosity and permeability data as possible would be very useful, data on larger scales, such as seismic data, with one or two well ties, would allow deduction of porosity and permeability through the reservoir. This would be more immediately applicable to building a dynamic model than a highly detailed small scale model of reservoir porosity and permeability. Additionally, aside from any issues relating to cost, it would be undesirable to have lots of wells drilled and core taken from the site as this would increase the number of leakage pathways for CO_2 to escape to the surface.

Dissolution has not been modelled in this study but it would reduce the amount of free CO_2 within the plume and would therefore prevent the plume from spreading out so far (Gasda *et al.*, 2011). Some people have proposed ways of engineering the injection method to increase dissolution trapping. For example Qi *et al.* (2009) who suggested that injecting CO_2 with brine and then injecting brine alone could increase residual trapping. The result of this would then be an increase in dissolution trapping as the residually trapped CO_2 would dissolve in the brine surrounding it.

Further modelling of the entire site up to and including the stratigraphic trap, would be useful to determine the amount of CO_2 reaching the stratigraphic trap, and the time it would take to get there if it leaks out of the CCC Prospect.

Looking at the effect of internal stratigraphic layering shows that pressure buildup at the top of the model is reduced in the layered models. This is due to some CO_2 moving laterally beneath the boundary between layers 1 and 2 away from the injection point. The resulting

maximum pressure buildup is reduced, as the CO_2 column above the injection point is thinned (Fig. 4.15). However, the pressure increase affects a larger section of the reservoir because of the increased spread of CO_2 (Fig. 4.13). Core data from the site would give a much clearer indication of the layering present beneath the CCC Prospect. Subsequent modelling using this information would provide a better estimation of CO_2 migration at the site.

The effect of having a model with planar stratigraphy versus a model with irregular stratigraphy is only apparent when comparing the layered models (s02a2, s07a). Here the influence of increased stratigraphic relief leads to a more irregular plume shape with the plume extending further to the east than in the flat layered model (Fig. 4.13 (b)). A corresponding asymmetrical pressure profile can be seen at the top of the model (Fig. 4.15 (a)).

The irregular plume shape can be attributed to the movement of the CO_2 plume through the reservoir from the injection point to the top of the storage site. After 10 years of injection, a small amount of CO_2 has reached the top of the storage site above the injection point but some CO_2 has spread along the layer boundary and pooled at an area of high stratigraphic relief, before rising to the surface. The plume at top of the storage site has subsequently developed in an area slightly to the east of the injection point, where there is a rise in the reservoir-caprock boundary, creating a more irregular plume. Irregular plume shape, related to spreading of CO_2 along internal layering, has been observed in modelling studies by Ghomian *et al.* (2008). It has also been inferred from seismic data at Sleipner, where it can be seen that injected CO_2 is spreading beneath intraformational shale layers, following areas of high relief of the stratigraphic boundaries (Arts *et al.*, 2004).

In the homogeneous models and the flat layered model this has not happened as there is either no internal layering, or the layering is regular and contains no areas of high relief. This means that the CO_2 plume is still fairly regular in shape when it reaches the top of the storage site, leading to a correspondingly regular plume footprint.

4.6.2 Storage capacity

The simulations indicate that the site is likely to have a large enough storage capacity to accommodate injection of CO_2 at a rate of 2.5 Mt a^{-1} for 20 years. This leads to a total storage capacity of at least 50 Mt within the CCC Prospect. To put this into perspective, as of 2011, 12.7 Mt of CO_2 had been stored in the North Sea at Sleipner over 15 years (Statoil, 2011). 50 Mt is between 0.01 and 0.025 % of the total amount of CO_2 required to be stored by

the UK before 2050.

Pressure buildup in the case of the thin storage site with the closed boundary is very close to fracture pressure. If the storage site is thin with a closed boundary, it may be possible to prevent pressures reaching such high values by engineering the injection scheme in some way. For instance by injecting at a lower rate from multiple wells or by using a horizontal well which allows the CO_2 to be spread more evenly throughout the CCC Prospect. A large proportion of the CCC Prospect, to the north east, has not been filled. Further modelling should look at different injection schemes to determine the best way of filling the structure to maximise storage capacity and minimise pressure buildup.

4.6.3 Comparison of results with static capacity estimates

Hedley *et al.* (2013) used Monte-Carlo simulations to estimate static capacity at the site. Simulations were run for differing values of porosity, gross rock volume (volume of the CCC prospect), residual water saturation, maximum allowable pressure increase and efficiency factor. The efficiency factor is a factor related to the proportion of the reservoir which is likely to be swept by invading CO_2.

For each set of simulated variables the theoretical, open and closed capacities were estimated. The theoretical storage capacity is the pore volume of the reservoir, minus the residual water saturation, multiplied by density of CO_2 at the appropriate pressure and temperature conditions. The open storage capacity is the theoretical storage capacity multiplied by the efficiency factor. The closed storage capacity is the pore volume created by compressing the existing brine and rock within the reservoir up to the maximum allowable pressure buildup.

Statistics calculated from the results show that 80% of theoretical capacity estimates are in the range 42 Mt - 112 Mt. For open storage capacity estimates the range of results reduces to 7.59 Mt - 28 Mt. For closed storage capacity estimates 80% of the results were in the range 1.7 Mt - 3 Mt.

In comparison, dynamic modelling results indicate that for all models a storage capacity of 50 Mt can be achieved without exceeding fracture pressure. Albeit coming very close to fracture pressure for the closed thin system.

One reason for the large discrepancy between dynamic and static capacity estimates is that the static estimates only involve the volume of the CCC prospect down to the depth of the spill point. In the dynamic simulations there is CO_2 within the reservoir below the depth of

the spill point. Once this has migrated above the spill point it is possible that the CO_2 will flow laterally past the spill point and leak from the CCC prospect (after the 120 years which have been modelled), thereby reducing the modelled storage capacity. However, a large volume of the CCC prospect to the north east has not been filled and it is most likely that CO_2 will migrate up dip to the north east and fill the rest of the CCC prospect before moving down dip past the spill point.

The presence of accessible rock volume below the spill point will also have an effect on the capacity estimates for a closed aquifer. For capacity estimates relating to closed aquifers the only available pore space which can contain CO_2 is the additional pore space created by the compression of the brine and rock within the CCC prospect. This essentially assumes an impermeable layer directly below the CCC prospect at the level of the spill point. As the reservoir is likely to extend below the spill point the compressibility of the brine and rock below the CCC prospect must also be taken into account, increasing the extra pore space available to store CO_2.

Static capacity estimates for an open aquifer include a factor related to the sweep efficiency of the aquifer. Sweep efficiency can be reduced by small scale permeability variations within the reservoir which lead to preferential flow of CO_2 through areas with higher permeability. Sweep efficiency can also be reduced by larger scale permeability variations in the reservoir related to the net to gross ratio of the reservoir rocks. Additionally, sweep efficiency can be related to the geometry of the stratigraphic layers and the tendency of the buoyant CO_2 to flow up dip when it reaches a layer of lower permeability. This may cause channelling of the CO_2 along areas of high relief (e.g. Arts *et al.*, 2004).

The dynamic simulations do not include small scale permeability variations due to heterogeneities in the sandstones or values of net to gross. Therefore they are likely to overestimate sweep efficiency in the reservoir.

Static capacity estimates provide a way to quickly model many variations in reservoir parameters. However, there is a large discrepancy between the storage capacities predicted by the static models and those predicted by the dynamic models. This is primarily due to the fairly restrictive assumptions involved in the static capacity estimates. For instance the assumption of brine compressibility only within the trap in the case of a closed system is likely to be unrealistic in this case as we know the reservoir extends below the CCC prospect. Additionally the sweep efficiency factors used to estimate the open capacity of the trap are difficult to quantify without carrying out some form of dynamic modelling as well.

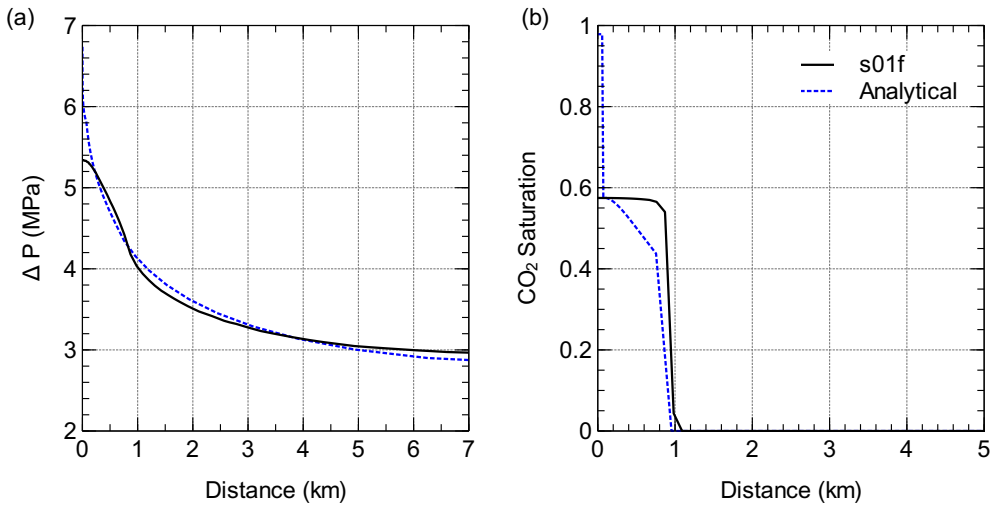

Figure 4.16: Comparison of results of dynamic modelling from this study with the analytical solution of Mathias *et al.* (2011). Reservoir is 320 m thick, injection well is at 0 km (a) Change in pressure. (b) CO_2 saturation.

4.6.4 Comparison of results with analytical solutions for plume diameter and pressure buildup

Mathias *et al.* (2011) derived an analytical solution for calculating plume diameter and pressure buildup assuming vertical equilibrium. The analytical solution assumes that the side and base boundaries of the reservoir are impermeable.

Figs. 4.16 and 4.17 show the comparison of the analytical solution with the corresponding dynamic solution for a reservoir thickness of 320 m and 120 m respectively. For both cases the pressure buildup predicted by the analytical model is slightly higher directly above the injection point. The plume diameters predicted by both models are very similar in both cases. The analytical model also predicts a value for CO_2 saturation around the injection point which is higher than one minus the residual water saturation. This is because the analytical solution models the dryout front, behind which the residual water has all dissolved into the CO_2 stream. The dynamic models also display this behaviour around the injection point but not at the surface where the results in Figs. 4.16 and 4.17 are taken from.

It can be seen that the analytical solutions provide very similar results to the dynamic models in certain situations. However, the main limitation is the fact that the analytical solutions can only be used to model one conceptual system i.e. where the storage site is surrounded by impermeable boundaries and where there is no internal heterogeneity.

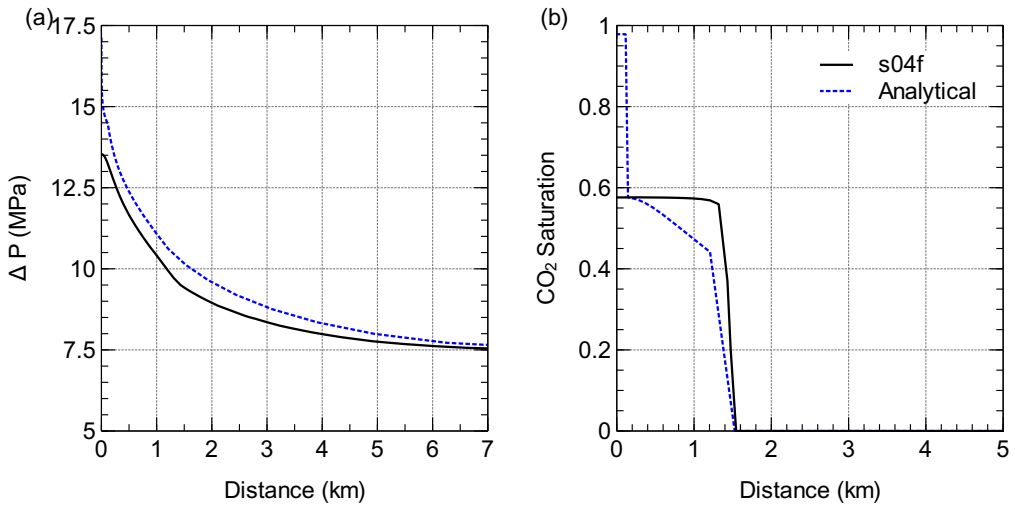

Figure 4.17: Comparison of results of dynamic modelling from this study with the analytical solution of Mathias *et al.* (2011). Reservoir is 320 m thick, injection well is at 0 km (a) Change in pressure. (b) CO_2 saturation.

4.6.5 Choice of dynamic modelling method

Using a full 3D numerical model has allowed us to produce results for storage capacity, pressure buildup and plume migration which include both the effects of vertical heterogeneity within the storage site and the geometry of the storage site. Using other dynamic modelling methods (e.g. streamline, vertical equilibrium etc.) would also give us indications of storage capacity, pressure buildup and plume migration. However, the large pressure change due to injection was considered unsuitable to be dealt with using streamline simulations. Additionally, the need to account for vertical layering and permeability anisotropy rendered vertical equilibrium modelling inappropriate. We have found that the combined presence of internal stratigraphic layering and stratigraphic relief has a noticeable impact on plume migration. Although we are not able to confidently predict plume migration at this stage, due to uncertainties in the input data, our modelling work indicates that the presence and properties of any stratigraphic layers in the storage site and the relief of potential layers are major influences on plume migration at the site. This supports the findings of several other case studies (e.g. Arts *et al.*, 2004; Hovorka *et al.*, 2004; Zhou *et al.*, 2010). Therefore when entering the next stage of the project, more data should be collected regarding internal porosity and permeability variations within the reservoir and the stratigraphic relief of the site to facilitate more accurate modelling of CO_2 migration.

4.7 Conclusions

In this study we have created a preliminary dynamic model of a potential CO_2 storage site, within a deep saline formation, of the Rotliegend sandstones of the UK North Sea. Model properties have been derived from a limited set of primary data from the site, and from literature and well log data from nearby locations.

Our modelling results indicate that the site can store approximately 2.5 Mt a^{-1} of CO_2 over a period of 20 years without injected CO_2 reaching the containment spill point or the pressure exceeding the caprock fracture pressure, for up to 100 years after injection. A large section of the CCC structure has not been filled

The main controls on pressure buildup are the nature of the base boundary of the storage reservoir and the thickness of reservoir at the storage site. The main controls on plume diameter are the porosity, permeability and permeability anisotropy ratio of the formation.

The major uncertainties at the site are the properties of the unit beneath the Rotliegend at the location of the CCC Prospect and the thickness of the Rotliegend at the CCC Prospect. Further data collection, such as the acquisition of a 3D seismic data set, tied to well data within the storage site, would assist in improving our understanding of these two parameters.

A thorough understanding of the porosity and permeability structure within the storage site would allow a much better estimate of plume migration pathways and plume diameter. To facilitate this more well and core data should be collected in the vicinity of the storage site. A compromise needs to be made between maximising the number of wells which can be drilled at the site and minimising the man-made leakage pathways for CO_2. Furthermore, it should be noted that for the purpose of dynamic modelling, data regarding small scale porosity and permeability variations (i.e. < 10 m resolution) will have to be scaled up and aggregated using a methodology similar to that described in this work, in order to populate a dynamic model. As a consequence, the acquisition of a high resolution seismic dataset in conjunction with a small number of well and core datasets would be more useful for building a dynamic model, than, for instance, collecting lots of core data without finding out any more information regarding the geometry and boundaries of the storage site.

Overall, the site looks promising for CO_2 storage and warrants some further investigation. Modelling using more detailed information will improve estimates for plume migration and pressure buildup. These models can then be used to test ways of filling the structure more efficiently, for instance with different injection locations, numbers of wells, and injection rates,

in order to maximise CO_2 storage capacity and minimise pressure buildup within the CCC Prospect.

A comparison between static and dynamic modelling of the site for CO_2 sequestration shows that generally the dynamic capacity estimates exceed the static capacity estimates. This mainly due to the assumptions required to calculate static capacity estimates which are not necessarily true and are not required for the dynamic modelling. Analytical estimates of pressure buildup and plume diameter are very quick to calculate, and provide a close match with dynamic models for scenarios with closed boundaries. However they are not suitable for modelling other situations such as a reservoir with open boundaries or internal heterogeneity.

3D, grid based, numerical modelling has been useful as it has allowed us to identify and prioritise factors which could have a strong influence on the behaviour of CO_2 at the site even though only limited site data is available. This information will dictate the planning of future site characterisation work.

The authors would like to thank Progressive Energy Ltd. and TGS-NOPEC for access to seismic data. The authors would also like thank David Noy for his assistance with TOUGH2.

Chapter 5

Dissolution of CO_2 from leaking fractures in saline formations

Summary

In this chapter we use a 2D, finite difference, MATLAB model to simulate dissolution rates from a vertical fracture, with CO_2 flowing through it, in a secondary storage formation. The objectives were:

1. To build a MATLAB code capable of modelling CO_2 dissolution in brine and subsequent convection at conditions found in a potential storage site.
2. To investigate the impact of leaky fractures, in and around a storage site, on CO_2 dissolution rates.

The model is a single-phase, multi-component flow model. The decision to build a model in MATLAB instead of using TOUGH2 was made to enable us to model a simplified situation and concentrate solely on the small scale dissolution processes occurring, without the influence of any multiphase effects.

A version of this chapter is published in the following article:

Watson, F. E., Mathias, S. A., van Hunen, J., Daniels, S. E., & Jones, R. R. (2012). Dissolution of CO_2 from leaking fractures in saline formations. *Transport in Porous Media*, 94(3), 729-745.

The MATLAB model used was built by myself with assistance from Simon Mathias and Jeroen van Hunen. All simulations were run and analysed by myself. Write up of the work was carried out by myself with reference to discussions on the significance of the results provided by all the authors.

5.1 Introduction

High permeability fractures in and around a storage formation can provide pathways to transport CO_2 towards the surface (Pruess, 2008; Annunziatellis *et al.*, 2008) and as such are generally seen in a negative light when assessing storage security. However, flow along fractures increases the CO_2 - brine interface which can lead to enhanced dissolution rates and increased storage of CO_2 in overlying porous units. In this study we consider dissolution rates of CO_2 from a vertical fracture in a porous medium. The increase in dissolution rates caused by diffusion and subsequent convection of the aqueous CO_2 is investigated.

Dissolution from areas of high concentration to low concentration occurs initially by molecular diffusion and is proportional to the concentration gradient. Dissolution can be further enhanced by the onset of convection (Farajzadeh *et al.*, 2007), as convective motion causes an influx of fresh material towards the boundary layer, increasing the concentration gradient at the boundary.

Convection occurs when diffusion causes a gravitationally unstable situation with relatively high density material overlying lower density material. Convection begins once the diffusive boundary layer of high density material reaches a critical thickness which depends on the properties of the porous medium and the convecting fluid. The occurrence of convection is related to the porous media Rayleigh number, Ra (Horton & Rogers, 1945), which is a dimensionless parameter measuring the stability of a system (see also Eq. (5.9)). It is the ratio of factors which encourage convection to factors which suppress convection. The Rayleigh number can be increased by increasing the permeability and height of the system and the density difference between the convecting fluids. Increasing the fluid viscosity, the porosity of the porous medium and the rate at which diffusion takes place, which is controlled by the apparent diffusion coefficient, will reduce the Rayleigh number.

Analytical solutions in the context of CO_2 dissolving into brine show that the onset time for convection is shorter when the system has a higher Rayleigh number (Ennis-King *et al.*, 2005; Riaz *et al.*, 2006; Xu *et al.*, 2006). The critical thickness of the diffusive boundary layer

required to initiate convection is given by Riaz *et al.* (2006) and is inversely proportional to the Rayleigh number. A consequence of this critical thickness is that convection may not occur in very thin formations with low Rayleigh numbers.

Convection enhanced dissolution of CO_2 into brine has been studied experimentally (Farajzadeh *et al.*, 2007; Kneafsey & Pruess, 2010). Power law relationships have been derived between the Rayleigh number of a system and the increase in convection in that system (Hassanzadeh *et al.*, 2007; Neufeld *et al.*, 2010). The power law exponents in the different studies vary due to differences in the assumptions made when modelling convection. In a CO_2 storage case similar to that at Sleipner in the North Sea, Neufeld *et al.* (2010) estimate that convective dissolution alone could account for dissolution of around 10% of the annual amount of injected CO_2. Clearly then, convection of aqueous CO_2 is an important factor to be considered when planning for CO_2 storage.

Numerical studies show that the presence of high permeability fractures in a storage site can increase dissolution rates (Carneiro, 2009; Iding & Blunt, 2011). This is caused by preferential flow of CO_2 through the fractures leading to an increase in the surface area between CO_2 and brine and consequently an increase in the area from which dissolution can occur.

Iding & Blunt (2011) found from numerical modelling that the relative increase in amount of dissolution in a system is reduced as more fractures are added to the system. The interaction between multiple fractures and their impact on dissolution and convection is something which requires further consideration.

Chang *et al.* (2009) proposed that the amount of CO_2 reaching the surface after leaking through a high permeability fracture can be reduced if the fracture passes through suitably permeable formations on its way to the surface. They defined a leakoff coefficient based on Darcy's law to quantify the lateral leakage from a fault into surrounding permeable formations. Their modelling showed that the amount of CO_2 reaching the surface after leaking from the storage formation is lower when the fracture intersects more layers with high permeability, although this increases the total amount leaking out of the storage formation. Hence leakage into secondary formations may be useful for reducing the risk of CO_2 escape at the surface.

This study seeks to investigate dissolution rates of CO_2 from a fracture to provide a better understanding of processes which can affect CO_2 once it has leaked from the storage formation. Dissolution rates can be compared to the rate of flow through the fracture to see if dissolution from fractures is significant enough to mitigate against potential leakage of CO_2 into unsafe areas (e.g. potable aquifers) or to the surface. The impact of model Rayleigh number on

convection patterns and therefore dissolution rates is assessed.

The work builds on previous studies of flow of CO_2 through fractures (Carneiro, 2009; Iding & Blunt, 2011) by looking explicitly at convection enhanced dissolution in relation to fracture flow.

5.2 Methodology

5.2.1 Conceptual model

Our conceptual model consists of a single fracture within a permeable formation. It is assumed that the fracture has a relatively high permeability allowing supercritical CO_2 to flow through it. CO_2 is also able to escape laterally from the sides of the fracture via diffusion. The fracture begins in the storage formation and intersects the caprock and a secondary permeable formation above the caprock (Fig. 5.1). The permeability of the caprock is too low to allow significant convection currents to occur within it but convection may develop independently within the secondary formation. Our model represents the secondary permeable formation containing a fracture with supercritical CO_2 constantly flowing through it.

Experimental modelling (Chalbaud *et al.*, 2009) suggests that when a non-wetting fluid (i.e. CO_2) displaces a wetting fluid (i.e. brine), the non-wetting fluid tends to flow through the larger pore space. However, a thin layer of wetting fluid remains along the pore walls and traps the non-wetting fluid in the pore space. This may be the case for CO_2 flowing through an open or high-permeability fracture. If so, the layer of brine coating the inside of the fracture will quickly become saturated with dissolved CO_2. Diffusion of CO_2 will occur from the CO_2 saturated edge of the fracture into the surrounding formation waters.

Assuming that the full length of the fracture is initially saturated with supercritical CO_2 which can only escape laterally from the fracture by diffusion, the fracture can be modelled as a constant source of dissolved CO_2. Multiphase flow of supercritical CO_2 within a brine filled fracture has not been modelled. Making the assumption that CO_2 is already dissolved into the brine at the edge of the fracture reduces the complexity of the model by allowing us to model only a single aqueous phase.

5.2.2 Governing equations

The relevant governing equations for flow and transport are as follows:

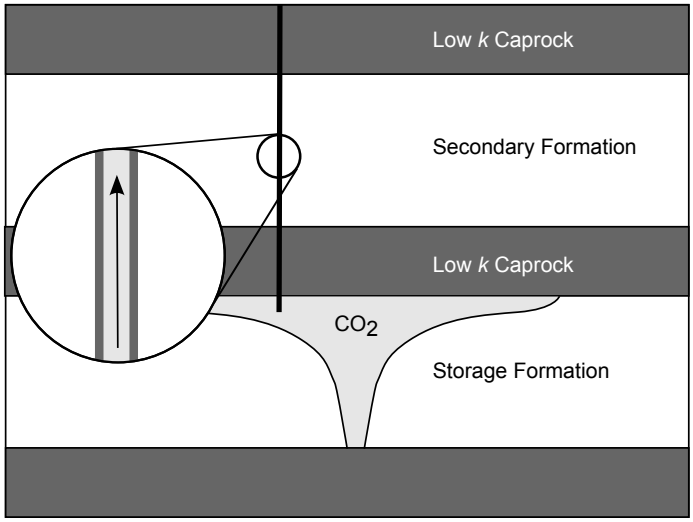

Figure 5.1: Conceptual model. White layers have high permeability and dark grey layers have low permeability. The arrow shows the direction of flow of supercritical CO_2 in the fracture, although in our model this is represented by a constant dissolved CO_2 concentration as opposed to free flowing CO_2

$$\phi(c_r + c_f)\frac{\partial P}{\partial t} = -\frac{\partial q_x}{\partial x} - \frac{\partial q_z}{\partial z} \tag{5.1}$$

$$\phi\frac{\partial C}{\partial t} = -\frac{\partial}{\partial x}\left(q_x C - \phi D_A \frac{\partial C}{\partial x}\right) - \frac{\partial}{\partial z}\left(q_z C - \phi D_A \frac{\partial C}{\partial z}\right) \tag{5.2}$$

where the volumetric fluid fluxes, q_x and q_z, are found from Darcy's Law expressions:

$$q_x = -\frac{k}{\mu}\left(\frac{\partial P}{\partial x}\right) \qquad q_z = -\frac{k}{\mu}\left(\frac{\partial P}{\partial z} + \rho g\right) \tag{5.3}$$

and ϕ is the porosity of the matrix, c_r is the rock compressibility, c_f is fluid compressibility, P is pressure, C is concentration, $\boldsymbol{D_A}$ is the apparent diffusion coefficient, k is the permeability of the medium, μ is the viscosity of the fluid, ρ is the fluid density, and g is gravity.

The following linear relationship between density, ρ, and solute concentration, C, is assumed:

$$\rho = \rho_0 + \Delta\rho\left(\frac{C - C_0}{C_1 - C_0}\right) \tag{5.4}$$

where ρ_0 is the brine density when $C = C_0$, $\Delta\rho$ is the density difference between brine with $C = C_1$ and brine with $C = C_0$, C_0 is the minimum concentration and C_1 is the maximum concentration.

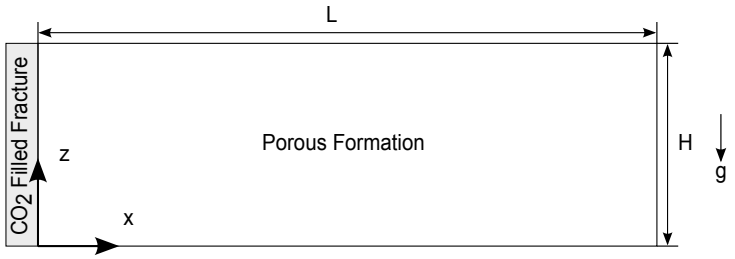

Figure 5.2: Schematic diagram of the model and the coordinate system (not to scale)

Following from the previous discussion associated with development of the conceptual model, the relevant initial and boundary conditions are (also see Fig. 5.2)):

$$\begin{aligned}
P = P_0 + \rho_0 g z, \quad & 0 < x < L, \quad && 0 < z < H, \quad && t = 0 \\
q_x = 0, \quad & x = 0, \quad && 0 < z < H, \quad && t > 0 \\
q_x = 0, \quad & x = L, \quad && 0 < z < H, \quad && t > 0 \\
q_z = 0, \quad & 0 < x < L, \quad && z = 0, \quad && t > 0 \\
q_z = 0, \quad & 0 < x < L, \quad && z = H, \quad && t > 0
\end{aligned} \tag{5.5}$$

$$\begin{aligned}
C = C_0, \quad & 0 < x < L, \quad && 0 < z < H, \quad && t = 0 \\
C = C_1, \quad & x = 0, \quad && 0 < z < H, \quad && t > 0 \\
\frac{\partial C}{\partial x} = 0, \quad & x = L, \quad && 0 < z < H, \quad && t > 0 \\
\frac{\partial C}{\partial z} = 0, \quad & 0 < x < L, \quad && z = 0, \quad && t > 0 \\
\frac{\partial C}{\partial z} = 0, \quad & 0 < x < L, \quad && z = H, \quad && t > 0
\end{aligned} \tag{5.6}$$

Introducing the dimensionless transformations

$$x_D = \frac{x}{H}, \qquad z_D = \frac{z}{H}, \qquad t_D = \frac{D_A t}{H^2} \tag{5.7}$$

$$C_D = \frac{C - C_0}{C_1 - C_0}, \qquad P_D = \frac{P + \rho_0 g z}{\Delta \rho g H} \tag{5.8}$$

$$Ra = \frac{k \Delta \rho g H}{\mu \phi D_A}, \qquad \epsilon = \frac{\Delta \rho g H (c_r + c_f)}{Ra} \tag{5.9}$$

reduces the above problem to:

$$\epsilon \frac{\partial P_D}{\partial t_D} = -\frac{\partial q_{xD}}{\partial x_D} - \frac{\partial q_{zD}}{\partial z_D} \tag{5.10}$$

$$\frac{\partial C_D}{\partial t_D} = -\frac{\partial}{\partial x_D}\left(q_{xD} Ra C_D - \frac{\partial C_D}{\partial x_D}\right) - \frac{\partial}{\partial z_D}\left(q_{zD} Ra C_D - \frac{\partial C_D}{\partial z_D}\right) \tag{5.11}$$

$$q_{xD} = -\frac{\partial P_D}{\partial x_D} \qquad q_{zD} = -\frac{\partial P_D}{\partial z_D} - C_D \tag{5.12}$$

$$\begin{aligned}
P_D &= \frac{P_0 + \rho_0 g z}{\Delta \rho g H}, & 0 < x_D < \frac{L}{H}, \quad & 0 < z_D < 1, & t_D = 0 \\
q_{xD} &= 0, & x_D = 0, \quad & 0 < z_D < 1, & t_D > 0 \\
q_{xD} &= 0, & x_D = \frac{L}{H}, \quad & 0 < z_D < 1, & t_D > 0 \\
q_{zD} &= 0, & 0 < x_D < \frac{L}{H}, \quad & z_D = 0, & t_D > 0 \\
q_{zD} &= 0, & 0 < x_D < \frac{L}{H}, \quad & z_D = 1, & t_D > 0
\end{aligned} \tag{5.13}$$

$$
\begin{aligned}
C_D &= 0, & 0 < x_D < \frac{L}{H}, \quad & 0 < z_D < 1, & t_D &= 0 \\
C_D &= 1, & x_D &= 0, & 0 < z_D < 1, \quad & t_D > 0 \\
\frac{\partial C_D}{\partial x_D} &= 0, & x_D &= \frac{L}{H}, & 0 < z_D < 1, \quad & t_D > 0 \\
\frac{\partial C_D}{\partial z_D} &= 0, & 0 < x_D < \frac{L}{H}, \quad & z_D &= 0, & t_D > 0 \\
\frac{\partial C_D}{\partial z_D} &= 0, & 0 < x_D < \frac{L}{H}, \quad & z_D &= 1, & t_D > 0
\end{aligned}
\tag{5.14}
$$

The above set of equations are solved by discretizing in space using finite differences (see Appendix B). The resulting set of coupled ordinary differential equations are then simultaneously integrated with respect to time using MATLAB's solver, ODE15s. The developed code was verified by comparison to the pseudospectral solution of the Elder problem presented by Van Reeuwijk *et al.* (2009).

The model domain is rectangular with a constant concentration boundary on the left hand side and no flow boundaries on all other sides. The no flow boundary opposite the constant concentration boundary is set far enough away from the concentration boundary ($L/H = 200$) to have a minimal effect on dissolution patterns. The model contains 40 x 50 grid elements. Horizontal grid resolution decreases logarithmically away from the concentration boundary over 6 orders of magnitude. Next to the concentration boundary $\Delta x_D \sim 10^{-5}$, at $x = L$, $\Delta x_D \sim 58$. Vertical grid resolution is kept constant at $\Delta z_D = 0.02$. Time-stepping is controlled by the default adaptive time-stepping scheme of ODE15s.

5.3 Results

Fig. 5.3 shows dimensionless CO_2 concentration through time for a model with Ra = 500. Initially CO_2 diffuses perpendicular to the fracture plane but as more CO_2 diffuses into the brine, convection occurs whereby gravity causes the dense, CO_2-rich brine to sink and spread out along the impermeable bottom surface of the model. At later times the convection becomes weaker relative to diffusion and the CO_2 concentration profile tends towards being perpendicular to the boundary.

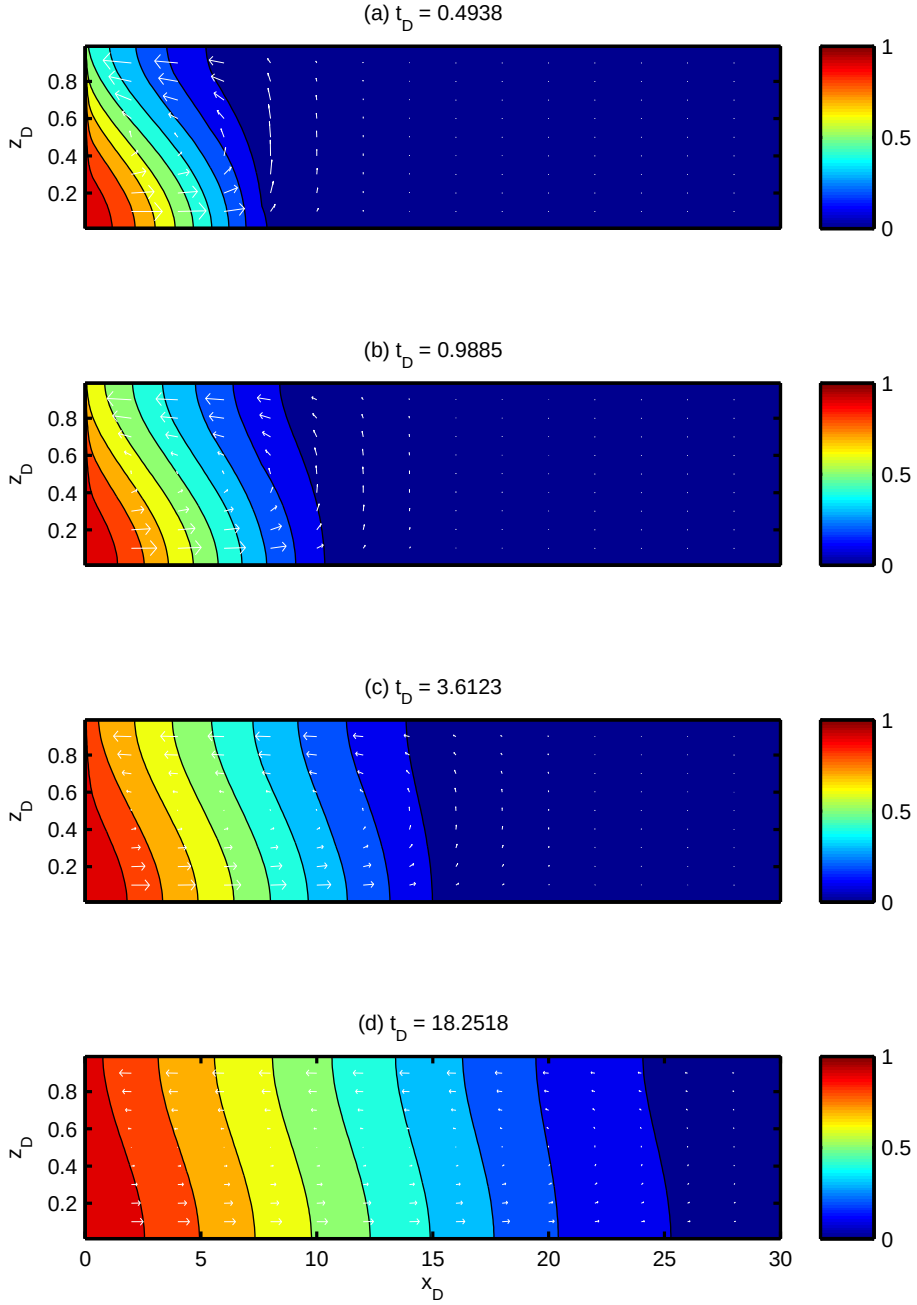

Figure 5.3: Dimensionless CO_2 concentration, C_D, for model with $Ra = 500$ at varying t_D. Contours are in the range 0 to 1 with increments of 0.1. White arrows indicate direction and relative magnitude of fluid flux vectors.

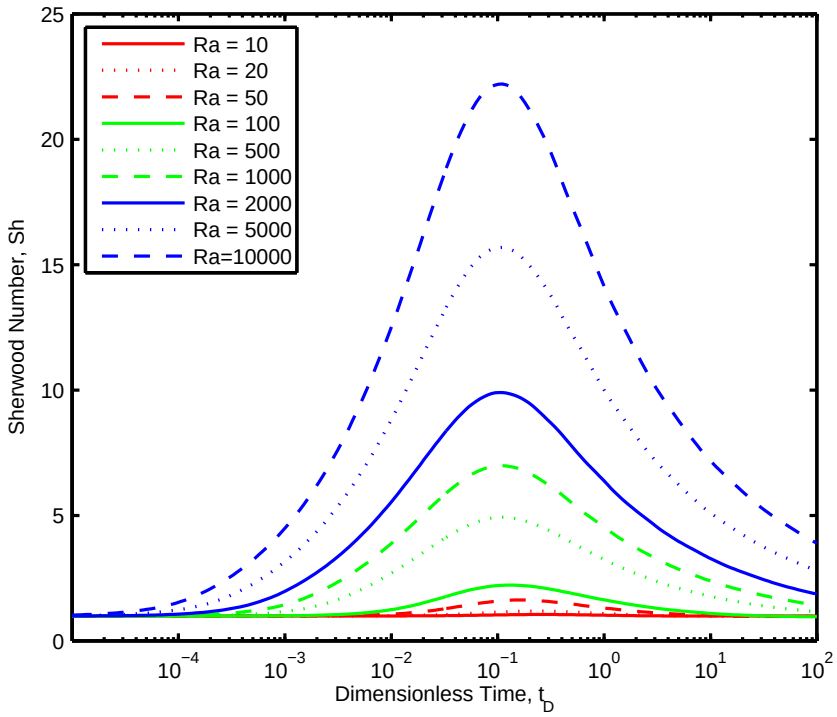

Figure 5.4: Sherwood number through time for models with varying Ra

5.3.1 Changing Rayleigh Number

A useful measure of the amount of convection in a system is the dimensionless Sherwood number, Sh. In this context, the Sherwood number is the ratio of the mass flux across the $x = 0$ boundary, for a given Ra, to the mass flux that would occur in the absence of convection (i.e., $Ra = 0$). In this way, $Sh = 1$ when mass transfer is occurring purely by diffusion. In the presence of convection, $Sh > 1$.

Mathematically, Sh can be obtained from:

$$Sh = \frac{F_{xD}(0, Ra)}{F_{xD}(0, 0)} \tag{5.15}$$

where

$$F_{xD}(x_D, Ra) = \int_0^1 q_{xD} Ra C_D - \frac{\partial C_D}{\partial x_D} dz_D \tag{5.16}$$

For the limiting case when $Ra = 0$, there is no convection, diffusion becomes one-dimensional and the problem can be solved analytically to get (Carslaw & Jaeger, 1959):

$$C(x,t) = (C_1 - C_0)\text{erfc}\left(\frac{x}{2\sqrt{D_A t}}\right) + C_0 \tag{5.17}$$

where erfc denotes the complementary error function.

Differentiating Eq. (5.17) with respect to x and integrating with respect to z (from 0 to H) leads to the equation for mass flux across the $x = 0$ boundary:

$$F_x(x=0) = -\phi\rho D_A H \left.\frac{\partial C}{\partial x}\right|_{x=0} = (C_1 - C_0)\phi\rho H\sqrt{\frac{D_A}{\pi t}} \tag{5.18}$$

Hence it can be said that the dimensionless diffusive mass flux, $F_{xD}(0,0)$, can be found from:

$$F_{xD}(0,0) = \frac{F_x(x=0)}{(C_1 - C_0)\rho\phi D_A} = -\left.\frac{\partial C_D}{\partial x_D}\right|_{x_D=0} = (\pi t_D)^{-1/2} \tag{5.19}$$

Fig. 5.4 shows the variation in Sherwood number for models with different Rayleigh numbers. The Sherwood number for all models peaks between $t_D = 0.1$ and $t_D = 1$ and is slightly earlier for higher Rayleigh numbers. The magnitude of the Sherwood number represents the amount of convective enhancement to dissolution, e.g. a Sherwood number of 10 indicates that the dissolution rate is ten times higher than it would be if only diffusion were occurring. The peak in Sherwood number represents the point in time where the most convective enhancement to dissolution is occurring. This happens just before the downwards movement of CO_2 saturated brine away from the diffusing interface is slowed down by the presence of the no flow boundary at the bottom of the model. Sherwood number is highest for higher Ra models where more convection occurs.

Fig. 5.5 shows the dimensionless flux across the left hand boundary of the model, $F_{xD}(0, Ra)$. Alongside, plotted as circular markers, is the equivalent response due to pure diffusion (i.e., $Ra = 0$). Higher Rayleigh number models exhibit higher mass transfer rates (and hence dissolution rates). Initially mass flux is diffusion dominated. As convection starts to affect dissolution rates the flux decreases at a slower rate. At later times convection slows down and the model results converge on those for pure diffusion once again.

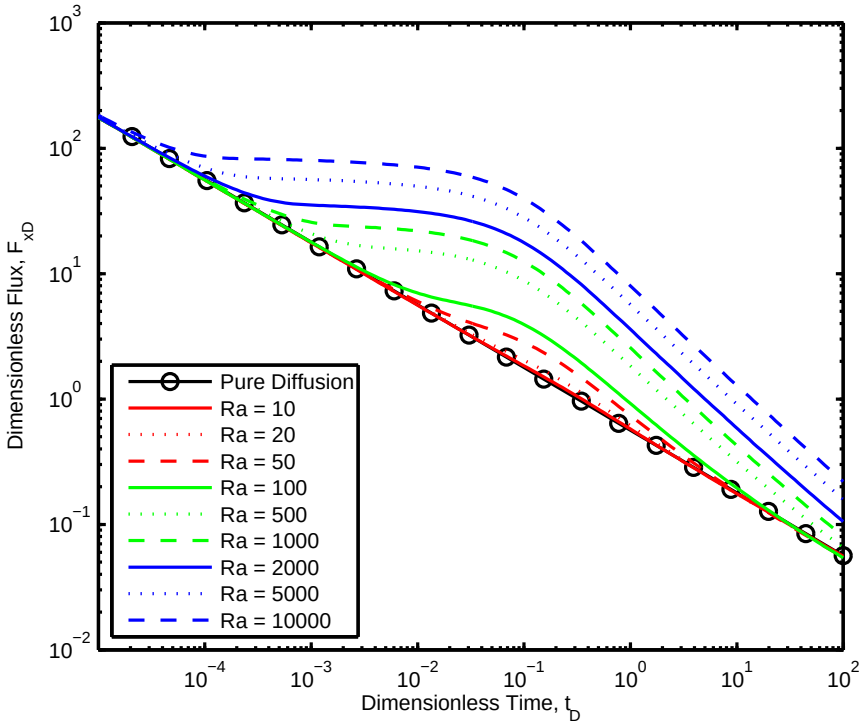

Figure 5.5: Dimensionless CO_2 flux from fracture for models with varying Ra

5.3.2 Comparison with flow through fracture

To assess the practical significance of lateral dissolution from a fracture it needs to be compared to possible flow rates of CO_2 through the fracture. Flow through an open fracture can be approximated as flow between two parallel plates. The volumetric flow rate per unit width between two vertical, parallel plates can be calculated using the following equation (Turcotte & Schubert, 2002):

$$Q_f = -\frac{b^3}{12\mu}\frac{\partial P}{\partial z} \tag{5.20}$$

where b is the fracture aperture and

$$\frac{\partial P}{\partial z} = -(\rho_b - \rho_{CO_2})g \tag{5.21}$$

The mass flux through the fracture, M_f, is:

$$M_f = Q_f \rho_{CO_2} = \frac{b^3}{12\mu}(\rho_b - \rho_{CO_2})g\rho_{CO_2} \tag{5.22}$$

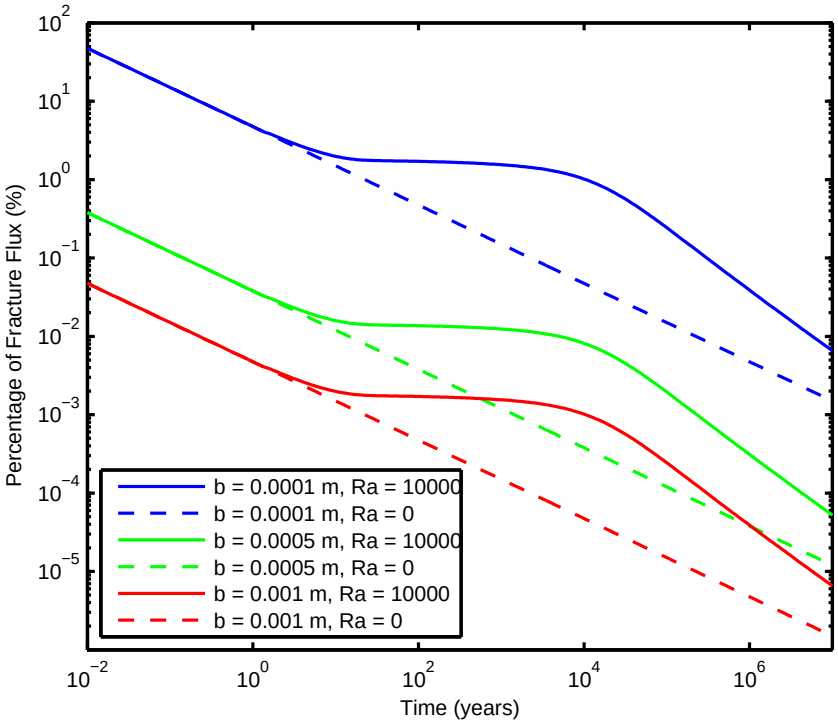

Figure 5.6: Mass transfer from fracture into rock matrix as percentage of flux through fracture for fracture length $H = 100$ m, other properties as described in Table 5.1 and varying aperture, b

Fig. 5.6 shows the mass transfer of CO_2 from the fracture into the rock matrix (as calculated using the model described in the previous section), for a realistic secondary formation thickness $H = 100$ m, as a percentage of the CO_2 flux through the fracture for different fracture apertures. Rayleigh number has been varied by changing the model permeability. Other properties used are shown in Table 5.1. Fluxes have been multiplied by $2H$ to account for dissolution from both sides of the fracture in a formation of thickness H.

For a fracture aperture of 0.1 mm the mass transfer at early times is around 50 % of the flux through the fracture. At later times the mass transfer is less than 1 % of the fracture flux. For an aperture of 1 mm the diffusive flux is always less than 1 % of the fracture flux. In all cases shown of 100 m thick formation, convection does not begin until after 1 year.

Fracture apertures estimated at the In Salah CO_2 storage site in Algeria are in the range of 0.5 to 1 mm (Iding & Ringrose, 2010). Assuming such a range and given a layer thickness of 100 m and a Rayleigh number of 500, the dissolution flux at 1 year is between 0.0380 % and 0.0047 % of the CO_2 flux through the fracture. These values are extremely small but are greatly influenced by the fracture aperture. For instance, the dissolution flux at 1 year for a fracture aperture of 0.1 mm, would be 4.75 % of the fracture flux under the same conditions.

Parameter	Symbol	Value	Units
Pressure	P	10	MPa
Temperature	T	45	°C
Apparent Diffusion Coefficient	D_A	2×10^{-9}	$m^2\ s^{-1}$
Formation Porosity	ϕ	0.3	-
Formation Permeability	k	1×10^{-14}	m^2
Brine Salinity	-	0.032	wt. %
Brine Viscosity at P, T and Salinity	μ_b	0.6330×10^{-3}	Pa s
Brine density at P, T and Salinity	ρ_b	1015.21	$kg\ m^{-3}$
CO_2 saturated brine density at P, T and Salinity	ρ_{sat}	1023.69	$kg\ m^{-3}$
CO_2 viscosity at P and T	μ_{CO_2}	0.3616×10^{-4}	Pa s
CO_2 density at P and T	ρ_{CO_2}	499.84	$kg\ m^{-3}$
Gravity	g	9.81	$m\ s^{-2}$

Table 5.1: Model Parameters

5.4 Discussion

Our results show that convection enhanced dissolution will occur when CO_2 dissolves from a vertical surface. The higher the Rayleigh number of the formation containing the diffusing surface, the higher the amount of convection and therefore the higher the dissolution rate from that surface. Dissolution rates decrease through time although this decrease can be slowed by the occurrence of convection. The amount of CO_2 diffusing out of a fracture is probably going to be small in comparison to the amount of CO_2 flowing through the fracture but depends on the fracture aperture and the Rayleigh number of the system.

Fig. 5.7 shows the convection enhanced CO_2 mass flux from a fracture inside a secondary formation. Fluid and rock properties assumed are described in Table 5.1. The plots show the fluxes at 1, 10, 100 and 1000 years. After 1 year, for thicker formations (H = 100 m to 500 m) the convection has not started, therefore the CO_2 flux is independent of permeability and is driven by pure diffusion. For H = 10 m convection starts earlier therefore CO_2 flux increases with formation permeability, (and hence the Rayleigh number). Despite this, CO_2 flux is higher in thicker formations due to the larger fracture surface area. At later times convection occurs for models with all values of H where permeability is high enough.

To gain insight into the basic physics of the system, several simplifying assumptions have been made. The model consists of a single fracture which is instantaneously filled with CO_2 and is situated within a homogeneous, porous layer. Flow rate within the fracture is considered constant and is purely due to the buoyancy of the CO_2. The system is at close to hydrostatic pressure.

It is assumed that pressure in the primary storage formation is low enough to prevent CO_2

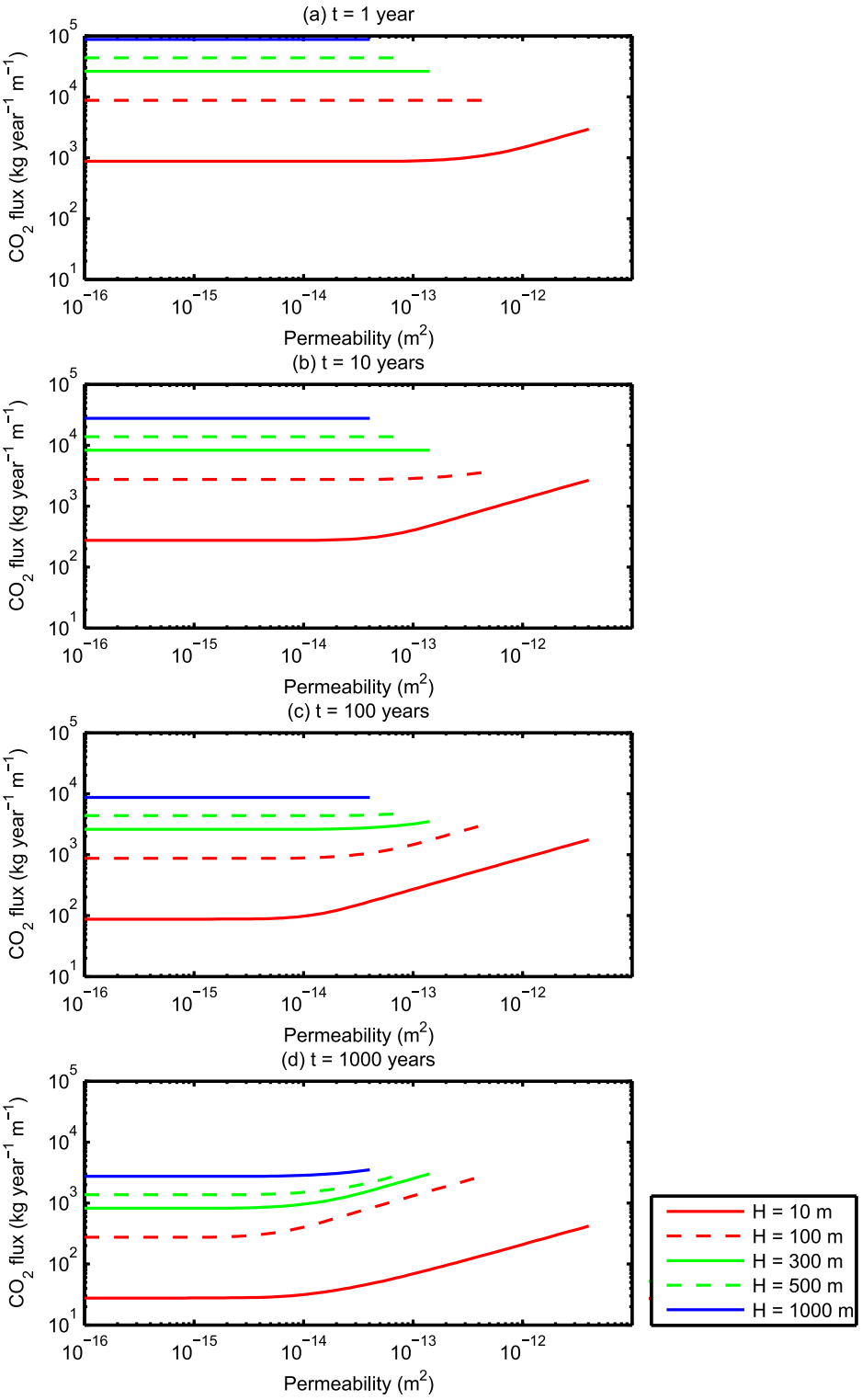

Figure 5.7: CO_2 dissolution rate from fracture for different k and H through time. All other properties as described in Table 5.1

from overcoming the capillary threshold pressure at the base of the seal. If this pressure were overcome, diffuse leakage of CO_2 into the base of the seal would occur, as opposed to leakage occurring only via fractures. Additionally, if the pressure within the fracture were higher than the capillary threshold pressure, the lateral movement of free CO_2 from the sides of the fracture, as studied by Chang *et al.* (2009), could take place. This has not been considered in our study. Dissolution rates would be enhanced if supercritical CO_2 was able to overcome capillary pressures and escape laterally from a fracture into a secondary formation rather than only escaping from the sides of the fracture by diffusion. This is because the surface area of a plume of CO_2 escaping from the fracture into a secondary formation would be larger than the surface area of a single fracture.

Heterogeneity in the system will have an effect on dissolution. Simulations have shown that increasing the heterogeneity of the permeability within a formation increases dissolution rates (Farajzadeh *et al.*, 2011). However, the presence of low permeability layers may restrict downward movement of the convecting aqueous CO_2, limiting convection in the system. Of interest is the effect on dissolution rates if a fracture passes through several discrete layers stacked on top of each other. Where low permeability barriers prevent transportation of CO_2 between layers via convection, dissolution rates from separate layers (with individual H and Ra) can be added together to obtain a bulk dissolution rate for the series of formations as a whole. Our model also assumes isotropic permeability. Introducing permeability anisotropy is also likely to affect dissolution rates by altering convection patterns.

The ability of the storage formation to provide the fracture with a constant source of CO_2 is assumed. This may not be the case if permeability within the storage formation is such that the CO_2 supply cannot be replenished at a rate similar to the flow rate through the fracture.

Our models do not consider what happens as the fracture initially fills up with CO_2. This process involves two phase displacement within the conduit whereby CO_2 displaces the brine originally in the fracture. This is a complex process which may lead to channelling of the CO_2 as it displaces the brine. Potentially, large regions of brine can be left inside the fracture even after CO_2 breakthrough at the top of the fracture. Dissolution rates from the sides of the fracture will be reduced compared to our model results if the brine at the edge of the fracture is not saturated with dissolved CO_2.

In the time before CO_2 fills the whole of the fracture, mass transfer rates will be lower than predicted in our model. However, our estimates of fracture flow in section 5.3.2 are also too high at early times as the relative permeability of CO_2 in a fracture containing CO_2 and brine

will be smaller than the CO_2 permeability when the fracture only contains CO_2. Therefore, the cubic law will initially overestimate the rate of flow of CO_2 through the fracture.

Fracture flow rates estimated using the cubic law are higher than those actually expected as they assume the fracture is bounded by planar surfaces. The presence of asperities on the fracture walls increases the tortuosity of the fluid flow path through the fracture (Zimmerman & Bodvarsson, 1996). This will reduce flow rates through the fracture and correspondingly the mass transfer from the sides of the fracture will be more significant.

Our results assume that the CO_2 remains in the supercritical phase throughout the whole length of the fracture. Supercritical CO_2 within the fracture could change phase into gaseous or liquid phase CO_2 if it rises and reaches an area with low enough pressure or temperature. This effect would have consequences for flow rates through the fracture.

It is possible that the permeability of a fracture could change with depth. In particular an area of reduced permeability within a fracture will reduce flow rates through the fracture (Chang *et al.*, 2009), allowing a larger proportion of the CO_2 to be dissolved. Fracture permeability can also change over time. For instance, in an overpressured formation a fracture may open due to the pressure of the CO_2 column beneath it and subsequently close again when the pressure dissipates after discharge of CO_2 through the fracture (Sibson, 1990). This so called 'fault-valve' behaviour would limit the amount of fluid in the fracture, possibly allowing all the CO_2 within the fracture to be dissolved away before it reaches the surface. Therefore, dissolution from fractures can potentially be a significant mechanism for mitigating against CO_2 leakage through low permeability or short lived, open fractures. However, this is not likely to apply in our model as the pressure is assumed to be close to hydrostatic.

The representation of a fracture as a single homogeneous conduit is fairly simplistic. In reality, fractures may be part of a larger fault zone containing a low permeability core surrounded by a potentially higher permeability damage zone (Caine *et al.*, 1996). In this case, fluid flow behaviour will be different to the parallel plate model considered here. In particular, if flow takes place in a network of interconnected, smaller fractures in the damage zone, dissolution patterns from individual fractures will interfere with each other. Interaction between multiple fractures has not been looked at in this study. Multiple fractures close together could increase dissolved CO_2 concentrations in the area surrounding each fracture. This will reduce concentration gradients around individual fractures and therefore reduce dissolution rates per fracture. The presence of multiple fractures would, however, increase overall amounts of CO_2 dissolution, although this increase is likely to be accompanied by an increase in the amount of

CO_2 leaking from the primary storage formation.

5.5 Conclusion

In this study we have used models to investigate convection enhanced dissolution from a vertical concentration boundary, representing a CO_2 filled fracture, into a homogeneous and isotropic porous medium, representing a secondary storage formation. Our modelling has shown that convection increases dissolution rates from the fracture and is proportional to the Rayleigh number of the formation into which the CO_2 is dissolving.

Dissolution rates decline through time as the concentration of CO_2 in the formation surrounding the fracture increases. The comparative dissolution rate from the sides of a fracture is likely to be very small compared the the total amount of CO_2 escaping through an open fracture but this is highly dependent on the fracture aperture. Variation of fracture permeability with time or depth may also reduce fracture flow rates of CO_2. In this case dissolution from the sides of the fracture will become more significant and could serve to prevent a leak to surface.

To facilitate insight into the physics of the system several assumptions have been made in our modelling. The fracture has been modelled as a single conduit; no heterogenity or anisotropy within the formation has been modelled; pressure within the model is taken to be close to hydrostatic; it is assumed that the fracture fills up instantaneously and the CO_2 source is constant; it is assumed that the CO_2 is only able to escape laterally from the fracture via diffusion.

Further investigation into fracture flow dynamics, the interaction of dissolution patterns from multiple fractures and the influence of heterogeneity within the system is required to increase our understanding of dissolution related to CO_2 flow through fractures. Work on these topics can be used to inform future CCS projects and improve estimates of dissolution rates for site characterisation.

Chapter 6

Mathematical model for two phase, two component, miscible flow

Summary

This chapter shows the development of the mathematical model for isothermal, two-phase, two-component, miscible flow in porous media used in Chapter 7. The model includes volume change on mixing which allows the density of components to change depending on which phase they are in. The assumption of equilibrium in the two phase region has been made. This means that the composition of fluid phases in the two phase region is always set to the equilibrium phase composition at the specified phase pressure and temperature. In reality a small amount of time is required before the composition reaches equilibrium but as this time is short, this is a helpful assumption to make.

The model is developed for isothermal conditions although temperature is set in the model in order to calculate the thermophysical properties of the fluids. Temperature variation in the model would require an extra differential equation for the change in temperature over time to be derived.

The two phases of interest are a supercritical phase predominantly containing CO_2 and an aqueous phase predominantly containing H_2O with dissolved NaCl. The equation of state

described in Chapter 3 is used to calculate properties for this combination of fluids.

6.1 Governing Equations

Governing equations for this problem are described in Section 2.2. Additionally we define a total mass of all components, F, and a corresponding mass balance:

$$F = \phi \sum_{i=1}^{Nc} G_i = \phi \sum_{j=1}^{Np} \rho_j S_j \tag{6.1}$$

$$\frac{\partial F}{\partial t} = -\nabla \cdot \sum_{j=1}^{Np} \rho_j \boldsymbol{q_j} \tag{6.2}$$

along with a term for the total mass fraction of component i, z_i:

$$z_i = \frac{G_i}{F} \tag{6.3}$$

The following mixing rule has been used to calculate phase density ρ_j:

$$\rho_j = \left(\sum_{i=1}^{Nc} \frac{X_{ij}}{\rho_{ij}} \right)^{-1} \tag{6.4}$$

where ρ_{ij} is the partial density of component i in phase j. Phase saturations, S_j, are fractions of the total volume of the pore space therefore:

$$\sum_{j=1}^{Np} S_j = 1 \tag{6.5}$$

The sum of the component mass fractions in each phase, X_{ij}, is given by:

$$\sum_{i=1}^{Nc} X_{ij} = 1 \tag{6.6}$$

6.2 Primary dependent variables

For the two-phase, two-component model $Np = 2$ and $Nc = 2$. The primary dependent variables chosen for this problem are the total pressure, P, and the mass fraction of component 1, z_1. For convention we define phase 1 as the gaseous phase and phase 2 as the aqueous phase. Component 1 is defined as CO_2 and component 2 as H_2O.

It is possible to deduce all other values, such as phase saturations and compositions, using just these two variables. This is due to the assumption of equilibrium, which is described further in Section 6.3.

Total pressure P is given by:

$$P = P_1 S_1 + P_2 S_2 \tag{6.7}$$

where P_1 and P_2 are individual phase pressures and are calculated using the capillary pressure, P_c (see Section 2.2.2):

$$P_c = P_1 - P_2 \tag{6.8}$$

Total pressure has been chosen as a primary dependent variable instead of one of the phase pressures as, unlike the phase pressures, total pressure is defined regardless of which phases are present.

z_1 has been chosen as a primary dependent variable instead of F or G_1 because both of these variables are dependent on pressure. We could equally well have chosen z_2 as a primary dependent variable. Indeed, $z_2 = 1 - z1$.

6.3 Defining phase conditions

In our model there are three possible phase conditions for $Np = Nc = 2$:

- A - Single phase conditions - only phase 1 present
- B - Two phase conditions - phases 1 and 2 present
- C - Single phase conditions - only phase 2 present

The presence of different phases is determined by the mass fraction of each component present, X_{ij}, and the component mass fractions at equilibrium, x_{ij}.

Equilibrium mass fractions tell us how a component is partitioned between each phase at equilibrium (see Section 3.4). If we have single phase conditions with only phase 1 present (condition A) then X_{11} must be greater than x_{11} and X_{21} must be less than x_{21} (if X_{21} was greater than x_{21} a separate aqueous phase (phase 2) would form). Similarly if we have single phase conditions with only phase 2 present X_{12} would be less than x_{12} and X_{22} would be greater than x_{22}.

The phase conditions can be distinguished using the value of z_1, the assumption of equilibrium compositions in the two-phase region and the knowledge that solubility of CO_2 in the aqueous phase is small, so $x_{12} < x_{11}$.

From Eq. (6.3):

$$\begin{aligned} z_1 &= \frac{\rho_1 S_1 X_{11}}{\rho_1 S_1} = X_{11} && S_1 = 1, && S_2 = 0 \\ z_1 &= \frac{\rho_1 S_1 x_{11} + \rho_2 S_2 x_{12}}{\rho_1 S_1 + \rho_2 S_2} && 0 < S_1 < 1, && 0 < S_2 < 1 \\ z_1 &= \frac{\rho_2 S_2 X_{12}}{\rho_2 S_2} = X_{12} && S_1 = 0, && S_2 = 1 \end{aligned} \tag{6.9}$$

Consequently it can be understood that phase conditions can be defined as follows:

- $z_1 \geq x_{11}$ - A Single Phase 1
- $x_{11} < z_1 < x_{12}$ - B Two Phase
- $z_1 \leq x_{12}$ - C Single Phase 2

Once we have ascertained which phases are present we can deduce phase saturations, component mass fractions and phase densities.

6.4 Derivation of time derivatives

6.4.1 Expression for the variation of z_1 with time

The total derivative of z_1 is given by:

$$dz_1 = \frac{1}{F}\left(dG_1 - z_1 dF\right) \tag{6.10}$$

It follows that the partial derivative of z_1 with respect to t is:

$$\boxed{\frac{\partial z_1}{\partial t} = \frac{1}{F}\left(\frac{\partial G_1}{\partial t} - z_1\frac{\partial F}{\partial t}\right)} \tag{6.11}$$

where $\frac{\partial G_1}{\partial t}$ and $\frac{\partial F}{\partial t}$ are defined above (Eqs. (2.1) and (6.2)).

6.4.2 Expression for the variation of P with time

Given that $F = F(z_1, P)$, the total derivative of F is:

$$dF = \left(\frac{\partial F}{\partial z_1}\right)_P dz_1 + \left(\frac{\partial F}{\partial P}\right)_{z_1} dP \tag{6.12}$$

the partial derivative of F with respect to t is:

$$\frac{\partial F}{\partial t} = \left(\frac{\partial F}{\partial z_1}\right)_P \frac{\partial z_1}{\partial t} + \left(\frac{\partial F}{\partial P}\right)_{z_1} \frac{\partial P}{\partial t} \tag{6.13}$$

which can be rearranged to give the partial derivative of P with respect to t:

$$\boxed{\frac{\partial P}{\partial t} = \left[\frac{\partial F}{\partial t} - \left(\frac{\partial F}{\partial z_1}\right)_P \frac{\partial z_1}{\partial t}\right]\left(\frac{\partial F}{\partial P}\right)_{z_1}^{-1}} \tag{6.14}$$

To find $\frac{\partial P}{\partial t}$ we need expressions for $\left(\frac{\partial F}{\partial z_1}\right)_P$ and $\left(\frac{\partial F}{\partial P}\right)_{z_1}$.

Total derivative of F

Expanding the right hand side of Eq. (6.1) and finding the total derivative of F gives:

$$dF = F\frac{d\phi}{\phi} + \phi\sum_{j=1}^{Np}\left[\rho_j S_j\left(\frac{d\rho_j}{\rho_j} + \frac{dS_j}{S_j}\right)\right] \tag{6.15}$$

To find $\frac{d\rho_j}{\rho_j}$ let:

$$u_{ij} = \frac{X_{ij}}{\rho_{ij}}, \qquad\qquad u_j = \sum_{i=1}^{Nc} u_{ij} \tag{6.16}$$

then Eq. (6.4) becomes

$$\rho_j = \frac{1}{u_j} \tag{6.17}$$

The total derivatives of du_j and du_{ij} are:

$$du_j = -\frac{d\rho_j}{\rho_j^2} = \sum_{i=1}^{Nc} du_{ij} \tag{6.18}$$

$$du_{ij} = \frac{X_{ij}}{\rho_{ij}}\left(\frac{dX_{ij}}{X_{ij}} - \frac{d\rho_{ij}}{\rho_{ij}}\right) \tag{6.19}$$

therefore:

$$\frac{d\rho_j}{\rho_j} = \rho_j\sum_{i=1}^{Nc}\frac{X_{ij}}{\rho_{ij}}\left(\frac{d\rho_{ij}}{\rho_{ij}} - \frac{dX_{ij}}{X_{ij}}\right) \tag{6.20}$$

In order to find $\frac{dS_j}{S_j}$ we return to the definition of z_1. Using Eq. 6.5 and for $Np = 2$ and $Nc = 2$:

$$z_1 = \frac{G_1}{F} = \frac{(\rho_1 X_{11} - \rho_2 X_{12})S_1 + \rho_2 X_{12}}{(\rho_1 - \rho_2)S_1 + \rho_2} \tag{6.21}$$

which on rearrangement gives:

$$S_1 = \frac{\rho_2(z_1 - X_{12})}{\rho_2(z_1 - X_{12}) - \rho_1(z_1 - X_{11})} \tag{6.22}$$

Substitution of the variables:

$$v_{11} = \rho_1(z_1 - X_{11}) \qquad\qquad v_{12} = \rho_2(z_1 - X_{12}) \tag{6.23}$$

and using the quotient rule and the fact that:

$$\begin{aligned} S_2 &= 1 - S_1 \\ &= 1 - \frac{v_{12}}{v_{12} - v_{11}} = -\frac{v_{11}}{v_{12} - v_{11}} \end{aligned} \tag{6.24}$$

leads to the following expression:

$$\begin{aligned} \frac{dS_1}{S_1} &= \frac{dv_{11}}{v_{12} - v_{11}} + \frac{S_2}{S_1}\frac{1}{v_{12} - v_{11}}dv_{12} \\ &= \frac{1}{v_{12} - v_{11}}\left(dv_{11} - \frac{v_{11}}{v_{12}}dv_{12}\right) \\ &= -S_2\left(\frac{dv_{11}}{v_{11}} - \frac{dv_{12}}{v_{12}}\right) \end{aligned} \tag{6.25}$$

Additionally, using the product rule, we have:

$$\frac{dv_{11}}{v_{11}} = \left(\frac{d(z_1 - X_{11})}{(z_1 - X_{11})} + \frac{d\rho_1}{\rho_1}\right) \qquad \frac{dv_{12}}{v_{12}} = \left(\frac{d(z_1 - X_{12})}{(z_1 - X_{12})} + \frac{d\rho_2}{\rho_2}\right) \tag{6.26}$$

Expression for $\frac{\partial F}{\partial z_1}$

From Eq. (6.15) the derivative of F with respect to z_1 for two phases and two components is given by:

$$\frac{\partial F}{\partial z_1} = \frac{F}{\phi}\frac{\partial \phi}{\partial z_1} + \phi\left[\rho_1 S_1\left(\frac{1}{\rho_1}\frac{\partial \rho_1}{\partial z_1} + \frac{1}{S_1}\frac{\partial S_1}{\partial z_1}\right) + \rho_2(1-S_1)\left(\frac{1}{\rho_2}\frac{\partial \rho_2}{\partial z_1} + \frac{1}{(1-S_1)}\frac{\partial (1-S_1)}{\partial z_1}\right)\right] \tag{6.27}$$

As porosity, ϕ, does not depend on z_1:

$$\frac{\partial \phi}{\partial z_1} = 0 \tag{6.28}$$

and Eq. (6.27) becomes:

$$\frac{\partial F}{\partial z_1} = \phi\left[\rho_1 S_1\left(\frac{1}{\rho_1}\frac{\partial \rho_1}{\partial z_1} + \frac{1}{S_1}\frac{\partial S_1}{\partial z_1}\right) + \rho_2(1-S_1)\left(\frac{1}{\rho_2}\frac{\partial \rho_2}{\partial z_1} - \frac{1}{(1-S_1)}\frac{\partial S_1}{\partial z_1}\right)\right] \tag{6.29}$$

The partial derivatives on the right hand side of Eq. (6.29) are as follows:

$$\frac{1}{S_1}\frac{\partial S_1}{\partial z_1} = -S_2\left(\frac{1}{v_{11}}\frac{\partial v_{11}}{\partial z_1} - \frac{1}{v_{12}}\frac{\partial v_{12}}{\partial z_1}\right) \tag{6.30}$$

where:

$$\frac{1}{v_{11}}\frac{\partial v_{11}}{\partial z_1} = \frac{1}{\rho_1}\frac{\partial \rho_1}{\partial z_1} + \frac{1}{(z_1 - X_{11})}\left(1 - \frac{\partial X_{11}}{\partial z_1}\right) \tag{6.31}$$

$$\frac{1}{v_{12}}\frac{\partial v_{12}}{\partial z_1} = \frac{1}{\rho_2}\frac{\partial \rho_2}{\partial z_1} + \frac{1}{(z_1 - X_{12})}\left(1 - \frac{\partial X_{12}}{\partial z_1}\right) \tag{6.32}$$

and:

$$\frac{1}{\rho_1}\frac{\partial \rho_1}{\partial z_1} = \rho_1\left(\frac{1}{\rho_{21}} - \frac{1}{\rho_{11}}\right)\frac{\partial X_{11}}{\partial z_1} \tag{6.33}$$

$$\frac{1}{\rho_2}\frac{\partial \rho_2}{\partial z_1} = \rho_2 \left(\frac{1}{\rho_{22}} - \frac{1}{\rho_{12}} \right) \frac{\partial X_{12}}{\partial z_1} \tag{6.34}$$

using Eq. (6.6) and the fact that $\frac{\partial \rho_{ij}}{\partial z_1} = 0$

In our model $\frac{\partial F}{\partial z_1}$ is piecewise depending on which phases are present (see Section 6.3).

Derivation of $\frac{\partial F}{\partial z_1}$ for condition A

For condition A only phase 1 is present so phase saturations are:

$$S_1 = 1, \qquad S_2 = 0 \tag{6.35}$$

Substitution of Eq. (6.35) into Eqs. (6.29) and (6.30) gives:

$$\frac{\partial F}{\partial z_1} = \phi \left[\rho_1 \left(\frac{1}{\rho_1} \frac{\partial \rho_1}{\partial z_1} \right) \right] \tag{6.36}$$

Also:

$$\frac{\partial X_{11}}{\partial z_1} = 1 \tag{6.37}$$

which on substitution into Eq. (6.33) leads to:

$$\frac{1}{\rho_1}\frac{\partial \rho_1}{\partial z_1} = \rho_1 \left(\frac{1}{\rho_{21}} - \frac{1}{\rho_{11}} \right) \tag{6.38}$$

Substitution of Eq. (6.38) into Eq. (6.36) gives the expression for $\frac{\partial F}{\partial z_1}$ when only phase 1 is present.

Derivation of $\frac{\partial F}{\partial z_1}$ for condition C

For condition C only phase 2 is present so phase saturations are:

$$S_1 = 0, \qquad S_2 = 1 \tag{6.39}$$

Substitution of Eq. (6.39) into Eqs. (6.29) and (6.30) gives:

$$\frac{\partial F}{\partial z_1} = \phi \left[\rho_2 \left(\frac{1}{\rho_2} \frac{\partial \rho_2}{\partial z_1} \right) \right] \tag{6.40}$$

As:

$$\frac{\partial X_{12}}{\partial z_1} = 1 \tag{6.41}$$

we get:

$$\frac{1}{\rho_2} \frac{\partial \rho_2}{\partial z_1} = \rho_2 \left(\frac{1}{\rho_{22}} - \frac{1}{\rho_{12}} \right) \tag{6.42}$$

which on substitution into Eq. (6.40) gives the expression for $\frac{\partial F}{\partial z_1}$ when only phase 2 is present.

Derivation of $\frac{\partial F}{\partial z_1}$ for condition B

If we have two phases present (condition B):

$$0 < S_1 < 1, \qquad 0 < S_2 < 1 \tag{6.43}$$

Component mass fractions, X_{ij}, are assumed to be equal to equilibrium mass fractions x_{ij} therefore:

$$\frac{\partial X_{11}}{\partial z_1} = \frac{\partial x_{11}}{\partial z_1} = 0, \qquad \frac{\partial X_{12}}{\partial z_1} = \frac{\partial x_{12}}{\partial z_1} = 0 \tag{6.44}$$

and:

$$\frac{1}{\rho_1}\frac{\partial \rho_1}{\partial z_1} = 0, \qquad \frac{1}{\rho_2}\frac{\partial \rho_2}{\partial z_1} = 0 \tag{6.45}$$

Substitution of Eqs. (6.44) and (6.45) and into Eq. (6.29) gives:

$$\frac{\partial F}{\partial z_1} = \phi\left[\rho_1 S_1\left(\frac{1}{S_1}\frac{\partial S_1}{\partial z_1}\right) + \rho_2(1-S_1)\left(-\frac{S_1}{(1-S_1)}\left(\frac{1}{S_1}\frac{\partial S_1}{\partial z_1}\right)\right)\right] \tag{6.46}$$

Using Eqs. (6.44) and (6.45) Eq. (6.30) becomes:

$$\frac{1}{S_1}\frac{\partial S_1}{\partial z_1} = -S_2\left(\frac{1}{(z_1 - X_{11})} - \frac{1}{(z_1 - X_{12})}\right) \tag{6.47}$$

which on substitution into Eq. (6.46) gives the expression for $\frac{\partial F}{\partial z_1}$ when two phases are present.

Expression for $\frac{\partial F}{\partial P}$

After Eq. (6.15) the derivative of F with respect to P for two phases and two components is:

$$\frac{\partial F}{\partial P} = \frac{F}{\phi}\frac{\partial \phi}{\partial P} + \phi\left[\rho_1 S_1\left(\frac{1}{\rho_1}\frac{\partial \rho_1}{\partial P} + \frac{1}{S_1}\frac{\partial S_1}{\partial P}\right) + \rho_2(1-S_1)\left(\frac{1}{\rho_2}\frac{\partial \rho_2}{\partial P} + \frac{1}{(1-S_1)}\frac{\partial (1-S_1)}{\partial P}\right)\right] \tag{6.48}$$

$\frac{1}{\phi}\frac{\partial \phi}{\partial P}$ is defined as the rock compressibility c_r:

$$\frac{1}{\phi}\frac{\partial \phi}{\partial P} = c_r \tag{6.49}$$

Phase compressibilities, c_j, are given by:

$$c_j = \frac{1}{\rho_j}\frac{\partial \rho_j}{\partial P_j} = \rho_j\left[\sum_{i=1}^{Nc}\frac{X_{ij}}{\rho_{ij}}\left(c_{ij} + \frac{1}{X_{ij}}\frac{\partial X_{ij}}{\partial P_j}\right)\right] \tag{6.50}$$

where component compressibilities, c_{ij}, are found from the equation of state (Section 3.3).

Using Eq. (6.50):

$$\frac{1}{\rho_j}\frac{\partial \rho_j}{\partial P} = \frac{1}{\rho_j}\frac{\partial \rho_j}{\partial P_j}\frac{\partial P_j}{\partial P} = c_j \frac{\partial P_j}{\partial P} \tag{6.51}$$

The derivative of individual phase pressures with respect to the total pressure is found as follows. Using Eqs. (6.7) and (6.8):

$$\begin{aligned} P &= P_1(1 - S_2) + P_2 S_2 \\ &= P_1 + (P_2 - P_1)S_2 \\ &= P_1 - P_c S_2 \end{aligned} \tag{6.52}$$

As $P_c = P_c(S_1)$ the total derivative of P_1 is given by:

$$dP_1 = dP - P_c dS_1 + (1 - S_1)\frac{\partial P_c}{\partial S_1} dS_1 \tag{6.53}$$

$\frac{\partial P_1}{\partial P}$ is then:

$$\frac{\partial P_1}{\partial P} = 1 + \left((1 - S_1)\frac{\partial P_c}{\partial S_1} - P_c\right)\frac{\partial S_1}{\partial P} \tag{6.54}$$

Similarly:

$$\frac{\partial P_2}{\partial P} = 1 - \left(S_1 \frac{\partial P_c}{\partial S_1} + P_c\right)\frac{\partial S_1}{\partial P} \tag{6.55}$$

The partial derivative $\frac{\partial S_1}{\partial P}$ is given by:

$$\frac{1}{S_1}\frac{\partial S_1}{\partial P} = -S_2\left(\frac{1}{v_{11}}\frac{\partial v_{11}}{\partial P} - \frac{1}{v_{12}}\frac{\partial v_{12}}{\partial P}\right) \tag{6.56}$$

In terms of phase pressures this becomes:

$$\frac{1}{S_1}\frac{\partial S_1}{\partial P} = -S_2\left(\frac{1}{v_{11}}\frac{\partial v_{11}}{\partial P_1}\frac{\partial P_1}{\partial P} - \frac{1}{v_{12}}\frac{\partial v_{12}}{\partial P_2}\frac{\partial P_2}{\partial P}\right) \tag{6.57}$$

Using Eq. (6.26) and the fact that $\frac{\partial z_1}{\partial P} = 0$ we have:

$$\begin{aligned}\frac{1}{v_{11}}\frac{\partial v_{11}}{\partial P_1} &= \frac{1}{\rho_1}\frac{\partial \rho_1}{\partial P_1} - \frac{1}{z_1 - X_{11}}\frac{\partial X_{11}}{\partial P_1} \\ &= c_1 - \frac{1}{z_1 - X_{11}}\frac{\partial X_{11}}{\partial P_1}\end{aligned} \tag{6.58}$$

$$\begin{aligned}\frac{1}{v_{12}}\frac{\partial v_{12}}{\partial P_2} &= \frac{1}{\rho_2}\frac{\partial \rho_2}{\partial P_2} - \frac{1}{z_1 - X_{12}}\frac{\partial X_{12}}{\partial P_2} \\ &= c_2 - \frac{1}{z_1 - X_{12}}\frac{\partial X_{12}}{\partial P_2}\end{aligned} \tag{6.59}$$

with c_1 and c_2 given by Eq. (6.50).

For single phase conditions S_1 is constant so $\frac{\partial S_1}{\partial P} = 0$. For two phase conditions X_{11} and X_{12} are equal to equilibrium mass fractions x_{11} and x_{12} respectively. $\frac{\partial X_{11}}{\partial P_1}$ and $\frac{\partial X_{12}}{\partial P_2}$ are approximated from the equation of state using first order forward finite differences.

Substituting Eqs. (6.54), (6.55), (6.58) and (6.59) into Eq. (6.57) gives:

$$\frac{1}{S_1}\frac{\partial S_1}{\partial P} = -S_2\left(\frac{1}{v_{11}}\frac{\partial v_{11}}{\partial P_1}\left[1 + \left((1 - S_1)\frac{\partial P_c}{\partial S_1} - P_c\right)\frac{\partial S_1}{\partial P}\right] - \frac{1}{v_{12}}\frac{\partial v_{12}}{\partial P_2}\left[1 - \left(S_1\frac{\partial P_c}{\partial S_1} + P_c\right)\frac{\partial S_1}{\partial P}\right]\right) \tag{6.60}$$

Rearrangement of Eq. (6.60) then gives:

$$\frac{\partial S_1}{\partial P} = \left[\frac{1}{v_{11}}\frac{\partial v_{11}}{\partial P_1} - \frac{1}{v_{12}}\frac{\partial v_{12}}{\partial P_2}\right]\left[-\frac{1}{S_1 S_2} - \frac{1}{v_{11}}\frac{\partial v_{11}}{\partial P_1}\left(S_2\frac{\partial P_c}{\partial S_1} - P_c\right) - \frac{1}{v_{12}}\frac{\partial v_{12}}{\partial P_2}\left(S_1\frac{\partial P_c}{\partial S_1} + P_c\right)\right]^{-1} \tag{6.61}$$

Substitution of Eqs. (6.49), (6.51) and (6.56) into Eq. (6.48) leads to the expression for $\frac{\partial F}{\partial P}$. Once we know $\frac{\partial F}{\partial z_1}$ and $\frac{\partial F}{\partial P}$ we can calculate $\frac{\partial P}{\partial t}$ using Eq. (6.14).

Chapter 7

Convection patterns beneath an injected plume of CO_2

Summary

This chapter describes work carried out using the two-phase, two-component miscible flow model developed in Chapter 6.

The main objective of the work was to build a model with which to investigate the interaction between the larger scale processes of CO_2 injection and migration and the smaller scale dissolution and convection processes.

The model performed well when benchmarked against analytical solutions for the plume diameter and pressure buildup. However, resolution testing indicates that model results are highly dependent on grid resolution. Therefore in its current state the model is not robust enough to accurately model the problem described above. Further refinement of the grid is required but numerical instabilities have caused higher resolution models to crash. Future work should focus on improving the accuracy of the numerical scheme used so that simulations can be run with a high enough resolution to be able to resolve individual convective fingers.

7.1 Introduction

In order to satisfy safety requirements it is important for us to be able to predict the migration of CO_2 within the reservoir. As part of this we need to study dissolution of CO_2 and its

subsequent migration in the aqueous phase as dissolved CO_2 will behave in a different way, for instance in terms of buoyancy and reactivity, to gaseous CO_2.

Dissolution of CO_2 into brine renders the brine negatively buoyant compared to brine with no CO_2 in it, leading to a downward migration of CO_2. This is an important phenomenon because downwards migration of CO_2 moves it away from the atmosphere and reduces the likelihood of CO_2 reaching the surface and escaping. Accordingly the tendency for CO_2 dissolution should be considered when selecting suitable CO_2 storage sites.

The location of dissolved CO_2 exerts a major control on the processes of mineral dissolution and precipitation (Audigane *et al.*, 2007). Brine acidification caused by CO_2 dissolution can lead to dissolution of existing minerals within the reservoir and caprock and the precipitation of new carbonate minerals. Whilst the precipitation of carbonate minerals is beneficial for permanent storage of CO_2, the initial dissolution of in situ minerals, particularly within the caprock, can lead to an increase in caprock permeability and consequently a reduction in storage security (Armitage *et al.*, 2013; Smith *et al.*, 2013). Therefore accurate modelling of dissolution rates of CO_2 and the movement of dissolved CO_2 is important.

7.1.1 The likelihood of CO_2 dissolution

There are various ways that we can investigate CO_2 dissolution in saline aquifers. One way is to study accumulations of CO_2 which occur naturally. Isotope studies of natural underground CO_2 accumulations suggest that significant CO_2 dissolution has taken place in the past. Gilfillan *et al.* (2009) suggest that CO_2 dissolution is a major trapping mechanism, over timescales of thousands to millions of years, based on estimated emplacement dates of CO_2 and estimated amounts of dissolved CO_2 at various natural CO_2 reservoirs. Additionally comparison of CO_2 dissolution rates to rates of pure diffusion at the Bravo Dome natural CO_2 store indicate that convection enhanced dissolution is likely to have occurred (Sathaye *et al.*, 2014).

Pilot studies of CO_2 injection and existing CCS projects also provide opportunity for us to explore CO_2 dissolution over shorter time periods. Analysis of ions present in fluid samples taken at the Nagaoka CCS Test Site in Japan indicate high dissolved CO_2 concentrations one year after the end of injection (Mito *et al.*, 2008). This result is supported by resistivity measurements from the same site which suggest the presence of dissolved CO_2 and can be used to loosely constrain the location of the dissolved CO_2 (Nakajima & Xue, 2013). Changes in

carbon isotope ratios studied as part of the CO2CRC Otway Project have been used to infer the arrival of a dissolved CO_2 front at fluid sampling locations (Boreham *et al.*, 2011).

Changes in time lapse seismic taken at various CO_2 injection locations indicate a loss of gaseous CO_2 which can possibly be attributed to CO_2 dissolution (Ivandic *et al.*, 2015; Chadwick *et al.*, 2005). However, estimates of CO_2 dissolution rates and locations from geophysical methods are very poorly constrained due to large uncertainties in the input data. Information about migration of dissolved CO_2 from fluid sampling is also ambiguous as data can only be collected from a few point sources within the reservoir.

Field scale numerical modelling of all aspects of CO_2 storage can provide a broad insight into the dissolution likely to occur in a realistic storage situation. Ghanbari *et al.* (2006) carried out modelling of a generic CO_2 storage site to identify the main controls on storage efficiency, particularly relating to hydrodynamic and dissolution trapping. They concluded that convection enhanced dissolution plays a major role in increasing CO_2 storage efficiency. Their simulations showed that downwelling of CO_2 saturated brine took place in concentric circles around a vertical injection well. Doughty (2010) modelled a potential CO_2 storage site to assess its suitability for CO_2 storage. The model was populated with realistic porosity and permeability data for the facies present in the reservoir. Convection enhanced dissolution was observed to occur in models with fewer horizontal, low permeability barriers.

Both these models indicate that dissolution of CO_2 is likely to have and impact on CO_2 storage. However, the grid resolution used was necessarily coarse in order to model the whole storage site and was not fine enough to capture small scale fingering dynamics of convection.

Pressure changes have been used as a proxy measure for CO_2 dissolution within sealed containers where CO_2 and water are allowed to mix, e.g. Farajzadeh *et al.* (2007); Mojtaba *et al.* (2014). In these studies dissolution rates are found to be greater than pure diffusion rates and this discrepancy has been attributed to convective dissolution. Mojtaba *et al.* (2014) were also able to find scaling relationships between Rayleigh number and CO_2 dissolution from their experiments.

7.1.2 CO_2 dissolution from a flat interface

Natural analogues, geophysical monitoring of existing sites and field scale numerical modelling can help constrain dissolution rates but are less suited to constraining spatial patterns of CO_2

dissolution and convection.

Modelling concentrating specifically on the process of CO_2 dissolution into brine, with the aim of investigating the spatial and temporal patterns of CO_2 convection, has been carried out in the laboratory as well as using mathematical and numerical methods.

Patterns of convective dissolution from a flat interface have been imaged in the laboratory by numerous authors (e.g Kneafsey & Pruess, 2010; Neufeld *et al.*, 2010). In these experiments two fluids of different densities, representing CO_2 and brine, are placed next to each other between two flat plates and allowed to mix under controlled conditions. Kneafsey & Pruess (2010) were able to image convection occurring as CO_2 dissolved into water from an initially flat boundary layer. Similar to this, Neufeld *et al.* (2010) observed convection occurring between two analogue fluids with properties similar to CO_2 and brine. Both studies qualitatively described the stages of convection through time. In their studies small scale convective fingers formed, coalesced into larger fingers and then descended, initiating larger scale flow patterns. Quantitatively the experimental results were used to estimate CO_2 dissolution fluxes through time. Neufeld *et al.* (2010) also developed scaling relations for different Rayleigh number experiments which could be used to estimate CO_2 dissolution rates at particular storage sites.

Several authors have investigated convection by undertaking analytical or numerical modelling of a single, aqueous phase system with a saturated concentration boundary above an initially unsaturated layer of brine (Riaz *et al.*, 2006; Ennis-King *et al.*, 2005; Xu *et al.*, 2006). These studies used analytical models to estimate onset times for convection and typical wavelengths of convective fingers under different permeability conditions. In these models onset time of convection and wavelength of convective fingers was found to be inversely proportional to reservoir permeability.

The studies described above provide an idea of the overall dynamics of convective fingering. However they do not include the effects of a laterally migrating CO_2 brine interface which is likely to be present in a realistic injection scenario.

7.1.3 CO_2 dissolution from an advancing interface

Work investigating the interaction of convection with an advancing CO_2-brine interface was undertaken by MacMinn *et al.* (2012) who carried out laboratory experiments using analogue fluids to investigate the influence of convection enhanced dissolution on the migration of a buoy-

ant plume of CO_2. The migrating gravity current was initiated by having less dense material, representing CO_2, initially to the right of a larger area of more dense material, representing brine. At the beginning of the experiment the system was allowed to mix causing the buoyant material ro rise and spread laterally along the top of the model.

The same setup was modelled numerically by Hidalgo *et al.* (2013). Both studies found that the accumulation of high density material beneath the migrating current limited the amount of convection which could occur. This is similar to the findings of Chapter 5 albeit with a slightly different configuration of the diffusive boundary layer. Hidalgo *et al.* (2013) were also able to use their simulations to observe three stages of dissolution: an initially diffusive stage followed by a constant dissolution flux and then a decaying of the dissolution flux as the accumulated dense material beneath the buoyant current suppressed convection.

The use of analogue fluids was required in order to image the processes in the laboratory. However, some characteristics of the analogue fluids were clearly different to the problem of CO_2 dissolving into brine. For instance, the mobility ratio between CO_2 and brine is much greater than the mobility ratios between the fluids modelled. Also the fluids modelled were completely miscible so no two phase effects were taken into account. These factors could potentially exert a major influence over convection patterns and plume behaviour.

MacMinn *et al.* (2011) produced a semi-analytical model to model the advance of a CO_2 plume under a tilted caprock. Subsequent laboratory modelling of the same problem by MacMinn & Juanes (2013) was also carried out. The effect of convection enhanced dissolution of the buoyant fluid on the up slope migration of the fluid was assessed. They found that the up slope movement of a buoyant plume was slowed and eventually halted by the continued depletion of the plume due to dissolution.

7.1.4 CO_2 dissolution under two phase conditions

Nearly all of work described above, which specifically addresses the process of CO_2 dissolution, neglects the effects of partial miscibility and capillarity between the gaseous phase and the aqueous phase.

Elenius *et al.* (2012, 2014) performed linear stability analysis and numerical modelling to explore the relationship between convection enhanced dissolution and the presence of a capillary fringe at the CO_2-brine interface. Their results indicate that capillary effects at the boundary

destabilise the system leading to reduced onset times for convection and increased dissolution rates.

Numerical simulations carried out by Emami-Meybodi & Hassanzadeh (2015) included capillary effects and volume change on mixing between the partially miscible phases. Similar to Elenius *et al.* (2012, 2014), they found a reduction in convection onset time and increased convective dissolution rates for models including volume change on mixing and capillarity.

Although these studies were performed under the assumption of a flat, static boundary between the CO_2 and brine, the results indicate the importance of being able to include partial miscibility and capillarity in models of the CO_2 dissolution process.

7.1.5 CO_2 dissolution from an advancing interface under two phase conditions

Pruess & Nordbotten (2011) carried out numerical simulations of CO_2 migrating up dip under a sloping caprock which included two phase effects. Their model was on a coarse scale so the process of convection enhanced dissolution was not explicitly modelled. Instead it was represented by the imposition of a CO_2 sink at the top of the model in the region where two phase conditions existed. Their results showed that although the flux of gaseous CO_2 migrating up dip was reduced by the dissolution, the velocity of the migrating CO_2 front was unchanged. This is contrary to the findings of MacMinn *et al.* (2011); MacMinn & Juanes (2013) who found that dissolution eventually caused the migrating gravity current to stop moving. However, Pruess & Nordbotten (2011) point out that their model is fairly crude and in other scenarios the velocity of the gravity current may well be reduced by dissolution of the migrating plume.

It is clear that partially miscible flow and the presence of a moving CO_2-brine interface will affect the process of CO_2 dissolution and associated convection. Despite this, very few studies have provided a detailed investigated the spatial and temporal patterns of CO_2 migration and dissolution including both these effects.

In this work a numerical model has been developed which models two phase flow and transport of CO_2 and brine with partial miscibility between the phases. Injection and subsequent migration of the CO_2 is modelled allowing us to explore in detail the convection enhanced dissolution process within a two phase, partially miscible flow regime, during and after injection

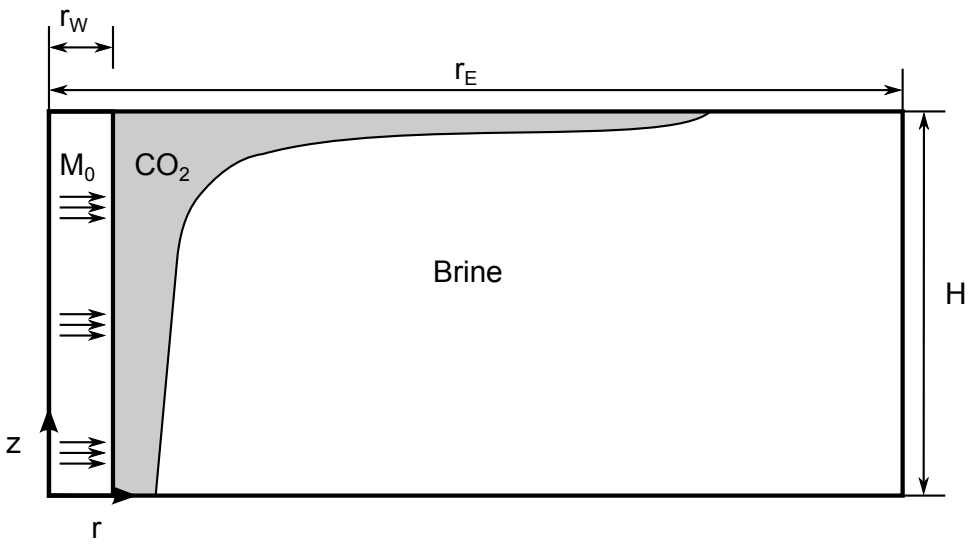

Figure 7.1: Model Setup

as well as the effect of dissolution on the advancing CO_2 plume. The model developed here uses a more realistic injection scenario compared to previous studies of dissolution and convection from a migrating interface (e.g MacMinn *et al.*, 2012; Hidalgo *et al.*, 2013). Convective dissolution has been modelled explicitly as opposed to being applied as a sink term as in Pruess & Nordbotten (2011).

7.2 Methodology

7.2.1 Model Description

A finite difference, two dimensional, radial flow model has been built to simulate two phase flow and transport of CO_2 and brine within a porous medium. Fluids are injected from the radial centre boundary of the model by specifying a mass flow rate for each component across the boundary. All other boundaries do not allow mass to flow across them (Fig. 7.1).

The two phases modelled are a gaseous phase consisting predominantly of supercritical CO_2 and an aqueous phase consisting predominantly of brine. We have used an equation of state which allows for miscibility of CO_2 and H_2O between the phases and encompasses volume change on mixing (Chapter 3). When two phases are present they are assumed to be in equilibrium (Section 6.3).

Darcy's Law is used to govern flow in the model (Eq. (2.6)) and a Fickian model of diffusion governs transport (Eq. (2.5)). The governing equations and the mathematical implementation

Parameter	Symbol	Value	Units
Well Radius	r_W	0.2	m
Reservoir radius	r_E	20	km
Reservoir thickness	H	0.1	km
Porosity	ϕ	0.2	-
Horizontal permeability	k_h	1.00×10^{-12}	m^2
Vertical permeability	k_v	1.00×10^{-13}	m^2
Temperature	T	40	°C
Initial pressure	P_{ini}	1.00×10^{7}	Pa
Effective diffusivity	D_E	4.00×10^{-10}	$m^2\ s^{-1}$
Salt mass fraction	X_s	0.105	-
Critical gas saturation	S_{1_c}	0	-
Residual brine saturation	S_{2_r}	0	-
Endpoint relative permeability - gas	$k_{r_{10}}$	0.3	m^2
Endpoint relative permeability - brine	$k_{r_{20}}$	1	m^2
Relative permeability power law exponent - brine	m	3	-
Relative permeability power law exponent - gas	n	3	-
Capillary pressure van Genuchten parameter	P_{c0}	19600	Pa
Capillary pressure van Genuchten parameter	m_v	0.46	-
Rock compressibility	c_r	4.50×10^{-10}	Pa^{-1}
CO_2 injection rate	M_0	15	$kg\ s^{-1}$
Gravity	g	9.81	m^{-2}

Table 7.1: Model input parameters.

of the model are described in further detail in Section 2.2 and Chapter 6 respectively.

The governing equations have been solved using the method of lines whereby they have been discretised in space using finite differences and subsequently integrated in time by the inbuilt MATLAB ode solver `ode15s` (see Section 2.3 for more details).

Model geometry and initial and boundary conditions are shown in Table 7.1. The model dimensions and parameters are chosen to be representative of a typical saline aquifer.

Horizontal grid resolution increases logarithmically away from the injection boundary. Vertical grid resolution is constant throughout the model.

7.3 Benchmarking

7.3.1 Pressure buildup and CO_2 migration

The MATLAB model has been compared to the analytical model of (Mathias *et al.*, 2011).

Mathias *et al.* (2011) provide an analytical solution which gives the vertically averaged pressure and CO_2 saturation for injection of CO_2 into a radial aquifer. The analytical model assumes vertical equilibrium (i.e. no flow in the vertical direction), no capillary pressure,

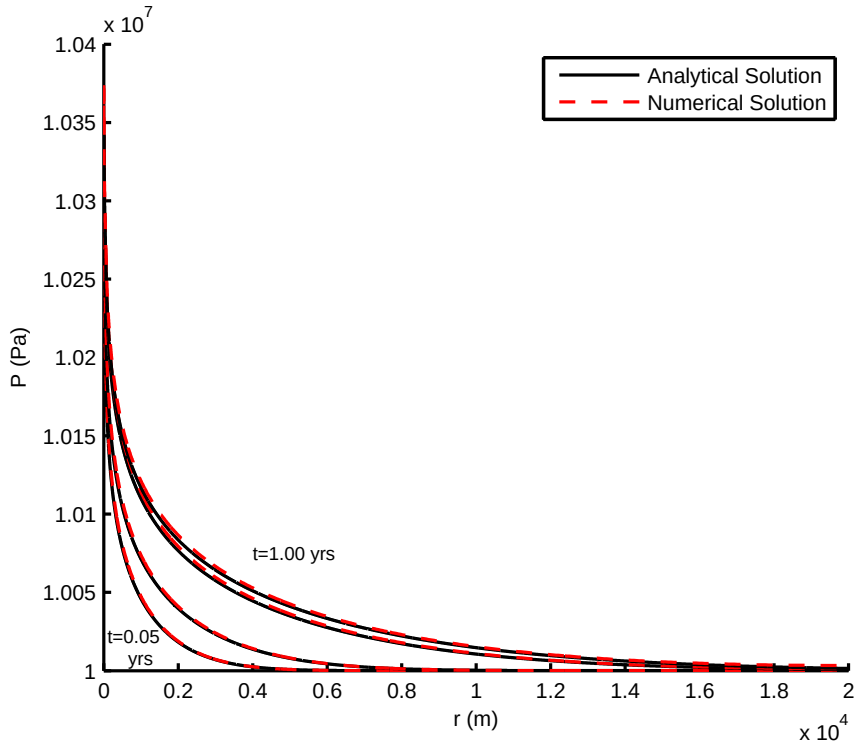

Figure 7.2: Comparison of MATLAB model with Mathias *et al.* (2011) for vertically averaged total pressure, P, at $t = 0.05$, 0.15, 0.75 and 1.00 years.

constant fluid properties which do not vary with pressure changes in the model and no flow boundaries on all sides except at the well.

The MATLAB model has been run with no vertical flow and with capillary pressure in order to provide a better comparison with the analytical solution. However, fluid properties have been allowed to vary with pressure.

Fig. 7.2 shows the results for vertically averaged pressure for both models. Overall results from both models are very similar. Fig. 7.3 shows the same results plotted with the radial distance scaled logarithmically to allow closer inspection of the pressure profile close to the well. Close to the well the MATLAB model exhibits higher pressure than the analytical model.

Comparison of results for CO_2 migration between the numerical and analytical solutions also shows good agreement between the models (Fig. 7.4). The migrating front in the numerical solution is not as sharp as in the analytical solution. Close to the well the numerical solution underestimates the CO_2 mass fraction compared to the analytical solution (Fig. 7.5).

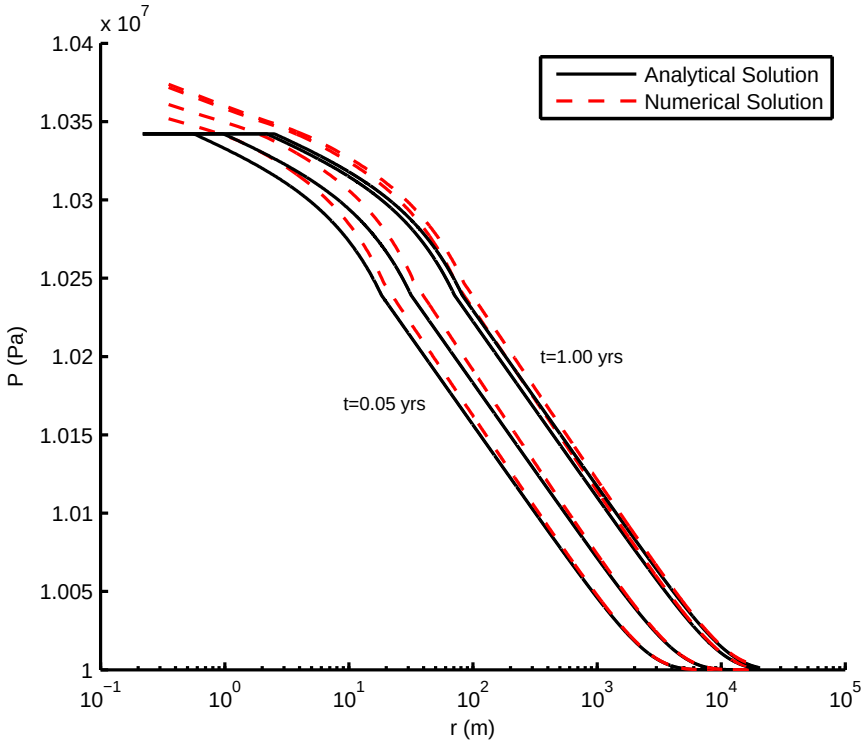

Figure 7.3: Comparison of MATLAB model with Mathias *et al.* (2011) for vertically averaged total pressure, P, at $t = 0.05$, 0.15, 0.75 and 1.00 years. Data is plotted with radial distance, r, on a logarithmic scale to allow better comparison of the models close to the injection well.

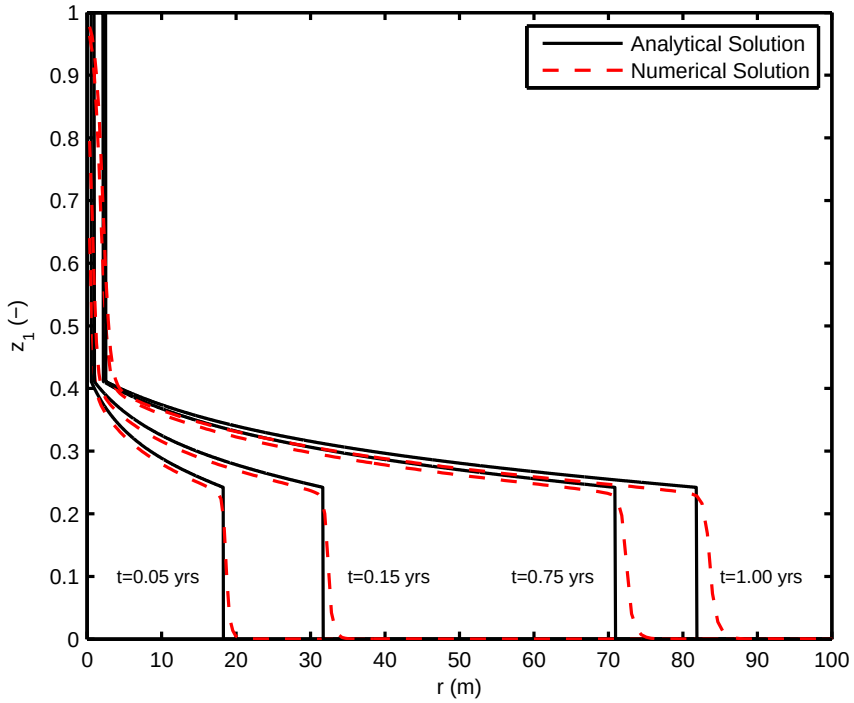

Figure 7.4: Comparison of MATLAB model with Mathias *et al.* (2011) for CO_2 mass fraction, z_1, at $t = 0.05$, 0.15, 0.75 and 1.00 years.

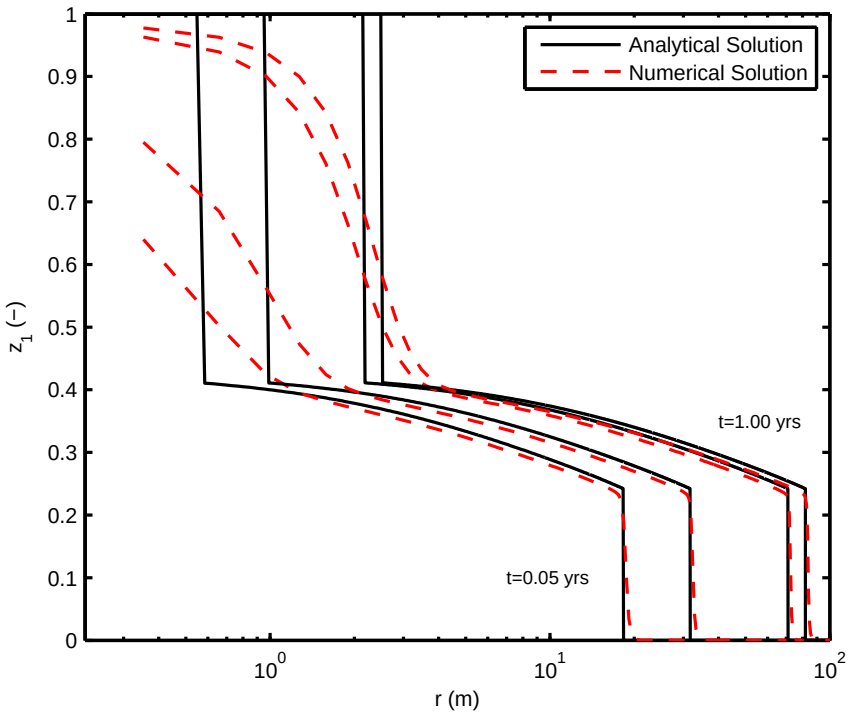

Figure 7.5: Comparison of MATLAB model with Mathias *et al.* (2011) for CO_2 mass fraction, z_1, at $t = 0.05$, 0.15, 0.75 and 1.00 years. Data is plotted with radial distance, r, on a logarithmic scale to allow better comparison of the models close to the injection well.

7.3.2 Resolution testing

Resolution testing has been carried out to find the grid resolution at which the model results converge.

Simulations were run for 1000 years in total with an injection rate of 15 kg s^{-1} of CO_2 applied for the first 20 years of the simulation.

The number of grid cells in the radial direction, n_r, was varied between $n_r = 30$ and $n_r = 400$. The number of grid cells in the vertical direction, n_z, was varied between $n_z = 30$ and $n_z = 200$.

Table 7.2 shows the minimum (closest to the well) and maximum (closest to the outer boundary) grid cell sizes for different values of n_r. The size of grid cells in the radial direction increases logarithmically away from the injection well.

Numerical issues meant that no models with $n_z > 50$ were able to run for the full 1000 years.

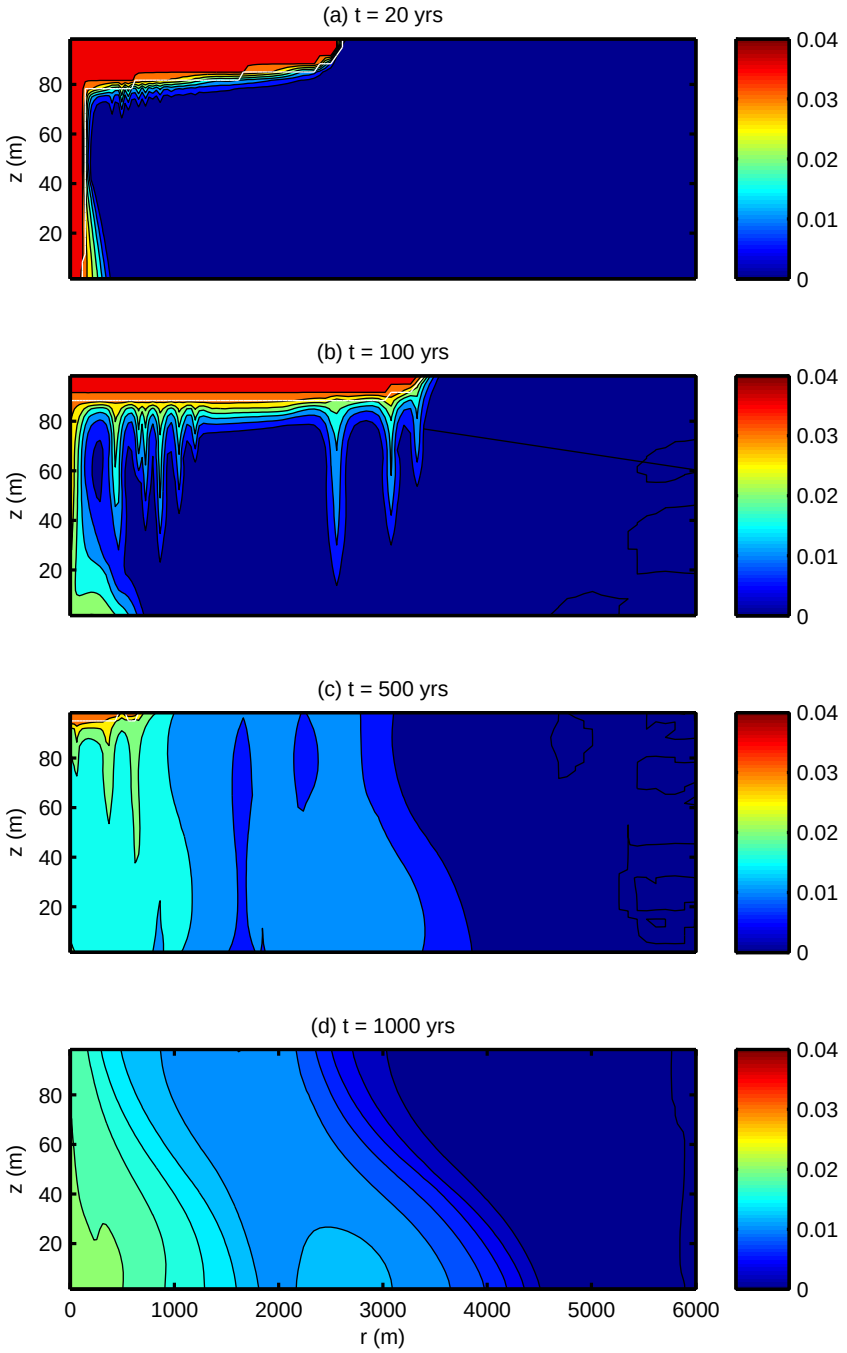

Figure 7.6: Mass fraction of CO_2 in the aqueous phase, X_{12}, through time. $n_r = 100, n_z = 30$. White line indicates the boundary between the two phase region and the single phase, aqueous region

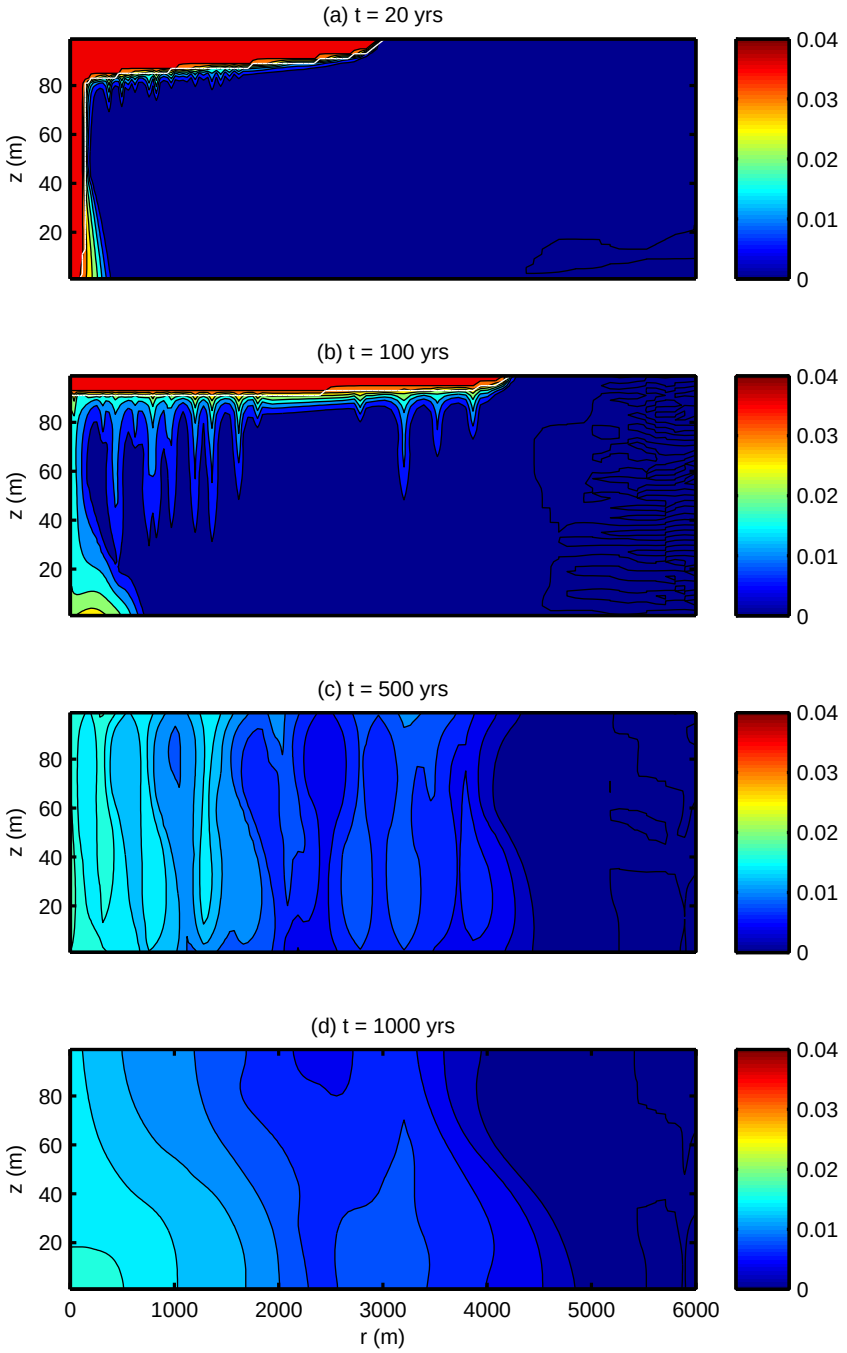

Figure 7.7: Mass fraction of CO_2 in the aqueous phase, X_{12}, through time. $n_r = 100, n_z = 50$. White line indicates the boundary between the two phase region and the single phase, aqueous region

n_r	Min. cell size (m)	Max. cell size (m)
30	177.3	1641.8
50	104.7	1000.2
100	51.8	505.8
150	34.4	338.5
200	25.7	254.4
250	20.6	203.7
350	14.7	145.7
400	12.8	127.6

Table 7.2: Grid cell sizes

Changing vertical resolution

Figs. 7.6 and 7.7 show the mass fraction of CO_2 in the aqueous phase, X_{12}, through time, for $n_z = 30$ and $n_z = 50$. Both have $n_r = 100$. Above the white line is the two phase region. Below the white line is the single phase aqueous region. Where no white line is present all the gaseous CO_2 has been dissolved.

The CO_2 has risen after injection and started to spread laterally along the impermeable boundary at the top of the model. Both models show some small scale convective downwelling after 20 years, close to the injection well. After 100 years the region containing free phase CO_2 has spread out further and thinned. Convection is more vigorous. A greater number of convective fingers have formed which have grown in size compared to those present at 20 years. After 500 years the convective fingers have started to coalesce into larger fingers. Some have begun interacting with the base of the model and spreading out along the bottom.

At all times the lateral extent of the two phase region and dissolved CO_2 in the model with $n_z = 30$ is not as great as in the model with $n_z = 50$. The vertical extent of the two phase region is greater for lower vertical resolution. After 500 years there is still some free phase CO_2 left in the model with $n_z = 30$ which is not present in the higher resolution model.

In terms of convection there are fewer distinct convective fingers in the lower resolution model at each timestep compared to the higher resolution model. However, fingers in the lower resolution model appear to be bigger both vertically and horizontally. Fingers in the lower resolution model interact with the bottom boundary sooner.

The irregular black lines to the right hand side of Figs. 7.6 and 7.7 indicate that there is noise present in the solution.

Figs. 7.8 and 7.9 show CO_2 rates and total dissolved CO_2 for models with $n_z = 30$ and

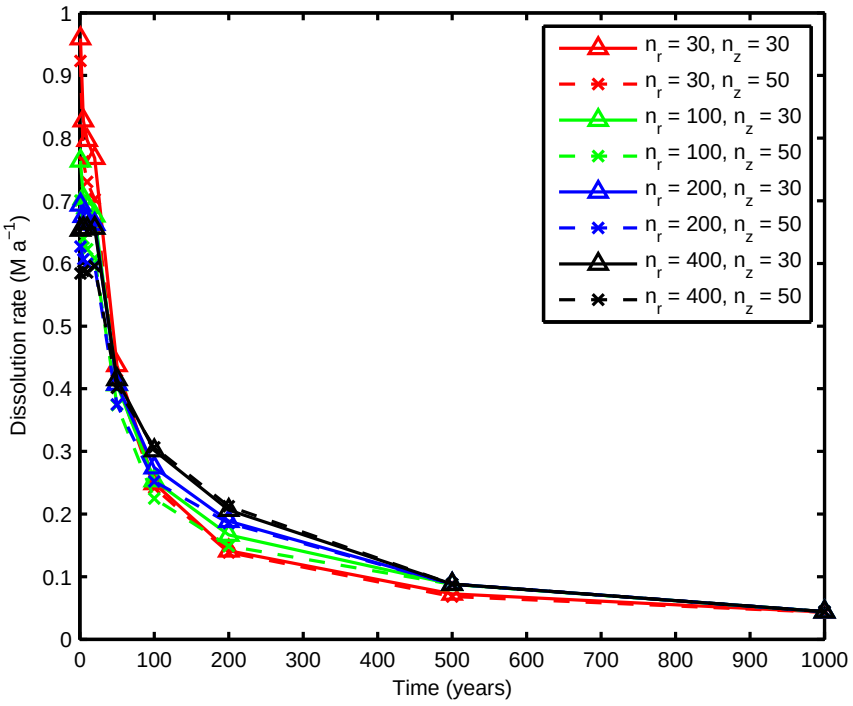

Figure 7.8: CO_2 dissolution rate for models with varying vertical resolution

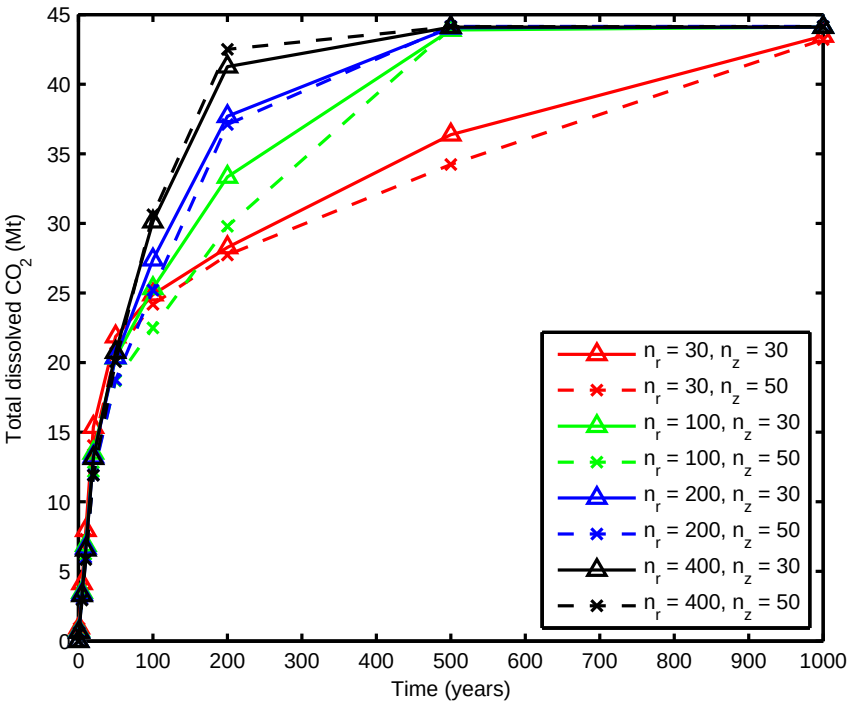

Figure 7.9: Total amount of dissolved CO_2 for models with varying vertical resolution

$n_z = 50$. Comparison of models with the same value of n_r shows that quantitatively CO_2 dissolution rates and total amounts of dissolved CO_2 do not vary much with n_z.

Changing horizontal resolution

Figs. 7.10 and 7.11 show the mass fraction of CO_2 in the aqueous phase, X_{12}, through time, for $n_r = 100$ and $n_r = 400$. Both have $n_z = 50$. Again the white line defines the boundary between the two phase region and the single phase, aqueous region. Overall characteristics of the evolution of dissolved CO_2 in the models is similar to that described above, in that small convective fingers form at first, coalesce and descend to the bottom where they interact with the bottom boundary and spread laterally.

The two phase region in the model with lower horizontal resolution extends further than in the model with higher horizontal resolution. After 500 years there is still some free phase CO_2 present in the lower resolution model. This isn't present in the higher resolution model.

Convective fingers have formed in both models after 20 years although a lot more fingers have formed in the higher resolution model. After 100 years the higher resolution model shows lots of narrow convective fingers which have nearly reached the bottom of the model. In contrast the largest convective finger in the lower resolution model has only reached 40 m depth after 100 years. After 500 years the fingers in the lower resolution model are still present and most of them have not reached the bottom of the model. In the higher resolution model fingers have coalesced and dissolved CO_2 has started to move laterally along the bottom of the model. This continues until 1000 years where no individual fingers are seen. After 1000 years it is still possible to see individual fingers in the lower resolution model although they have started to coalesce and spread laterally due to the influence of the bottom boundary.

The solutions shown in Figs. 7.10 and 7.11 exhibit quite a bit of noise on the right hand side of the plots.

Comparison of the CO_2 dissolution rate (Fig. 7.12) shows that although initially the highest dissolution rate is found in the lowest resolution model, through time this changes and the higher resolution models exhibit higher dissolution rates at later times. This manifests itself in the total amount of dissolved CO_2 as can be seen in Fig. 7.13 where total amount of dissolved CO_2 increases with model resolution at later times. At 500 years all models except the lowest resolution model contain the maximum amount of dissolved CO_2 (i.e. all CO_2 has been dissolved).

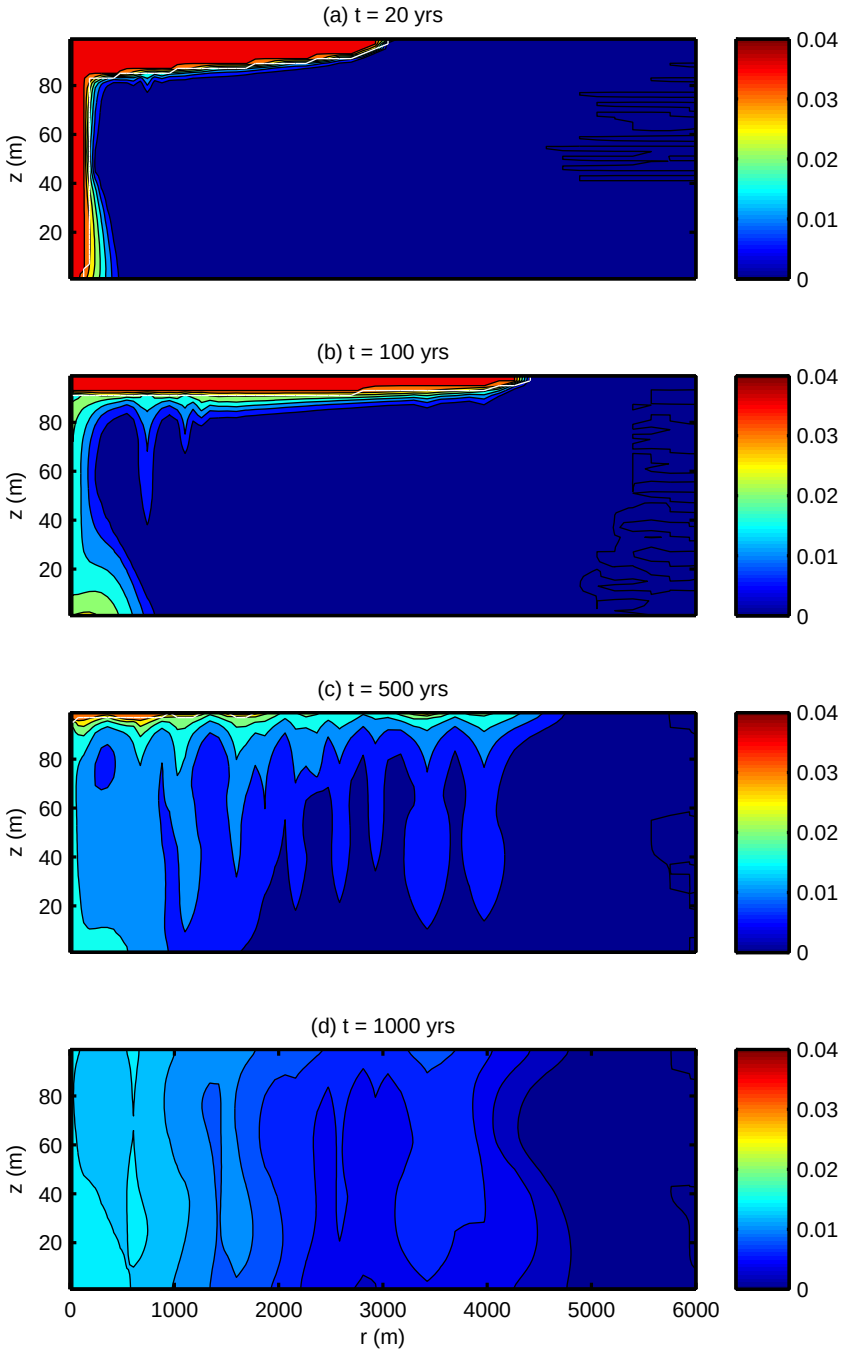

Figure 7.10: Mass fraction of CO_2 in the aqueous phase, X_{12}, through time. $n_r = 100, n_z = 50$. White line indicates the boundary between the two phase region and the single phase, aqueous region

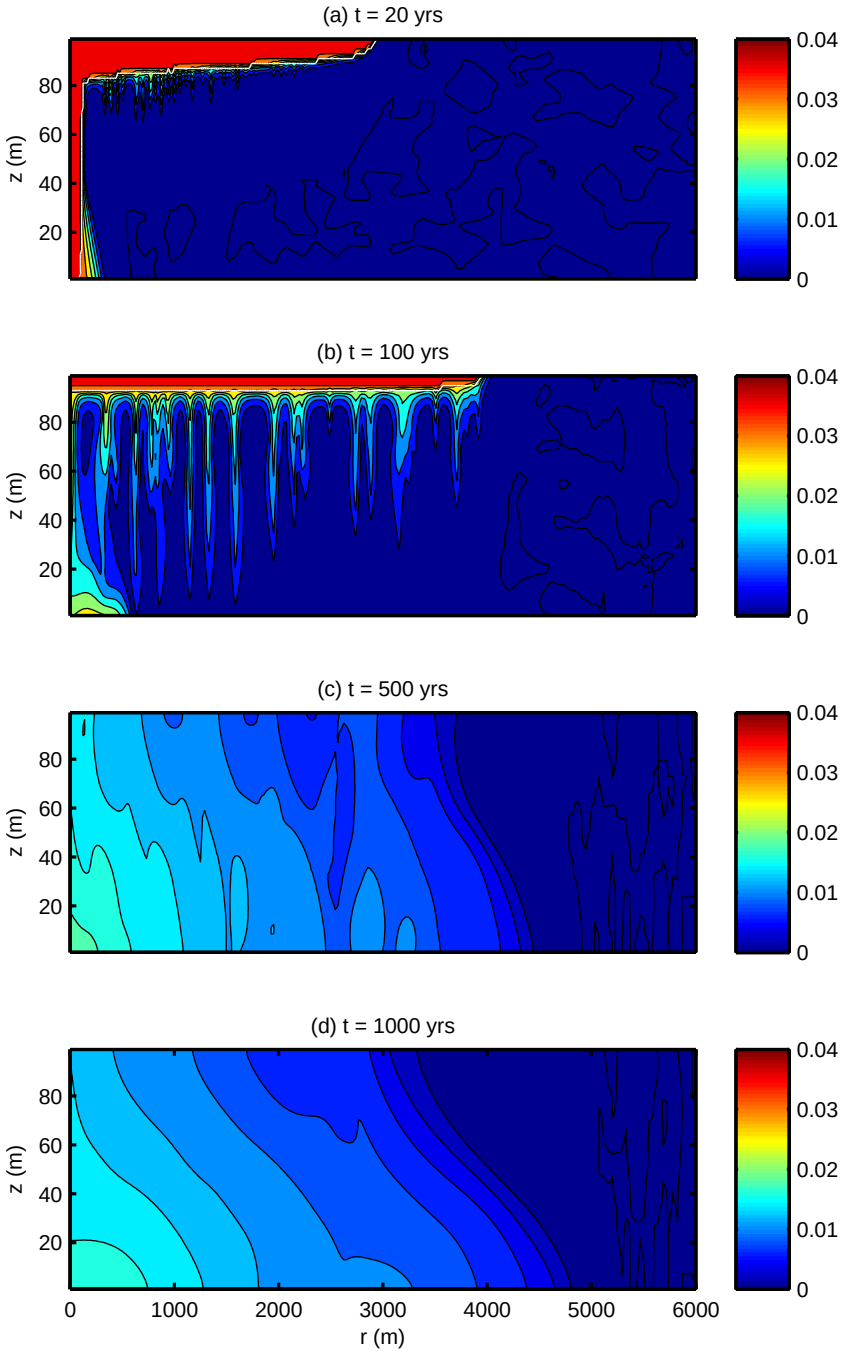

Figure 7.11: Mass fraction of CO_2 in the aqueous phase, X_{12}, through time. $n_r = 400, n_z = 50$. White line indicates the boundary between the two phase region and the single phase, aqueous region

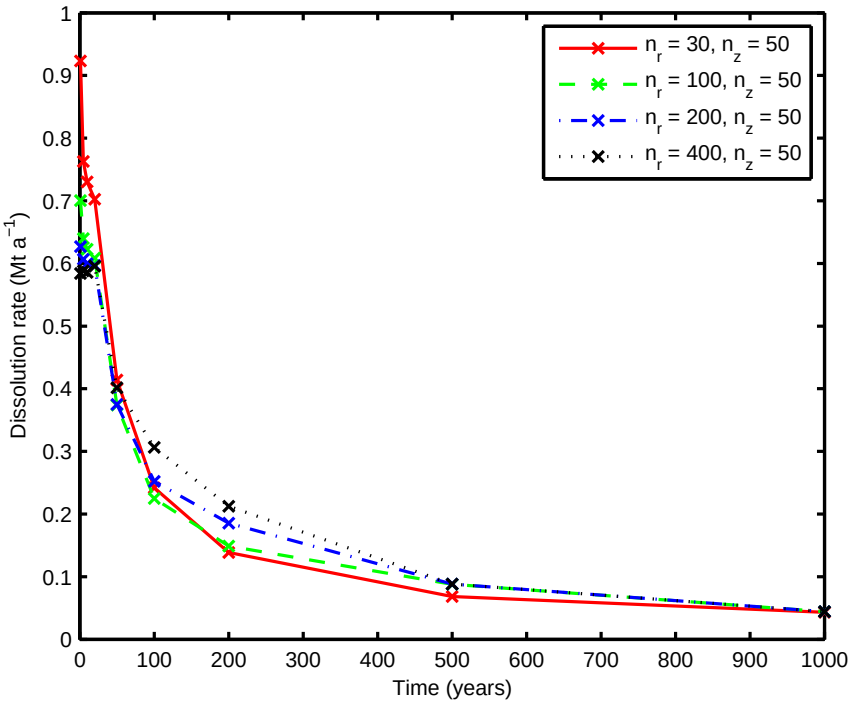

Figure 7.12: CO_2 dissolution rate for models with varying horizontal resolution

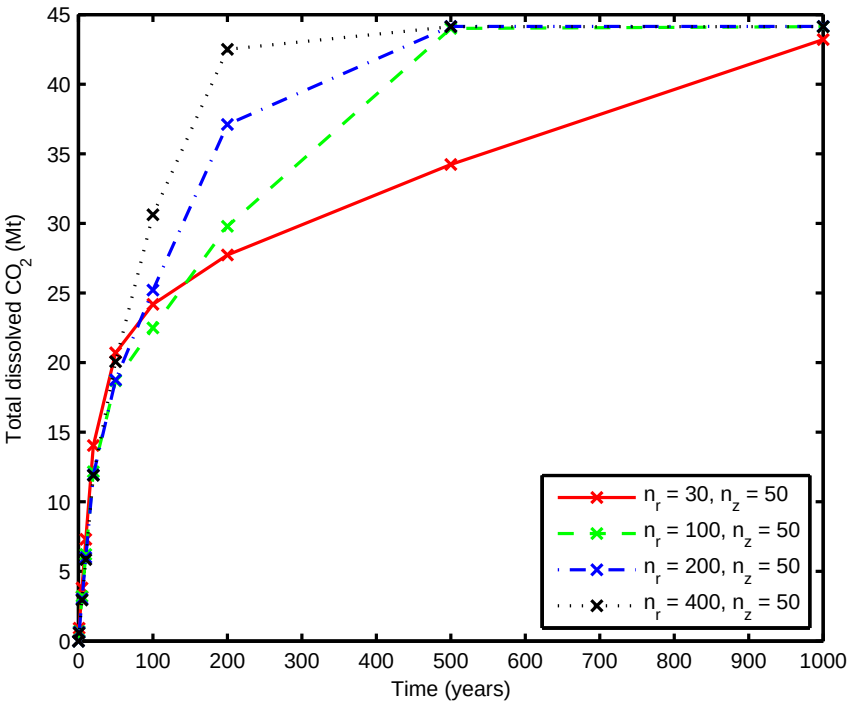

Figure 7.13: Total amount of dissolved CO_2 for models with varying vertical resolution

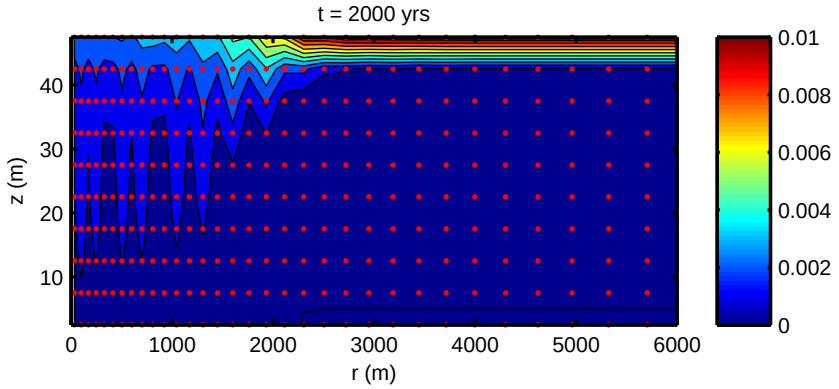

Figure 7.14: Mass fraction of dissolved CO_2, X_{12}, caused by convection from a CO_2 saturated aqueous layer. Red dots indicate location of grid cell centres. $n_r = 40$, $n_z = 10$

Effect of logarithmically spaced grid cells on convection

To further investigate the effect of grid resolution on convection patterns some models were run without CO_2 injection but with the condition along the top boundary of a layer of brine saturated with CO_2. The models were run with no injection but CO_2 was allowed to diffuse into the brine from the boundary.

Fig. 7.14 shows the dissolved mass fraction of CO_2 in the model after 2000 years. Red dots indicate the grid cell centres. Within the model grid resolution gets coarser as you move from left to right. Convective downwelling has begun at the left hand side of the model where grid resolution is finest but is not present in the coarser resolution part of the model. The peaks and troughs of the convection are coincident with the grid points.

7.4 Discussion

Results from benchmarking tests for pressure buildup and CO_2 migration show that the model is in fairly good agreement with the analytical results. This shows that the MATLAB model is able to represent the simplified model proposed in Mathias *et al.* (2011) and increases confidence in results produced by it for more complicated scenarios. Discrepancies between the two models of CO_2 migration close to the well and at the leading front (Figs. 7.4 and 7.5) are due to numerical diffusion which smears out the sharp fronts in the numerical model. Discrepancies in vertically averaged pressure between the two models close to the well (Figs. 7.2 and 7.3) are due to the fact that the analytical solution assumes constant fluid properties throughout the simulation whereas the fluid properties in the numerical model are allowed to change with pressure.

Section 2.3 shows that the size of the error in the finite difference approximation is controlled by the order of the approximation used and the spacing between points in the solution. Resolution testing was performed in order to find the resolution at which errors in the solution, relating to the spatial discretisation of the governing equations, are small enough such that increasing the grid resolution further doesn't make an appreciable difference to the solution.

Varying vertical resolution was shown to have a small impact on overall measures of CO_2 dissolution such as dissolution rates and total amounts of dissolved CO_2. However, small scale characteristics of fingering were noticeably different depending on the vertical resolution (Figs. 7.6 and 7.7). This suggests that vertical resolution needs to be increased further in order to be able to model the spatial patterns of convection robustly.

The model proved to be unstable as no simulations with $n_z > 50$ were able to run for the full 1000 years. It is likely that noise present in the solution increased to such an extent that the simulation became unstable and crashed. The conclusions which can be drawn from the vertical resolution testing are therefore severely limited as we can only really compare two data points, $n_z = 30$ and $n_z = 50$. Out of the simulations that failed to converge most stopped running within 40 years of the end of injection so were not useful for comparing long term results.

The results in Section 7.3.2 show that CO_2 dissolution rate and the total amount of dissolved CO_2 are dependent on horizontal grid resolution. More convective fingers have been resolved in the higher resolution model (Fig. 7.11) which has increased the rate of CO_2 dissolution in the higher resolution model at later times. These results indicate that we need to increase the horizontal grid resolution further in order to have confidence that any results produced are not just artefacts of the grid resolution. The fact that convection patterns in the model are controlled by grid resolution is clearly seen in Fig. 7.14 where convection only occurs at the left hand side of the model where grid resolution is highest. The wavelength of the convective fingers is very similar to the grid spacing. If patterns of convection were independent of grid spacing we would expect to see the width of convective fingers spanning several grid points. Also the fingers would have a more rounded appearance.

Riaz *et al.* (2006) give the critical wavelength, λ_c, for convection in a semi-infinite porous domain as:

$$\lambda_c = \frac{2\pi\mu D_A}{0.07k\Delta\rho g} \tag{7.1}$$

where D_A is apparent diffusivity and is equal to D_E/ϕ, and $\Delta\rho$ is the difference in density

between brine fully saturated with CO_2 and brine containing no CO_2.

The critical wavelength is the wavelength at which convective instabilities will start to grow. Riaz *et al.* (2006) recommend that numerical simulations should be able to resolve wavelengths as small as this in order to model the convection process well.

Based on the values shown in Table 7.1 we get $\Delta\rho = 5.545$ kg m^{-3}. This gives a critical wavelength of $\lambda_c = 0.29$ m for $k = 10^{-12}$ m^2 and $\lambda_c = 2.90$ m for $k = 10^{-13}$ m^2. These wavelengths are smaller than the smallest grid resolutions modelled (Table 7.2), suggesting we need to increase our model resolution if we want to properly resolve the convective fingers.

Results of the resolution testing indicate that higher resolution modelling is required. However, it has also been shown that the model is unstable at higher resolutions. To reduce instability in the model a different numerical scheme with a smaller error is needed.

There are several ways in which the accuracy of the model could be improved. The most obvious way would be to use a higher order finite difference scheme. However, higher order schemes require the use of more surrounding grid points when estimating the solution at a specific point. This makes the problem much more computationally intensive.

Higher order compact finite difference schemes (Lele, 1992; Spotz & Carey, 1995) can achieve higher order accuracy whilst utilising fewer surrounding grid points than the equivalent order finite difference scheme. They work by approximating the error terms in the finite difference formulation (Eqs. (2.17) and (2.20)) using finite differences and adding these onto the original approximation. Riaz *et al.* (2006) and Hidalgo *et al.* (2013) have both used 6th order compact finite difference formulations in their numerical simulations of CO_2 dissolution and convection.

Another option for producing more accurate solutions is to use pseudospectral collocation methods (e.g Trefethen, 2000; Boyd, 2001). When using pseudospectral collocation methods the function to be differentiated is approximated using a combination of trigonometric polynomials (e.g. a Fourier series, Chebyshev polynomials). The derivative of the trigonometric polynomials is then taken as an approximation to the derivative of the original function. The disadvantage of using pseudospectral methods is that the solution at each point depends on the solution at all other points in the domain, making the problem more computationally intensive. However, the advantage of pseudospectral methods is that the error decreases exponentially with the number of grid points used. This means that far fewer grid points are needed for higher order accurate approximations.

Pseudospectral methods have been used by several authors to model flow and transport in porous media. Riaz *et al.* (2006) and Van Reeuwijk *et al.* (2009) used pseudospectral methods to simulate single phase, buoyancy driven flow in porous media. Bjørnarå & Mathias (2013) used pseudospectral methods to model two phase flow in a porous medium with capillary pressure effects.

Pseudospectral methods work well if the solution is smooth enough, however they are prone to oscillations in the presence of non-smooth solutions. The problem we are trying to solve may not be smooth enough to prevent oscillations occurring if pseudospectral methods are used. To reduce oscillations a hybrid numerical scheme, where the smooth parts of the solution are solved pseudospectrally whilst the non-smooth parts of the solution are solved using finite differences, may be appropriate. Costa & Don (2007) suggest the use of pseudospectral methods coupled with weighted essentially non-oscillatory (WENO) finite difference methods (Shu, 2009) for solving hyperbolic equations. In their method the solution is split into subdomains and the smoothness of each subdomain is assessed. If the solution in a particular subdomain is smooth enough pseudospectral methods will be used in that subdomain, otherwise the WENO finite difference method will be used. The WENO finite difference method is a higher order finite difference scheme. It works by assessing the smoothness of the solution within the finite difference stencil (the points being used for the approximation), and if it is not smooth enough uses a smaller stencil (lower order finite difference approximation) which does not include the non-smooth portions of the solution.

Further work and testing is required to find the most appropriate numerical scheme to use in the model. This should be a priority for future work so that the model can be made robust enough to convincingly investigate CO_2 dissolution and convection processes, accompanied by two phase flow processes.

7.5 Conclusion

There is currently a need to the investigate process of CO_2 dissolution and convection from a moving plume of CO_2, including partial miscibility and capillary pressure effects. A two phase, two component, radial flow model has been developed to address this problem. The model has been solved using a second order finite difference scheme in space and the `ode15s` MATLAB ode solver in time.

Comparison of the model with the analytical solution of Mathias *et al.* (2011) produces

favourable results for plume diameter and pressure buildup.

Numerical instabilities within the model did not allow grid resolution to be increased to the point at which the solution became independent of the grid being used. As a priority further work is required to improve the numerical scheme used for the spatial discretisation. Possible methods for increasing model accuracy include using high order compact finite difference schemes, using pseudospectral collocation methods or using some combination of the two.

Chapter 8

Conclusions and Further Work

Summary

This chapter presents the overall conclusions of the thesis and provides suggestions for further work.

8.1 Conclusions

Geological storage of CO_2 in saline aquifers is a complex problem involving many different processes and occurring on many different scales. It would be impossible to build a numerical model which could completely model the whole system and allow a detailed investigation of all aspects of CO_2 storage.

Within this thesis three different models have been implemented to investigate CO_2 storage in saline aquifers. The work undertaken with each model had a slightly different focus, therefore models were designed differently to deal with the varying level of detail required and the overall question they were trying to address. There are differences between the models, in terms of their geometry and the processes included in them.

Chapter 4 provided a case study of the characterisation of a particular storage site within the UK North Sea. The model built in Chapter 4 was designed to model large, field scale processes and produce a rough idea of values for storage capacity, CO_2 migration and pressure buildup, along with the factors which were a major influence on them. The high degree of uncertainty in the input parameters meant that a range of estimates were made using best, most likely and

worst case scenarios. Several properties were varied such as the porosity and permeability, the nature of the reservoir boundaries, the presence of distinct layers within the reservoir and the reservoir geometry. This meant that it was possible to assess which factors had the biggest impact on the model results. Producing a range of results showed that for most parameter ranges CO_2 migration and pressure buildup were within the predefined limits for the site to be suitable as a storage site therefore indicating that it was worth further investigation. Modelling results indicated that the primary factor affecting pressure buildup is the nature of the boundary at the base of the reservoir, permeable or impermeable. The porosity and permeability structure within the reservoir were shown to have the biggest impact on the migration of the CO_2.

Despite the uncertainties in input parameters the model proved very useful for assessing if the site was suitable for CO_2 storage and identifying priorities for data collection. Dynamic modelling was able to refine storage capacity estimates produced using static modelling and provide insight into CO_2 storage for a wider range of model scenarios compared to analytical modelling.

Various aspects of the CO_2 storage process were not modelled, such as the best injection strategy or longer term trapping mechanisms. However, modelling these processes would not have added to our understanding of how suitable the site was for storing CO_2. They are much more influenced by variations in input parameters than the broad scale metrics of CO_2 migration and pressure buildup. Therefore it would have been impossible to have any confidence in the results of modelling these processes in light of the wide range of possible input parameters.

The model built in Chapter 5 was designed to look at the process of dissolution on a much finer scale. The problem being investigated regarded the enhancement to amounts of CO_2 dissolution caused by the flow of CO_2 through a fracture and associated convection dynamics. As the problem was not concerned with the injection process or the two phase flow of gaseous CO_2 within a brine filled aquifer, it was not necessary to incorporate these things into the model. Additionally, as a first step it was not necessary to model the fracture in three dimensions as it was possible to gain an overview of the dynamics of the convection process from the two dimensional model.

Results from this model showed that CO_2 movement through a fracture could facilitate convection currents which increased CO_2 dissolution rates. Despite this increased dissolution the proportion of dissolved CO_2 compared to the proportion of CO_2 flowing through the fracture is likely to be very small although this is highly dependent on fracture aperture.

The model was too simplistic to provide a definitive answer about the relative merits of

injecting CO_2 close to units containing fractures. However, the work was useful overall as it showed that dissolution effects associated with flow through fractures can have a bearing on the long term fate of stored CO_2. Furthermore the work highlighted the fact that the fate of leaked CO_2 is something to be considered when assessing the potential of CO_2 storage site.

In Chapter 7 the model was built in order to model the injection and convection enhanced dissolution processes. This is perhaps more ambitious than the two previous models as it attempts to model the large scale injection process and the small scale convection process. Specifically the model was designed to include both the effects of partial miscibility and large scale dynamics of CO_2 injection on the dissolution and convection processes.

Currently the model is suitable for simulating larger scale processes (suggested by the good agreement with the analytical solution of Mathias *et al.* (2011)) but is not robust enough to model small scale convection. Due to numerical instabilities in the model it was not possible to refine the grid enough to accurately resolve the fine scale convective fingers. Further work is needed towards building a more holistic model of CO_2 injection which integrates processes on a range of scales.

8.2 Future work

As our knowledge of convection enhanced dissolution is increasing the logical next step will be to model the interaction of the small scale dissolution process with the overall injection process. This presents a major challenge for dynamic simulations as the variation in scale between the processes being modelled is large. A compromise needs to be made between the level of grid refinement necessary and the computational effort required.

As suggested in Chapter 7 a possible solution to this would be the use of higher accuracy numerical methods, leading to better modelling of the fine scale dynamics of flow using fewer grid points than lower order accurate methods. Pseudospectral methods, WENO Finite difference and hybrid pseudospectral-WENO methods have been briefly described in Section 7.4 however this is not an exhaustive list. Further work should investigate different numerical methods which have been applied in other fields in the hope that they may be applicable to modelling multiphase flow with diffusion and convection in porous media.

The use of adaptive mesh refinement, such as in the work by Pau *et al.* (2010), may work well for modelling small scale convection processes at the same time as field scale injection processes. Here the grid can be refined in certain areas based on certain criteria. For example

in Pau *et al.* (2010) local grid refinement is temporarily introduced around areas which have a large enough density gradient within the aqueous phase, thereby increasing the grid resolution around the edges of convective fingers of CO_2.

Another solution would be to use a fine scale mesh for the whole model but take advantage of improvements in computing power by running simulations in parallel on multi-core clusters or using graphics processing units (GPUs). TOUGH2-MP currently has the capability to run simulations in parallel but these would still be prohibitively slow if a field scale model was run with very high resolution. However, TOUGH2-MP models lots of processes which aren't necessarily required to investigate the CO_2 injection and dissolution processes. If a model could be built in parallel which only included certain processes this may speed up calculations enough to allow modelling of field scale injection and small scale convection.

All these suggestions would require thorough investigation and testing. It may be that in the end a combination of methods would be the most effective for allowing simultaneous modelling of CO_2 injection and convection enhanced dissolution on a larger range of scales. An increase in the range of scales that could be modelled may also be highly beneficial when carrying out site characterisations such as the one in Chapter 4 as it would allow more aspects of CO_2 storage to be investigated within the same model. For instance a model of the migration of CO_2 and pressure buildup could be accompanied by information on the patterns of convection likely to occur at a given site. However, it is important to bear in mind the uncertainties in the model input data and not to draw detailed conclusions using models which contain major assumptions.

Appendix A

Divergence and gradient

A.1 Divergence

A.1.1 Divergence in Cartesian coordinates

The divergence operator, $\nabla \cdot ()$ appears in Eq. (2.1). If we have a 2D vector, $\boldsymbol{v} = (v_x, v_y)$, the divergence of v in 2D Cartesian coordinates (x, y) is:

$$\nabla \cdot (\boldsymbol{v}) = \frac{\partial v_x}{\partial x} + \frac{\partial v_y}{\partial y} \tag{A.1}$$

This is the formulation used in the model in Chapter 5. In a 3D Cartesian coordinate system (x, y, z), as used in Chapter 4, the divergence of the 3D vector $\boldsymbol{v} = (v_x, v_y, v_z)$ is:

$$\nabla \cdot (\boldsymbol{v}) = \frac{\partial v_x}{\partial x} + \frac{\partial v_y}{\partial y} + \frac{\partial v_z}{\partial z} \tag{A.2}$$

A.1.2 Divergence in cylindrical coordinates

Chapter 7 uses a 2D cylindrical coordinate system (r, z). Divergence of the vector $\boldsymbol{v} = (v_r, v_z)$ is given by:

$$\nabla \cdot (\boldsymbol{v}) = \frac{1}{r}\frac{\partial r v_r}{\partial r} + \frac{\partial v_z}{\partial z} \tag{A.3}$$

A.2 Gradient

A.2.1 Gradient in Cartesian coordinates

Eqs. (2.5) and (2.6) both involve the gradient operator, $\nabla()$. In 2D Cartesian coordinates the gradient of scalar field P is given by:

$$\nabla(P) = \left[\frac{\partial P}{\partial x}, \frac{\partial P}{\partial y}\right] \tag{A.4}$$

In 3D Cartesian coordinates the gradient of P is:

$$\nabla(P) = \left[\frac{\partial P}{\partial x}, \frac{\partial P}{\partial y}, \frac{\partial P}{\partial z}\right] \tag{A.5}$$

A.2.2 Gradient in cylindrical coordinates

In 2D cylindrical coordinates the gradient of P is given by:

$$\nabla(P) = \left[\frac{\partial P}{\partial r}, \frac{\partial P}{\partial z}\right]. \tag{A.6}$$

Appendix B

Finite difference approximation

The finite difference approximations of Eqs. Eq. (5.10) - Eq. (5.12) have been derived as follows (after Mathias *et al.* (2008), Mathias *et al.* (2009a)).

First we discretise in space. The model domain is split into $N \times M$ nodes along the x and z axes respectively, such that:

$$0 < x_{(i,j)} < x_{max} \qquad 0 < z_{(i,j)} < z_{max} \tag{B.1}$$

for $i = 1 \ldots N$ and $j = 1 \ldots M$, where $x_{(i,j)}$ and $z_{(i,j)}$ are the values of x_D and z_D at node (i, j) and x_{max} and z_{max} are the values of x_D and z_D at the boundaries of the domain. We define $P_{(i,j)}$, $C_{(i,j)}$, $q_{x(i,j)}$ and $q_{z(i,j)}$to represent the values of P_D, C_D, q_{xD} and q_{zD} at each node (i, j) respectively.

The following set of ordinary differential equations with respect to time, are developed:

$$\frac{\partial P_{(i,j)}}{\partial t_D} \approx -\frac{1}{\epsilon}\left(\left[\frac{q_{x(i+\frac{1}{2},j)} - q_{x(i-\frac{1}{2},j)}}{x_{(i+\frac{1}{2},j)} - x_{(i-\frac{1}{2},j)}}\right] + \left[\frac{q_{z(i,j+\frac{1}{2})} - q_{z(i,j-\frac{1}{2})}}{z_{(i,j+\frac{1}{2})} - z_{(i,j-\frac{1}{2})}}\right]\right), \quad i = 1...N, \quad j = 1...M \tag{B.2}$$

$$\frac{\partial C_{(i,j)}}{\partial t_D} \approx -\frac{1}{x_{(i+\frac{1}{2},j)} - x_{(i-\frac{1}{2},j)}} \left\{ \left(q_{x(i+\frac{1}{2},j)} RaC_{(i+\frac{1}{2},j)} - \left[\frac{C_{(i+1,j)} - C_{(i,j)}}{x_{(i+1,j)} - x_{(i,j)}} \right] \right) - \left(q_{x(i-\frac{1}{2},j)} RaC_{(i-\frac{1}{2},j)} - \left[\frac{C_{(i,j)} - C_{(i-1,j)}}{x_{(i,j)} - x_{(i-1,j)}} \right] \right) \right\}$$
$$- \frac{1}{z_{(i,j+\frac{1}{2})} - z_{(i,j-\frac{1}{2})}} \left\{ \left(q_{z(i,j+\frac{1}{2})} RaC_{(i,j+\frac{1}{2})} - \left[\frac{C_{(i,j+1)} - C_{(i,j)}}{z_{(i,j+1)} - z_{(i,j)}} \right] \right) - \left(q_{z(i,j-\frac{1}{2})} RaC_{(i,j-\frac{1}{2})} - \left[\frac{C_{(i,j)} - C_{(i,j-1)}}{z_{(i,j)} - z_{(i,j-1)}} \right] \right) \right\}, \quad i = 2...N-1, \quad j = 2...M-1 \tag{B.3}$$

where:

$$q_{x(i+\frac{1}{2},j)} = -\left(\frac{P_{(i+1,j)} - P_{(i,j)}}{x_{(i+1,j)} - x_{(i,j)}} \right)$$
$$q_{x(i-\frac{1}{2},j)} = -\left(\frac{P_{(i,j)} - P_{(i-1,j)}}{x_{(i,j)} - x_{(i-1,j)}} \right), \quad i = 2...N-1, \quad j = 1...M \tag{B.4}$$

$$q_{z(i,j+\frac{1}{2})} = -\left(\frac{P_{(i,j+1)} - P_{(i,j)}}{z_{(i,j+1)} - z_{(i,j)}} \right) - C_{(i,j+\frac{1}{2})}$$
$$q_{z(i,j-\frac{1}{2})} = -\left(\frac{P_{(i,j)} - P_{(i,j-1)}}{z_{(i,j)} - z_{(i,j-1)}} \right) - C_{(i,j-\frac{1}{2})}, \quad i = 1...N, \quad j = 2...M-1 \tag{B.5}$$

The boundary conditions shown in Eqs. Eq. (5.13) and Eq. (5.14) are then given by:

$$q_{x(i-\frac{1}{2},j)} = 0 \quad i = 1, \quad j = 1...M$$
$$q_{x(i+\frac{1}{2},j)} = 0 \quad i = N, \quad j = 1...M$$
$$q_{z(i,j-\frac{1}{2})} = 0 \quad i = 1...N, \quad j = 1$$
$$q_{z(i,j+\frac{1}{2})} = 0 \quad i = 1...N, \quad j = M \tag{B.6}$$

$$
\begin{aligned}
C_{(i-\frac{1}{2},j)} &= 1 \quad i = 1, \quad j = 1...M \\
\left[\frac{C_{(i+1,j)} - C_{(i,j)}}{x_{(i+1,j)} - x_{(i,j)}}\right] &= 0 \quad i = N, \quad j = 1...M \\
\left[\frac{C_{(i,j-1)} - C_{(i,j)}}{z_{(i,j-1)} - z_{(i,j)}}\right] &= 0 \quad i = 1...N, \quad j = 1 \\
\left[\frac{C_{(i,j+1)} - C_{(i,j)}}{z_{(i,j+1)} - z_{(i,j)}}\right] &= 0 \quad i = 1...N, \quad j = M
\end{aligned}
\tag{B.7}
$$

References

Adams, J. & Bachu, S. (2002). Equations of state for basin geofluids: algorithm review and intercomparison for brines. *Geofluids*, **2**(4):257–271.

Altunin, V. V. (1975). Thermophysical Properties of Carbon Dioxide. Moscow: Publishing House of Standards.

Annunziatellis, A., Beaubien, S. E., Bigi, S., Ciotoli, G., Coltella, M. & Lombardi, S. (2008). Gas migration along fault systems and through the vadose zone in the Latera caldera (central Italy): Implications for CO_2 geological storage. *International Journal of Greenhouse Gas Control*, **2**(3):353–372.

Armitage, P. J., Faulkner, D. R. & Worden, R. H. (2013). Caprock corrosion. *Nature Geoscience*, **6**(2):79–80.

Arts, R., Eiken, O., Chadwick, A., Zweigel, P., van der Meer, L. & Zinszner, B. (2004). Monitoring of CO_2 injected at Sleipner using time-lapse seismic data. *Energy*, **29**(9–10):1383–1392.

Audigane, P., Gaus, I., Czernichowski-Lauriol, I., Pruess, K. & Xu, T. (2007). Two-dimensional reactive transport modeling of CO_2 injection in a saline aquifer at the Sleipner site, North Sea. *American Journal of Science*, **307**(7):974–1008.

Batzle, M. & Wang, Z. (1992). Seismic properties of pore fluids. *Geophysics*, **57**(11):1396–1408.

Bear, J. (1989). Dynamics of fluids in porous media. Dover Publications Inc.

Bennion, D. B., Bachu, S. *et al.* (2006). Supercritical CO_2 and h_2s - brine drainage and imbibition relative permeability relationships for intercrystalline sandstone and carbonate formations. In *SPE Europec/EAGE Annual Conference and Exhibition*.

Bentham, M. (2006). An assessment of carbon sequestration potential in the UK-Southern North Sea case study. *Tyndall Centre for Climate Change Research and British Geological Survey. Keyworth, Nottingham, UK: Kingsley Dunham Centre*.

Bjørnarå, T. I. & Mathias, S. A. (2013). A pseudospectral approach to the McWhorter and Sunada equation for two-phase flow in porous media with capillary pressure. *Computational Geosciences*, **17**(6):889–897.

Boait, F. C., White, N. J., Bickle, M. J., Chadwick, R. A., Neufeld, J. A. & Huppert, H. E. (2012). Spatial and temporal evolution of injected CO_2 at the Sleipner Field, North Sea. *Journal of Geophysical Research: Solid Earth (1978–2012)*, **117**(B3).

Boreham, C., Underschultz, J., Stalker, L., Kirste, D., Freifeld, B., Jenkins, C. & Ennis-King, J. (2011). Monitoring of CO_2 storage in a depleted natural gas reservoir: gas geochemistry from the CO_2CRC Otway Project, Australia. *International Journal of Greenhouse Gas Control*, **5**(4):1039–1054.

Boyd, J. P. (2001). Chebyshev and Fourier spectral methods. Courier Corporation.

Caine, J. S., Evans, J. P. & Forster, C. B. (1996). Fault zone architecture and permeability structure. *Geology*, **24**(11):1025–1028.

Carneiro, J. F. (2009). Numerical simulations on the influence of matrix diffusion to carbon sequestration in double porosity fissured aquifers. *International Journal of Greenhouse Gas Control*, **3**(4):431–443.

Carslaw, H. S. & Jaeger, J. C. (1959). Conduction of heat in solids. Clarendon Press.

Chadwick, R., Arts, R. & Eiken, O. (2005). 4D seismic quantification of a growing CO_2 plume at Sleipner, North Sea. *Geological Society, London, Petroleum Geology Conference series*, **6**:1385–1399.

Chadwick, R. A., Noy, D., Arts, R. & Eiken, O. (2009a). Latest time-lapse seismic data from sleipner yield new insights into CO_2 plume development. *Energy Procedia*, **1**(1):2103–2110.

Chadwick, R. A., Noy, D. J. & Holloway, S. (2009b). Flow processes and pressure evolution in aquifers during the injection of supercritical CO_2 as a greenhouse gas mitigation measure. *Petroleum Geoscience*, **15**(1):59–73.

Chalbaud, C., Robin, M., Lombard, J., Martin, F., Egermann, P. & Bertin, H. (2009). Interfacial tension measurements and wettability evaluation for geological CO_2 storage. *Advances in Water Resources*, **32**(1):98–109.

Chang, K. W., Minkoff, S. E. & Bryant, S. L. (2009). Simplified model for CO_2 leakage and its attenuation due to geological structures. *Energy Procedia*, **1**(1):3453–3460.

Chasset, C., Jarsjö, J., Erlström, M., Cvetkovic, V. & Destouni, G. (2011). Scenario simulations of CO_2 injection feasibility, plume migration and storage in a saline aquifer, Scania, Sweden. *International Journal of Greenhouse Gas Control*, **5**(5):1303–1318.

Cornford, C. (1998). Source rocks and hydrocarbons of the north sea. In *Petroleum Geology of the North Sea* (Glennie, K. W. (Ed.)), p. 376–462.

Costa, B. & Don, W. S. (2007). Multi-domain hybrid spectral-weno methods for hyperbolic conservation laws. *Journal of Computational Physics*, **224**(2):970–991.

DECC (2012). CCS Roadmap. Department of Energy and Climate Change.

Denbigh, K. (1957). The principles of chemical equilibrium: with applications in chemistry and chemical engineering. Cambridge University Press.

Doughty, C. (2007). Modeling geologic storage of carbon dioxide: Comparison of non-hysteretic and hysteretic characteristic curves. *Energy Conversion and Management*, **48**(6):1768–1781.

Doughty, C. (2010). Investigation of CO_2 plume behavior for a large-scale pilot test of geologic carbon storage in a saline formation. *Transport in Porous Media*, **82**(1):49–76.

Duan, Z. & Sun, R. (2003). An improved model calculating CO_2 solubility in pure water and aqueous NaCl solutions from 273 to 533 K and from 0 to 2000 bar. *Chemical Geology*, **193**(3):257–271.

Eigestad, G. T., Dahle, H. K., Hellevang, B., Riis, F., Johansen, W. T. & Øian, E. (2009). Geological modeling and simulation of CO_2 injection in the Johansen formation. *Computational Geosciences*, **13**(4):435–450.

Elenius, M. T., Nordbotten, J. M. & Kalisch, H. (2012). Effects of a capillary transition zone on the stability of a diffusive boundary layer. *IMA Journal of Applied Mathematics*.

Elenius, M. T., Nordbotten, J. M. & Kalisch, H. (2014). Convective mixing influenced by the capillary transition zone. *Computational Geosciences*, **18**(3-4):417–431.

Emami-Meybodi, H. & Hassanzadeh, H. (2015). Two-phase convective mixing under a buoyant plume of CO_2 in deep saline aquifers. *Advances in Water Resources*, **76**:55–71.

Ennis-King, J., Preston, I. & Paterson, L. (2005). Onset of convection in anisotropic porous media subject to a rapid change in boundary conditions. *Physics of Fluids*, **17**(8):084107.

European Union (2009). Directive 2009/31/EC of the European Parliament and of the Council. *Official Journal of the European Union, L 140*, **52**(2009/31/EC):114–135.

Farajzadeh, R., Ranganathan, P., Zitha, P. L. J. & Bruining, J. (2011). The effect of heterogeneity on the character of density-driven natural convection of CO_2 overlying a brine layer. *Advances in Water Resources*, **34**(3):327–339.

Farajzadeh, R., Salimi, H., Zitha, P. L. J. & Bruining, H. (2007). Numerical simulation of density-driven natural convection in porous media with application for CO_2 injection projects. *International Journal of Heat and Mass Transfer*, **50**(25–26):5054–5064.

Fenghour, A., Wakeham, W. A. & Vesovic, V. (1998). The viscosity of carbon dioxide. *Journal of Physical and Chemical Reference Data*, **27**(1):31–44.

Garcia, J. E. (2001). Density of aqueous solutions of CO_2. *Lawrence Berkeley National Laboratory*.

Gasda, S. E., Nordbotten, J. M. & Celia, M. A. (2009). Vertical equilibrium with sub-scale analytical methods for geological CO_2 sequestration. *Computational Geosciences*, **13**(4):469–481.

Gasda, S. E., Nordbotten, J. M. & Celia, M. A. (2011). Vertically averaged approaches for CO_2 migration with solubility trapping. *Water Resources Research*, **47**(5).

Ghanbari, S., Al-Zaabi, Y., Pickup, G., Mackay, E., Gozalpour, F. & Todd, A. (2006). Simulation of CO_2 storage in saline aquifers. *Chemical Engineering Research and Design*, **84**(9):764–775.

Ghomian, Y., Pope, G. A. & Sepehrnoori, K. (2008). Reservoir simulation of CO_2 sequestration pilot in Frio brine formation, USA Gulf Coast. *Energy*, **33**(7):1055–1067.

Gilfillan, S. M. V., Lollar, B. S., Holland, G., Blagburn, D., Stevens, S., Schoell, M., Cassidy, M., Ding, Z., Zhou, Z., Lacrampe-Couloume, G. & Ballentine, C. J. (2009). Solubility trapping in formation water as dominant CO_2 sink in natural gas fields. *Nature*, **458**(7238):614–618.

Glennie, K. W. (1983). Early Permian (Rotliegendes) palaeowinds of the North Sea. *Sedimentary Geology*, **34**(2):245–265.

Glennie, K. W. (Ed.) (1998). Petroleum Geology of the North Sea. Blackwell Science Ltd.

Glennie, K. W., Higham, J. & Stemmerik, L. (2003). Permian. *The Millennium Atlas: Petroleum Geology of the Central and Northern North Sea. The Geological Society, London*, p. 91–103.

Haas Jr, J. (1976). Thermodynamics properties of the coexisting phases and thermochemical properties of the NaCl component in boiling NaCl solutions. *US, Geol. Surv., Bull.;(United States)*, **1421**.

Han, W. S., Lee, S., Lu, C. & McPherson, B. J. (2010). Effects of permeability on CO_2 trapping mechanisms and buoyancy-driven CO_2 migration in saline formations. *Water Resources Research*, **46**(7).

Hartmann, D. L., Klein Tank, A. M. G., Rusticucci, M., Alexander, L. V., Brönnimann, S., Charabi, Y., Dentener, F. J., Dlugokencky, E. J., Easterling, D. R., Kaplan, A., Soden, B. J., Thorne, P. W., Wild, M. & Zhai, P. M. (2013). Observations: Atmosphere and Surface. In *Climate Change 2013: The Physical Science Basis. Contribution of Working Group I to the Fifth Assessment Report of the Intergovernmental Panel on Climate Change* (Stocker, T. F., Qin, D., Plattner, G., Tignor, M., Allen, S. K., Boschung, J., Nauels, A., Xia, Y., Bex, V. & Midgley, P. M. (Eds.)).

Hassanzadeh, H., Pooladi-Darvish, M. & Keith, D. W. (2007). Scaling behavior of convective mixing, with application to geological storage of CO_2. *AIChE Journal*, **53**(5):1121–1131.

Hatzignatiou, D. G., Riis, F., Berenblyum, R., Hladik, V., Lojka, R. & Francu, J. (2011). Screening and evaluation of a saline aquifer for CO_2 storage: Central Bohemian Basin, Czech Republic. *International Journal of Greenhouse Gas Control*, **5**(6):1429–1442.

Hedley, B. J., Davies, R. J., Mathias, S. A., Hanstock, D. & Gluyas, J. G. (2013). Uncertainty in static CO_2 storage capacity estimates: Case study from the North Sea, UK. *Greenhouse Gases: Science and Technology*, **3**(3):212–230.

Heinemann, N., Wilkinson, M., Pickup, G. E., Haszeldine, R. S. & Cutler, N. A. (2012). CO_2 storage in the offshore UK Bunter Sandstone Formation. *International Journal of Greenhouse Gas Control*, **6**:210–219.

Heward, A. P. (1992). Inside Auk - the anatomy of an eolian oil reservoir. *Special Publications of SEPM*.

Heward, A. P., Schofield, P. & Gluyas, J. G. (2003). The Rotliegend reservoir in Block 30/24, UK Central North Sea: including the Argyll (renamed Ardmore) and Innes fields. *Petroleum Geoscience*, **9**(4):295–307.

Hidalgo, J. J., MacMinn, C. W. & Juanes, R. (2013). Dynamics of convective dissolution from a migrating current of carbon dioxide. *Advances in Water Resources*, **62**:511–519.

Hoegh-Guldberg, O. & Bruno, J. F. (2010). The impact of climate change on the worlds marine ecosystems. *Science*, **328**(5985):1523–1528.

Horton, C. W. & Rogers, F. (1945). Convection currents in a porous medium. *Journal of Applied Physics*, **16**(6):367–370.

Hovorka, S. D., Doughty, C., Benson, S. M., Pruess, K. & Knox, P. R. (2004). The impact of geological heterogeneity on CO_2 storage in brine formations: a case study from the Texas Gulf Coast. *Geological Society, London, Special Publications*, **233**(1):147–163.

Hudec, M. R. & Jackson, M. P. A. (2007). Terra infirma: Understanding salt tectonics. *Earth-Science Reviews*, **82**(1–2):1–28.

Iding, M. & Blunt, M. J. (2011). Enhanced solubility trapping of CO_2 in fractured reservoirs. *Energy Procedia*, **4**:4961–4968.

Iding, M. & Ringrose, P. (2010). Evaluating the impact of fractures on the performance of the In Salah CO_2 storage site. *International Journal of Greenhouse Gas Control*, **4**(2):242–248.

Ivandic, M., Juhlin, C., Lueth, S., Bergmann, P., Kashubin, A., Sopher, D., Ivanova, A., Baumann, G. & Henninges, J. (2015). Geophysical monitoring at the Ketzin pilot site for CO_2 storage: New insights into the plume evolution. *International Journal of Greenhouse Gas Control*, **32**:90–105.

Jahangiri, H. R. & Zhang, D. (2011). Effect of spatial heterogeneity on plume distribution and dilution during CO_2 sequestration. *International Journal of Greenhouse Gas Control*, **5**(2):281–293.

Jalalh, A. A. (2006). Compressibility of porous rocks: Part II. new relationships. *Acta Geophysica*, **54**(4):399–412.

Jin, M., Pickup, G., Mackay, E., Todd, A., Monaghan, A. & Naylor, M. (2012). Static and dynamic estimates of CO_2 storage capacity in two saline formations in the UK. *SPE Journal*, **17**(4):1108–1118.

Kestin, J., Khalifa, H. E. & Correia, R. J. (1981). Tables of the dynamic and kinematic viscosity of aqueous NaCl solutions in the temperature range 20-150 °C and the pressure range 0.1-35 MPa. *Journal of Physical and Chemical Reference Data*, **10**(1):71–88.

Kneafsey, T. J. & Pruess, K. (2010). Laboratory flow experiments for visualizing carbon dioxide-induced, density-driven brine convection. *Transport in Porous Media*, **82**(1):123–139.

Lele, S. K. (1992). Compact finite difference schemes with spectral-like resolution. *Journal of Computational Physics*, **103**(1):16–42.

LeVeque, R. J. (2007). Finite difference methods for ordinary and partial differential equations: steady-state and time-dependent problems, vol. 98. SIAM.

MacMinn, C. W. & Juanes, R. (2013). Buoyant currents arrested by convective dissolution. *Geophysical Research Letters*, **40**(10):2017–2022.

MacMinn, C. W., Neufeld, J. A., Hesse, M. A. & Huppert, H. E. (2012). Spreading and convective dissolution of carbon dioxide in vertically confined, horizontal aquifers. *Water Resources Research*, **48**(11).

MacMinn, C. W., Szulczewski, M. L. & Juanes, R. (2011). CO_2 migration in saline aquifers. Part 2. Capillary and solubility trapping. *Journal of Fluid Mechanics*, **688**:321–351.

Mathias, S., Butler, A. & Zhan, H. (2008). Approximate solutions for Forchheimer flow to a well. *Journal of Hydraulic Engineering*, **134**(9):1318–1325.

Mathias, S. A., Gluyas, J. G., González Martínez de Miguel, G. J. & Hosseini, S. A. (2011). Role of partial miscibility on pressure buildup due to constant rate injection of CO_2 into closed and open brine aquifers. *Water Resources Research*, **47**(12).

Mathias, S. A., Gluyas, J. G., Oldenburg, C. M. & Tsang, C. (2010). Analytical solution for Joule–Thomson cooling during CO_2 geo-sequestration in depleted oil and gas reservoirs. *International Journal of Greenhouse Gas Control*, **4**(5):806–810.

Mathias, S. A., Hardisty, P. E., Trudell, M. R. & Zimmerman, R. W. (2009a). Approximate solutions for pressure buildup during CO_2 injection in brine aquifers. *Transport in Porous Media*, **79**(2):265–284.

Mathias, S. A., Hardisty, P. E., Trudell, M. R. & Zimmerman, R. W. (2009b). Screening and selection of sites for CO_2 sequestration based on pressure buildup. *International Journal of Greenhouse Gas Control*, **3**(5):577–585.

Mendelsohn, R., Dinar, A. & Williams, L. (2006). The distributional impact of climate change on rich and poor countries. *Environment and Development Economics*, **11**(02):159–178.

Metz, B., Davidson, O., De Coninck, H., Loos, M. & Meyer, L. (Eds.) (2005). IPCC Special Report on Carbon Dioxide Capture and Storage. Prepared by Working Group III of the Intergovernmental Panel on Climate Change. Cambridge University Press.

Mito, S., Xue, Z. & Ohsumi, T. (2008). Case study of geochemical reactions at the Nagaoka CO_2 injection site, Japan. *International Journal of Greenhouse Gas Control*, **2**(3):309–318.

Mojtaba, S., Behzad, R., Rasoul, N. M. & Mohammad, R. (2014). Experimental study of density-driven convection effects on CO_2 dissolution rate in formation water for geological storage. *Journal of Natural Gas Science and Engineering*, **21**:600–607.

Møll Nilsen, H., Herrera, P. A., Ashraf, M., Ligaarden, I., Iding, M., Hermanrud, C., Lie, K., Nordbotten, J. M., Dahle, H. K. & Keilegavlen, E. (2011). Field-case simulation of CO_2-plume migration using vertical-equilibrium models. *Energy Procedia*, **4**:3801–3808.

Myhre, G., Shindell, D., Bréon, F., Collins, W., Fuglestvedt, J., Huang, J., Koch, D., Lamarque, J., Lee, D., Mendoza, A., Nakajima, T., Robock, A., Stephens, G., Takemura, T. & Zhang, H. (2013). Anthropogenic and natural radiative forcing. In *Climate Change 2013: The Physical Science Basis. Contribution of Working Group I to the Fifth Assessment Report of the Intergovernmental Panel on Climate Change* (Stocker, T. F., Qin, D., Plattner, G., Tignor, M., Allen, S. K., Boschung, J., Nauels, A., Xia, Y., Bex, V. & Midgley, P. M. (Eds.)).

Nakajima, T. & Xue, Z. (2013). Evaluation of a resistivity model derived from time-lapse well logging of a pilot-scale CO_2 injection site, Nagaoka, Japan. *International Journal of Greenhouse Gas Control*, **12**:288–299.

Narasimhan, T. N. & Witherspoon, P. A. (1976). An integrated finite difference method for analyzing fluid flow in porous media. *Water Resources Research*, **12**(1):57–64.

Neufeld, J. A., Hesse, M. A., Riaz, A., Hallworth, M. A., Tchelepi, H. A. & Huppert, H. E. (2010). Convective dissolution of carbon dioxide in saline aquifers. *Geophysical Research Letters*, **37**(22).

Nordbotten, J. M., Celia, M. A. & Bachu, S. (2005). Injection and storage of CO_2 in deep saline aquifers: Analytical solution for CO_2 plume evolution during injection. *Transport in Porous media*, **58**(3):339–360.

Noy, D. J., Holloway, S., Chadwick, R. A., Williams, J. D. O., Hannis, S. A. & Lahann, R. W. (2012). Modelling large-scale carbon dioxide injection into the Bunter Sandstone in the UK Southern North Sea. *International Journal of Greenhouse Gas Control*, **9**:220–233.

Obi, E. I. & Blunt, M. J. (2006). Streamline-based simulation of carbon dioxide storage in a North Sea aquifer. *Water Resources Research*, **42**(3).

Oldenburg, C. M. (2007). Joule-Thomson cooling due to CO_2 injection into natural gas reservoirs. *Energy Conversion and Management*, **48**(6):1808–1815.

Pacala, S. & Socolow, R. (2004). Stabilization wedges: solving the climate problem for the next 50 years with current technologies. *science*, **305**(5686):968–972.

Patz, J. A., Campbell-Lendrum, D., Holloway, T. & Foley, J. A. (2005). Impact of regional climate change on human health. *Nature*, **438**(7066):310–317.

Pau, G. S., Bell, J. B., Pruess, K., Almgren, A. S., Lijewski, M. J. & Zhang, K. (2010). High-resolution simulation and characterization of density-driven flow in CO_2 storage in saline aquifers. *Advances in Water Resources*, **33**(4):443–455.

Phillips, S. L. (1981). A technical databook for geothermal energy utilization. *Lawrence Berkeley National Laboratory*.

Pruess, K. (2005). ECO2N: A TOUGH2 fluid property module for mixtures of water, NaCl, and CO_2. *Lawrence Berkeley National Laboratory*.

Pruess, K. (2008). On CO_2 fluid flow and heat transfer behavior in the subsurface, following leakage from a geologic storage reservoir. *Environmental Geology*, **54**(8):1677–1686.

Pruess, K., García, J., Kovscek, T., Oldenburg, C., Rutqvist, J., Steefel, C. & Xu, T. (2004). Code intercomparison builds confidence in numerical simulation models for geologic disposal of CO_2. *Energy*, **29**(9):1431–1444.

Pruess, K. & Nordbotten, J. (2011). Numerical simulation studies of the long-term evolution of a CO_2 plume in a saline aquifer with a sloping caprock. *Transport in Porous Media*, **90**(1):135–151.

Pruess, K., Oldenburg, C. M. & Moridis, G. J. (1999). TOUGH2 User's Guide Version 2. *Lawrence Berkeley National Laboratory*.

Qi, R., LaForce, T. C. & Blunt, M. J. (2009). Design of carbon dioxide storage in aquifers. *International Journal of Greenhouse Gas Control*, **3**(2):195–205.

Redlich, O. & Kwong, J. (1949). On the thermodynamics of solutions. V. An equation of state. Fugacities of gaseous solutions. *Chemical Reviews*, **44**(1):233–244.

Riaz, A., Hesse, M., Tchelepi, H. A. & Orr, F. M. (2006). Onset of convection in a gravitationally unstable diffusive boundary layer in porous media. *Journal of Fluid Mechanics*, **548**:87–111.

Ringrose, P., Nordahl, K. & Wen, R. (2005). Vertical permeability estimation in heterolithic tidal deltaic sandstones. *Petroleum Geoscience*, **11**(1):29–36.

Sathaye, K. J., Hesse, M. A., Cassidy, M. & Stockli, D. F. (2014). Constraints on the magnitude and rate of CO_2 dissolution at Bravo Dome natural gas field. *Proceedings of the National Academy of Sciences*, **111**(43):15332–15337.

Schäfer, F., Walter, L., Class, H. & Müller, C. (2012). The regional pressure impact of CO_2 storage: a showcase study from the North German Basin. *Environmental Earth Sciences*, **65**(7):2037–2049.

Selley, R. C. (1978). Porosity gradients in North Sea oil-bearing sandstones. *Journal of the Geological Society*, **135**(1):119–132.

Shu, C.-W. (2009). High order weighted essentially nonoscillatory schemes for convection dominated problems. *SIAM review*, **51**(1):82–126.

Sibson, R. H. (1990). Conditions for fault-valve behaviour. *Geological Society, London, Special Publications*, **54**(1):15–28.

Smith, E. B. (2002). Basic chemical thermodynamics. Oxford University Press.

Smith, M. M., Sholokhova, Y., Hao, Y. & Carroll, S. A. (2013). Evaporite caprock integrity: An experimental study of reactive mineralogy and pore-cale heterogeneity during brine-CO_2 exposure. *Environmental Science & Technology*, **47**(1):262–268.

Spotz, W. & Carey, G. (1995). High-order compact finite difference methods. In *Preliminary Proceedings International Conference on Spectral and High Order Methods, Houston, TX*.

Spycher, N. & Pruess, K. (2005). CO_2-H2O mixtures in the geological sequestration of CO_2. II. partitioning in chloride brines at 12 to 100 °C and up to 600 bar. *Geochimica et Cosmochimica Acta*, **69**(13):3309–3320.

Spycher, N., Pruess, K. & Ennis-King, J. (2003). CO_2-H_2O mixtures in the geological sequestration of CO_2. I. Assessment and calculation of mutual solubilities from 12 to 100 °C and up to 600 bar. *Geochimica et cosmochimica acta*, **67**(16):3015–3031.

Statoil (2011). Statoil Annual Report. Statoil.

Taylor, J. C. M. (1998). Upper Permian-Zechstein. In *Petroleum Geology of the North Sea* (Glennie, K. W. (Ed.)), p. 174–211.

Trefethen, L. N. (2000). Spectral methods in MATLAB, vol. 10. SIAM.

Trewin, N. H., Fryberger, S. G. & Kreutz, H. (2003). The Auk Field, Block 30/16, UK North Sea. *Geological Society, London, Memoirs*, **20**(1):483–496.

Turcotte, D. L. & Schubert, G. (2002). Geodynamics, vol. 1. Cambridge University Press.

U.S. Energy Information Administration (2014). International Energy Outlook 2014. U.S. Department of Energy.

Van Genuchten, M. T. (1980). A closed-form equation for predicting the hydraulic conductivity of unsaturated soils. *Soil science society of America journal*, **44**(5):892–898.

Van Reeuwijk, M., Mathias, S. A., Simmons, C. T. & Ward, J. D. (2009). Insights from a pseudospectral approach to the Elder problem. *Water Resources Research*, **45**(4).

Wyllie, M. R. J., Gregory, A. R. & Gardner, G. H. F. (1958). An experimental investigation of factors affecting elastic wave velocities in porous media. *Geophysics*, **23**(3):459–493.

Xu, X., Chen, S. & Zhang, D. (2006). Convective stability analysis of the long-term storage of carbon dioxide in deep saline aquifers. *Advances in Water Resources*, **29**(3):397–407.

Yamamoto, H. & Doughty, C. (2011). Investigation of gridding effects for numerical simulations of CO_2 geologic sequestration. *International Journal of Greenhouse Gas Control*, **5**(4):975–985.

Yamamoto, H., Zhang, K., Karasaki, K., Marui, A., Uehara, H. & Nishikawa, N. (2009). Numerical investigation concerning the impact of CO_2 geologic storage on regional groundwater flow. *International Journal of Greenhouse Gas Control*, **3**(5):586–599.

Yielding, G., Lykakis, N. & Underhill, J. R. (2011). The role of stratigraphic juxtaposition for seal integrity in proven CO_2 fault-bound traps of the Southern North Sea. *Petroleum Geoscience*, **17**(2):193–203.

Zhang, K., Wu, Y. & Pruess, K. (2008). User's guide for TOUGH2-MP-a massively parallel version of the TOUGH2 code. *Report LBNL-315E, Lawrence Berkeley National Laboratory, Berkeley, CA*.

Zhou, Q., Birkholzer, J. T., Mehnert, E., Lin, Y. & Zhang, K. (2010). Modeling basin-and plume-scale processes of CO_2 storage for full-scale deployment. *Ground Water*, **48**(4):494–514.

Zhou, Q., Birkholzer, J. T., Tsang, C. & Rutqvist, J. (2008). A method for quick assessment of CO_2 storage capacity in closed and semi-closed saline formations. *International Journal of Greenhouse Gas Control*, **2**(4):626–639.

Zimmerman, R. W. & Bodvarsson, G. S. (1996). Hydraulic conductivity of rock fractures. *Transport in Porous Media*, **23**(1):1–30.

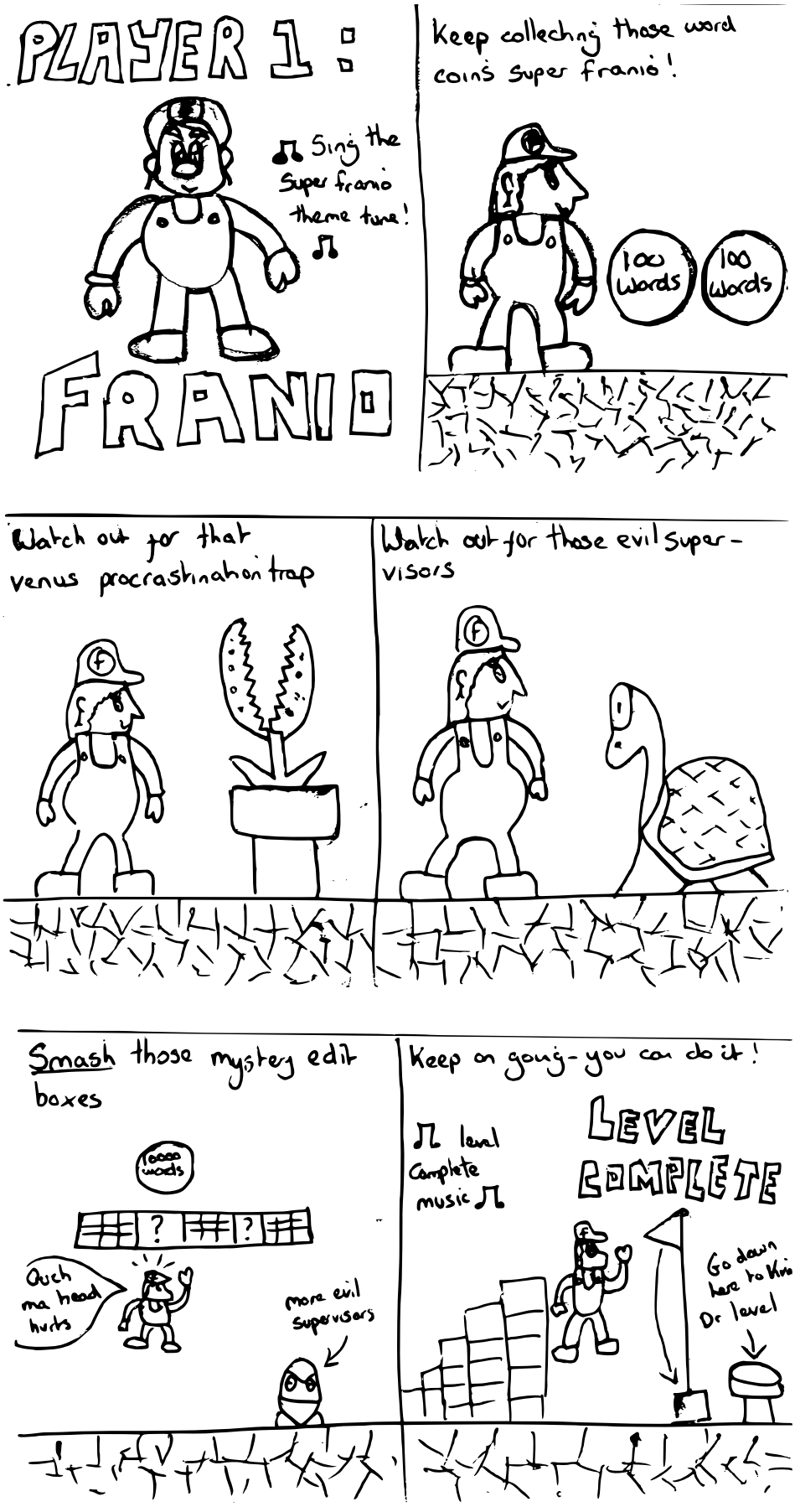

By Dr Sam Clark